MODELING AND SIMULATION OF STRESS-INDUCED NON-UNIFORM OXIDE SCALE GROWTH DURING HIGH-TEMPERATURE OXIDATION OF METALLIC ALLOYS.

A Thesis
Presented to
The Academic Faculty

By

Audric Saillard

In Partial Fulfillment
of the Requirements for the Degree
Doctor of Philosophy of the
Woodruff School of Mechanical Engineering

Georgia Institute of Technology

May 2010

MODELING AND SIMULATION OF
STRESS-INDUCED NON-UNIFORM OXIDE SCALE GROWTH
DURING HIGH-TEMPERATURE OXIDATION OF METALLIC ALLOYS.

Approved by:

Dr. Mohammed Cherkaoui, Advisor
Woodruff School of Mechanical Engineering
Georgia Institute of Technology

Dr. Richard W. Neu
Woodruff School of Mechanical Engineering
Georgia Institute of Technology

Dr. Esteban P. Busso
Centre des Matériaux – UMR CNRS 7633
Mines ParisTech, France

Dr. Preet Singh
School of Material Science and Engineering
Georgia Institute of Technology

Dr. David L. McDowell
Woodruff School of Mechanical Engineering
Georgia Institute of Technology

Date Approved: January 12, 2010

ACKNOWLEDGEMENTS

First, I would like to thank my thesis committee members, Dr. Mohammed Cherkaoui, Dr. Esteban P. Busso, Dr. David L. McDowell, Dr. Richard W. Neu and Dr. Preet Singh for their attention, comments and suggestions. I would like to mention here the collaboration with Dr. Busso, which has allowed to enlarge the scope of application of my PhD work through the interesting study concerning thermal barrier coating systems.

I am deeply grateful to Dr. Laurent Capolungo, who has been my “mentor” during this PhD work. His listening, support and advice have constituted a very precious help and have significantly contributed to the realization of this major academic achievement. I would also like to thank my friend Laurent for the numerous “pauses café”, which despite they made me coffee-addicted, have been much enjoyable moments and the occasion of very interesting work-related and unrelated discussions.

Above all, I am truly grateful to my family and particularly my mother for their precious encouragement and support; and to my friends and colleagues for the numerous wonderful moments we shared that made this period a very memorable time of my life, all their jokes about my never-ending studies, but also their care and attention during the difficult times.

Finally, I would like to thank the persons at GT-Lorraine and GT-Atlanta who assisted me very nicely, from registering at GT to finding my current job! I would like to address my last thanks to the Georgia Institute of Technology and the Région Lorraine, which have provided the environment and the financial support for my PhD thesis.

TABLE OF CONTENTS

LIST OF TABLES

LIST OF FIGURES

SUMMARY

The metallic alloys employed in oxidizing environment at high temperature rely on the development of a protective oxide scale to sustain the long-term aggressive exposition. However, the oxide scale growth is most of the time coupled with stress and morphological developments limiting its lifetime and then jeopardizing the metallic component reliability. In this study, a mechanism of local stress effect on the oxidation kinetics at the metal/oxide interface is investigated. The objective is to improve the understanding on the possible interactions between stress generation and non-uniform oxide scale growth, which might result in a precipitated mechanical failure of the system. Two different oxides are studied, alumina and chromia, in two different industrial systems, thermal barrier coatings and solid oxide fuel cell interconnects. A specific thermodynamic treatment of local oxide phase growth coupled with stress generation is developed. The formulation is completed with a phenomenological macroscopic framework and a numerical simulation tool is developed allowing for realistic analyses. Two practical situations are simulated and analyzed, concerning an SOFC interconnect and a thermal barrier coating system, for which oxide scale growth and associated stress and morphological developments are critical. The consequence of the non-uniform oxide growth on the system resistance to mechanical failure is investigated. Finally, the influences of material-related properties are studied, providing optimization directions for the design of metallic alloys which would improve the mechanical lifetime of the considered systems.

CHAPTER 1

INTRODUCTION

1.1 Motivation and objective

Oxidation resistant metallic alloys are increasingly employed in industrial systems operating at moderately high temperatures (600 to 1200°C), because they have lower fabrication cost and better formability than the traditionally used ceramic compounds. Nevertheless in common cases, the metallic alloy is exposed directly or indirectly to an oxidizing atmosphere (characterized by the presence of oxygen), and an oxide scale inevitably develops at the exposed surface. The principle of oxidation-resistant metallic alloys is that their composition is designed so as to produce a protective oxide scale, typically constituted of alumina or chromia, exhibiting very low permeability to the oxidation reactants, thus limiting as it grows the further extent of the process.

Investigations, mainly experimental, have been conducted for several decades to identify alloy compositions that will optimize oxide scales, to understand the processes of oxide scale development and to understand the contributions of alloy constituents and operating conditions and environments (Padture, Gell et al. 2002; Fergus 2005; Evans, Clarke et al. 2008; Yang 2008). Great progress has been achieved, but many questions remain and the lifetime of metal/oxide systems still needs to be improved. Stress development and resulting phenomena, such as crack nucleation and oxide scale delamination, are among the most critical issues limiting the lifetime of oxide/metal systems operating at high temperatures {Evans, 2008 #216}{Liu, 2009 #367}.

Several processes might contribute to stress generation, and various mechanisms can take place for stress relaxation. The resulting effects have been shown to lead in certain cases to stresses up to several gigapascals, or to large deformations of the oxide scale and the interfacial region of the metallic alloy. Both situations are detrimental to the oxide scale lifetime and usually result in mechanical failure at mid term. For systems of major industrial interest, such as thermal barrier coatings (TBC) for aircraft engines or power generation turbines, or interconnects for solid oxide fuel cells (SOFC), no consensus has been reached on the precise mechanisms limiting the mechanical lifetime and their respective contributions. The role of minor elements in the metallic alloy composition also needs to be elucidated. Indeed, the addition in minor proportions of certain elements has demonstrated dramatic effects on oxide scale development, particularly in terms of growth kinetics, morphology and microstructure, as well as on stress generation. These effects can lead to significant improvement in component lifetime. Due to the local, complex and evolving nature of the materials and processes, further lifetime optimization through extensive experiments is uncertain. Thus there is an increasing need for models and simulation tools that will allow for a better understanding of the key mechanisms and associated materials properties. Further, such models should allow users to predict metal/oxide systems evolution and to optimize the metallic alloy composition through a material-by-design approach.

The primary objective of this work was to develop a model and an associated simulation tool in order to investigate the coupling between oxide scale growth and stress and/or large morphological developments, along with the influence of the metallic alloy properties. The study focuses more particularly on the oxide scale/metallic alloy interface

evolution. The idea developed is that high stresses at the constrained phase boundary might locally modify the oxidation kinetics, inducing a non-uniform growth of the oxide scale. The resulting irregular geometry is very detrimental to the system resistance to failure. Indeed, it might lead to high stress concentration, particularly upon cooling due to the thermal mismatch between the metallic substrate and the oxide layer.

1.2 Document organization

This first chapter provides a comprehensive review of the phenomenon of oxide scale growth and its modeling, with an emphasis on stress development and mechanical failure mechanisms. Over this study, a focus is made on two different oxides, alumina and chromia, which develop in two different considered industrial systems, thermal barrier coatings and solid oxide fuel cell metallic interconnects. The review lead us to investigate a possible mechanism of stress-induced irregular morphological development in growing oxide scales at high temperature. A specific formulation is derived in the second chapter. It describes through a continuum thermodynamics approach a stress-affected local oxide phase propagation by direct oxidation of the metallic substrate at the metal/oxide interface. The local formulation of stress-affected oxidation is then completed with a phenomenological macroscopic framework, and a numerical tool is developed allowing for the analysis of complex cases. These contributions are presented in the third chapter.

Finally, the fourth chapter provides two investigations on practical situations in which oxide scale growth and associated stress and morphological developments are critical to the material system’s lifetime. The first one considers the growth at high

temperature of an oxide scale over a ferritic steel for SOFC interconnect, and the second treats the oxidation of a thermal barrier coating constituted of a nickel-aluminum bond coat covered by an yttria-stabilized zirconia layer. The associated situations present many similarities, but they interestingly differ since in the first one a chromia layer is developed from a flat surface at moderate temperature (~800°C) while in the second an alumina scale forms at a convoluted interface at higher temperature (~1100°C).

1.3 The issue of high temperature oxidation in studied industrial systems

A brief description of the industrial systems studied and the problem caused by high temperature oxidation is here given. Originally the project focused on metallic interconnects for solid oxide fuel cells. It has been enlarged to thermal barrier coatings which face similar problems and on which much more studies have been performed and are available in the literature.

1.3.1 Metallic interconnects in Solid Oxide Fuel Cells

Concerns about the dependence on fossil fuels and emission pollutions have stimulated a growing interest in cleaner and more efficient alternative energy sources. Solid oxide fuel cells (SOFC) are one of these alternatives because of their high conversion efficiency, a combustion free operation releasing optimally no undesired byproducts, and a producible fuel: hydrogen. Even though the technology has reached a reasonable maturity, cost and reliability still constitute major concerns preventing its massive adoption.

In addition to electrolyte, cathode and anode, forming a unit cell, an actual SOFC typically requires another component, namely, the interconnect. Interconnects are conducting layers placed next to each electrode, as shown in Figure 1.1 for a planar SOFC stack (Yang, Weil et al. 2003). Their primary function is to collect the current from the electrodes but structure-wise, they also serve as air and fuel channels. The voltage delivered by a single cell being quite limited (typically less than 1V), a practical power generation device must be constituted of a stack of fuel cells mounted in series. Interconnects are then required to electrically connect two consecutive cells, and also to provide supply conducts of air and fuel for the adjacent electrodes, while forming an impermeable layer for oxygen in order to maintain the oxygen gradient through each cell. Therefore, interconnects must be good electrical conductors with very low ionic conductivity. In addition, the interconnect material must be chemically compatible with all the other cell materials, as well as be stable in both oxidizing and reducing environments at high temperature (~ 1000°C). In addition, interconnect materials must present thermal expansion that matches with those of other cell materials in order to minimize residual stresses, and they must present a high resistance to thermomechanical fatigue for long term reliability. The chemical reaction at the cathode side being largely exothermic (it releases heat), a high thermal conductivity is also desired in order to limit the increase of temperature gradients. High thermal conductivity would also be beneficial in promoting endothermic reforming reactions (dissociation of di-hydrogen from methane for instance) at the anode side.

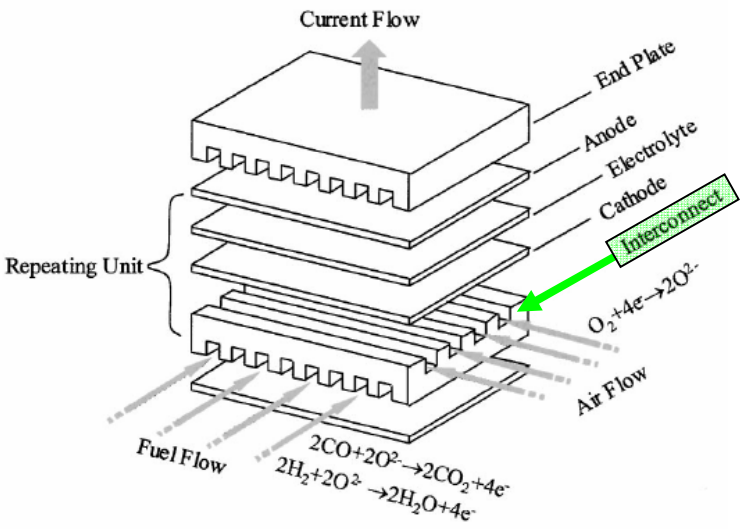

Figure 1.1: Expanded schematic of a planar SOFC stack.

In order to exhibit these stringent properties, complex ceramic compounds have been developed, such as rare earth element-doped chromites (for instance Lanthanum chromite, ($LaCrO_3$)). But these ceramic interconnects are expensive and difficult to fabricate. Recent advances in fuel cell materials and structures (e.g. anode-supported SOFC) have allowed the operational temperature to be lowered to around 800ºC. At such intermediated temperatures, resistant metallic materials can be considered for interconnects. This evolution is very attractive, owing to their lower materials and fabrication costs, easier fabrication and better electrical and thermal conductivity. The major drawback of metallic interconnects is corrosion, unavoidable in the SOFC environment. An oxide layer forms on exposed surfaces and interfaces, resulting with time in the development of a large electrical resistance and the degradation of the mechanical integrity of the component. Figure 1.2 presents cross-sectional scanning electron micrographs (SEM) of oxide scales grown in different conditions representative

of SOFC cathode and anode channel atmospheres (Mikkelsen and Linderoth 2003). In order to meet the goals for SOFC practical lifetime, it is essential to limit and optimize the growth of the oxide scale. Alloys considered for interconnect materials are mostly nickel-based, chromium-based or iron-based. Ferritic steels are the most attractive metallic interconnect materials for SOFC (e.g. Crofer 22 APU by ThyssenKrupp), owing to their limited thermal expansion, high ductility, good workability and low cost (Yang, Weil et al. 2003). Although alumina (Al_2O_3) is a more protective oxide, a chromia (Cr_2O_3) scale is preferred in interconnect applications because it is a good electrical conductor. Therefore a high Cr content (close or above 20%) is introduced in the metallic alloy composition in order to promote the development of this oxide.

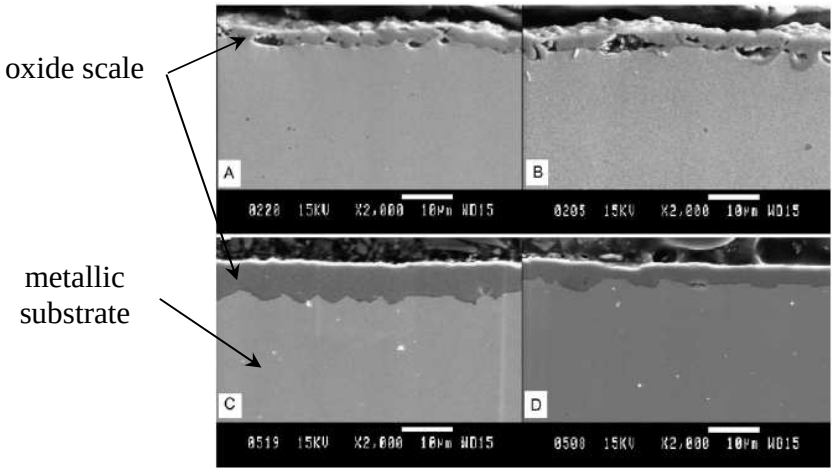

Figure 1.2: Cross-sectional SEMs of oxide scales grown for 70 hours at 900°C on a Fe-22Cr alloy in different SOFC environments (O_2/H_2/H_2O).

1.3.2 Thermal barrier coatings in engines and turbines

Concerns about reducing costs and pollutant emission have also stimulated the development of more efficient and cleaner aircraft engines and industrial gas turbines

used for power generation. The thermodynamic efficiency of these devices strongly relies on the maximum internal temperature. Therefore, a high functioning temperature is desired in order to limit fuel consumption, but it is also beneficial in reducing pollutant emissions (byproducts of combustion whose amount decreases with increasing temperature). However, the sustainability of the structural metallic materials to high temperatures limits the operating range. Therefore, specific high-temperature metallic alloys and coatings have been developed. The last technological evolution is the use of thermal barrier coatings (TBC), on turbine blades, combustor cans, ducting and nozzle guide vanes, which have allowed operating temperatures higher than 1100°C to be reached. A thermal barrier coating must exhibit a very low thermal conductivity, such that a thin layer (a typical thickness is of the order of 100µm) bears a high temperature gradient which results in the metallic substrate being exposed to a significantly reduced temperature. It must also present a high resistance to thermal shock and thermomechanical fatigue, as well as possible mechanical impacts. The most commonly employed TBC material is yttria stabilized zirconia (YSZ), generally deposited by plasma spraying or electron beam physical vapor deposition (EB-PVD) processes. The metallic substrate material (generally a nickel or cobalt superalloy) is usually pre-coated with a soft aluminium-containing bond-coat (NiPtAl or MCrAlY for instance, M designating the substrate metal, Ni or Co). The role of this bond coat is to accommodate residual stresses that might otherwise develop due to the significantly different thermal expansion behaviors of the metallic substrate and the ceramic TBC. A cross-sectional scanning electron micrograph (SEM) of a TBC material system is shown on Figure 1.3, along with

a schematic presenting the environment and the temperature gradient induced by the TBC (Padture, Gell et al. 2002).

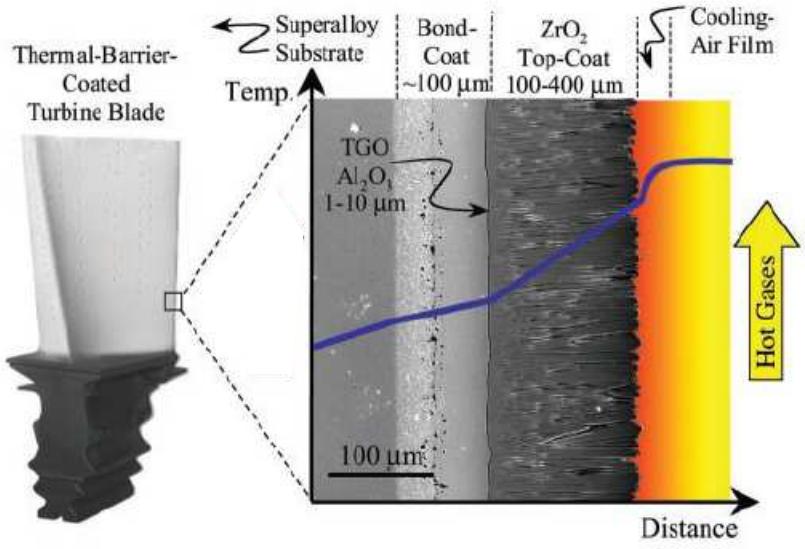

Figure 1.3: Cross-sectional SEM of an EB-PVD TBC system, superimposed onto a schematic diagram showing the temperature gradient induced by the coating.

However, the thermal barrier coating layer is not protective against oxidation, and consequently the bond coat oxidizes under operating conditions. A high aluminium content is introduced at the metallic substrate surface and in the bond coat in order to promote the development of a highly protective alumina layer, usually named thermally grown oxide (TGO) to differentiate it from the initially deposited oxide coating. Nevertheless, the growth of this oxide scale induces large deformations and eventually leads to the delamination and failure of the coating. A cross-section SEM of the TBC/bond coat interface region is presented in Figure 1.4. Again, it is essential to limit and optimize the development of the oxide scale in order to increase the lifetime of thermal barrier coatings.

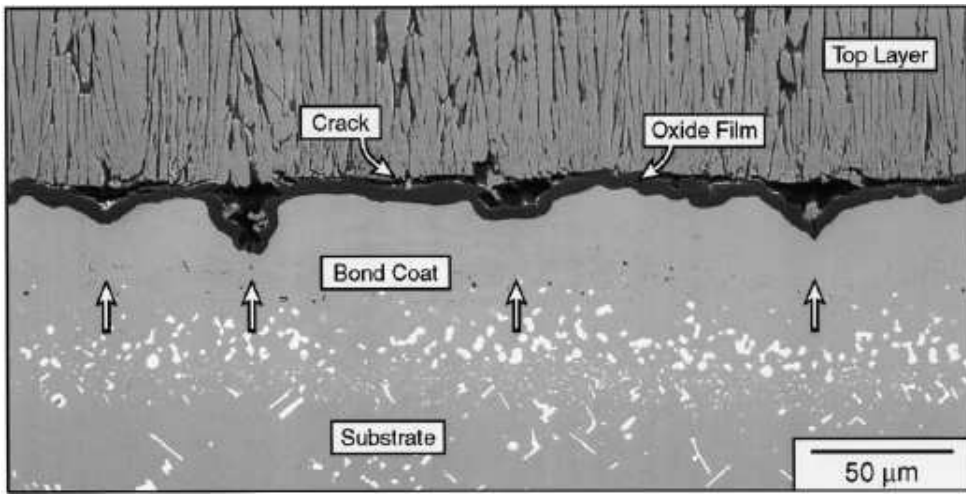

Figure 1.4: Cross-sectional SEM of the bond coat / TBC interface region, showing the developed oxide layer and resulting damages.

1.4 Review on high temperature oxidation

1.4.1 Thermodynamics of oxidation

Oxides are the stable states of metals in earth atmosphere. Therefore metal oxidation is a natural process working towards this stable situation. It globally results from the association of dioxygen molecules present in the atmosphere with metal atoms to form an oxide compound. The general chemical reaction can be described by:

$$nM + O_2 \rightleftharpoons M_nO_2 \tag{1.1}$$

where M represents the metal species, O the oxygen and M_nO_2 the oxide. The forward reaction corresponding to the oxide formation is thermodynamically very favorable, since the corresponding standard free energy, $\Delta G°$, is typically very negative (the oxidation reactions are therefore very exothermal, i.e. they release heat) ($\Delta G°$ is about -550 KJ per

mole of O_2 for chromia at 800°C and around -800 for alumina at 1100°C (Birks, Meier et al. 2006)). Under varying conditions of temperature and oxygen partial pressure, and even more if an alloy including different metallic species is considered, several different oxides might be likely to form. Reaction thermodynamics predicts that the most stable oxide should form, i.e. the one whose free energy of formation is the lowest (highest in magnitude since they are negative). Stability maps for oxides under varying environments are used to predict the main oxide phase that will develop. The molar Gibbs free energy of the oxidation reaction, equation (1.1), is given by:

$$\Delta G_{\mathrm{M}_n\mathrm{O}_2} = \Delta G^{\mathrm{o}}_{\mathrm{M}_n\mathrm{O}_2} + R\theta \ln(P_{\mathrm{O}_2}) \tag{1.2}$$

where $\Delta G^{\mathrm{o}}_{\mathrm{M}_n\mathrm{O}_2}$ is the standard molar free enthalpy of reaction, R is the molar gas constant, θ is the temperature and P_{O_2} is the dioxygen partial pressure to be given in atmospheres (the reference pressure). The oxidation reaction occurs if it releases energy: $\Delta G_{\mathrm{M}_n\mathrm{O}_2} < 0$. From the above equation this gives:

$$\Delta G^{\mathrm{o}}_{\mathrm{M}_n\mathrm{O}_2} < -R\theta \ln(P_{\mathrm{O}_2}) \tag{1.3}$$

The Ellingham diagram provides the standard free enthalpy of oxide formation for a given temperature range. The data is represented by a line obtained from:

$$\Delta G^{\mathrm{o}}_{\mathrm{M}_n\mathrm{O}_2} = \Delta H^{\mathrm{o}}_{\mathrm{M}_n\mathrm{O}_2} + \theta S^{\mathrm{o}}_{\mathrm{M}_n\mathrm{O}_2} \tag{1.4}$$

where $H^{\mathrm{o}}_{\mathrm{M}_n\mathrm{O}_2}$ is the molar free enthalpy and $S^{\mathrm{o}}_{\mathrm{M}_n\mathrm{O}_2}$ is the entropy of reaction, both data being experimentally measured. Then for a given dioxygen partial pressure, the line

$-R\theta\ln(P_{O_2})$ can be drawn on the diagram, and its intersection gives the equilibrium temperature of the oxidation reaction. At lower temperature, $\Delta G^{o}_{M_nO_2} < -R\theta\ln(P_{O_2})$ and the oxide phase is stable. In contrast, at higher temperatures the metal phase is stable. In a reverse way, the diagram allows us to obtain the equilibrium partial dioxygen pressure (commonly called dissociation pressure for the oxide) for a given temperature.

The Ellingham diagrams rely on several assumptions – thermodynamic equilibrium, pure metal phases (activity equal to one), activity of the dioxygen equal to its partial pressure, linear dependency of the standard Gibbs energy with temperature – but they have been proven very useful and are commonly used to predict the oxide phase that will develop under a given environment. For given temperature and oxygen partial pressure, representing a point on the diagram, the oxides that might form are those whose characteristic lines lie below the point, and the most favored one is that presenting the lowest standard Gibbs energy at the considered temperature. The Ellingham diagram for several oxides is presented in Figure 1.5, with a highlight on the data concerning chromia and alumina at the considered temperatures (base diagram reproduced from http://www.doitpoms.ac.uk/tlplib/ellingham_diagrams, University of Cambridge).

Even though the oxidation reaction is thermodynamically favorable, under normal conditions (ambient temperature and atmospheric pressure), the kinetics of the process is extremely slow limiting its extent. Furthermore, some oxides are “protective” for their metal substrate. They form a compact and adherent scale at the exposed surface, which isolates the metal phase from the oxidizing atmosphere, thus blocking the oxidation process. Therefore the composition of a metallic alloy can be designed to render it “resistant” to oxidation. In this case, elements are introduced, typically chromium or

aluminium, to form a protective oxide scale of chromia or alumina, respectively. This is for instance the case of stainless steels which are oxidation-resistant at room temperature.

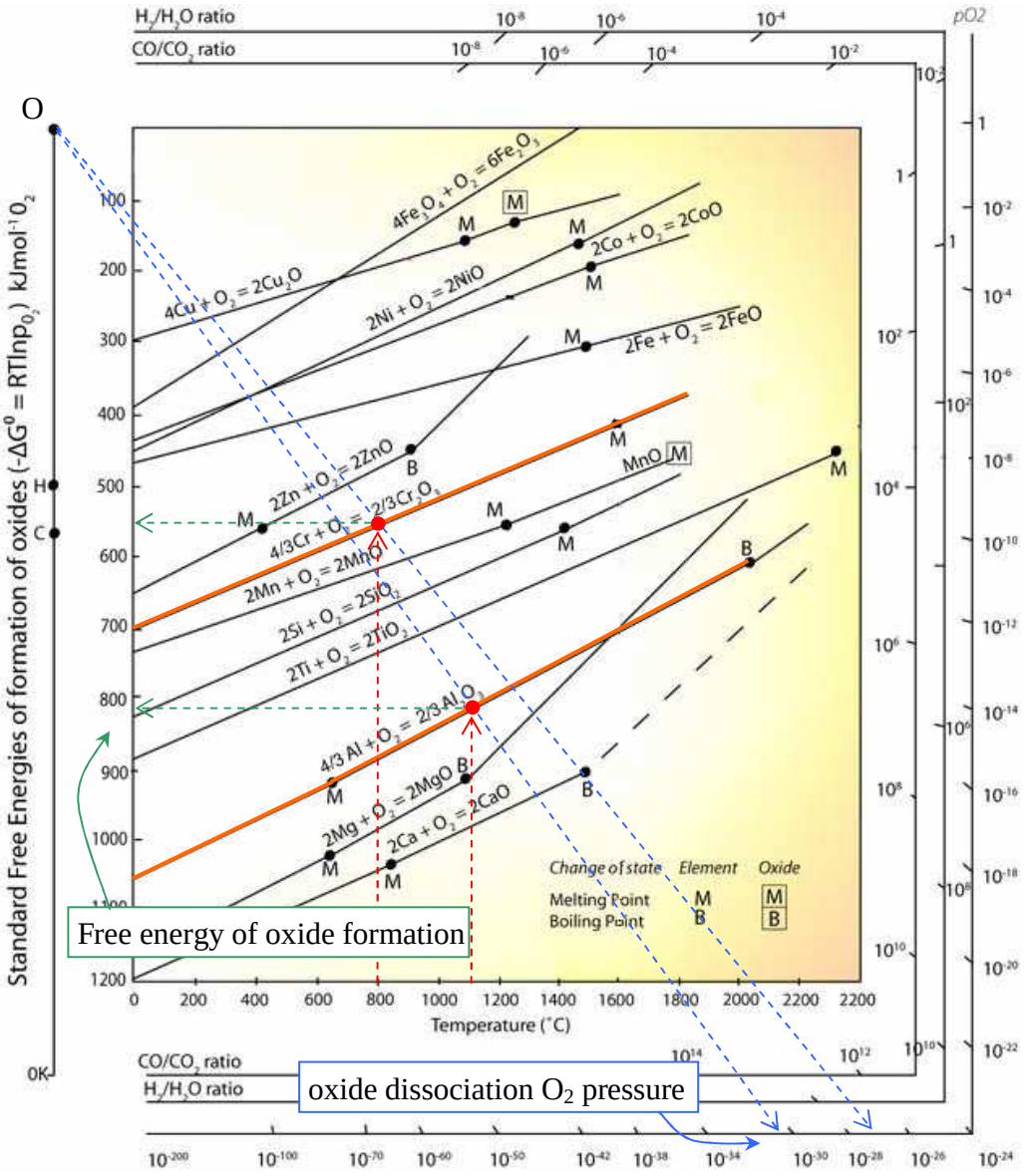

Figure 1.5: Ellingham diagram with emphasis on data for chromia and alumina formation at 800 and 1100°C, respectively.

1.4.2 High-temperature oxidation of resistant metallic alloys

However at high temperatures, these protective oxide scales do not stop the oxidation process whose kinetics is much faster. The metal substrate is continuously attacked and the long-term integrity or reliability of the metallic component is jeopardized. Therefore ceramic compounds are used in the most extreme cases. Being oxides themselves, they are intrinsically more stable in an oxidizing atmosphere. But on the other hand, ceramics present several limitations: They are expensive to fabricate and hard to form, and they exhibit low thermal and electrical conductivities. Therefore metallic alloys are preferable, and the development of oxidation-resistant materials at high temperatures is very promising for the industry. In solid oxide fuel cells, the replacement of ceramics with metallic alloys will allow for cheaper and better performing interconnects, while in thermal barrier coatings used in engines or turbines, the development of more resistant alloys will allow for an increase of the internal device temperature, thus increasing its energetic efficiency (see corresponding chapters).

Oxidation-resistant metallic alloys rely on the slow growth of a compact and adherent oxide scale of expected composition. It must present low permeabilities to the reactive species so that as the oxide scale thickness increases, it slows down the oxidation process, thus limiting the oxidation extent at long term. Complex alloys are used in order to meet desired properties and maintain low cost. The development of a specific oxide phase then relies on selective oxidation: the composition of the metallic alloy is designed to ensure that the most stable oxide in the given environment is the desired one. Thus, high aluminum or chromium content are necessary to form alumina or chromia scales at high temperature, but they do not need to be dominant in the composition.

The high-temperature long-term oxidation of metallic alloys under isothermal conditions typically follows a parabolic rate law. An example oxidation curve is given in Figure 1.6 for an oxidation-resistant commercial alloy used in a SOFC environment (Kurokawa, Kawamura et al. 2004). The oxide scale growth is slow, the thickness reaching typically a few micrometers after a few hundreds of hours. The parabolic rate law indicates that the oxide scale growth is controlled by one or several diffusion phenomena through the oxide scale and not by chemical reaction kinetics or transport outside of the oxide scale ((Huntz 1995), see model in next section). The two chains of processes which can ensure the growth of a compact oxide scale are presented in Figure 1.7: outward diffusion of the metallic cation and oxidation at the external interface with adsorbed oxygen atoms, or inward diffusion of the oxygen anion and oxidation at the internal interface. In addition, the diffusion in the substrate of the metal species consumed in the oxide scale formation, and of oxygen which can enter the metal phase in solid solution or form internal oxides, are also likely to influence the kinetics of the scale growth.

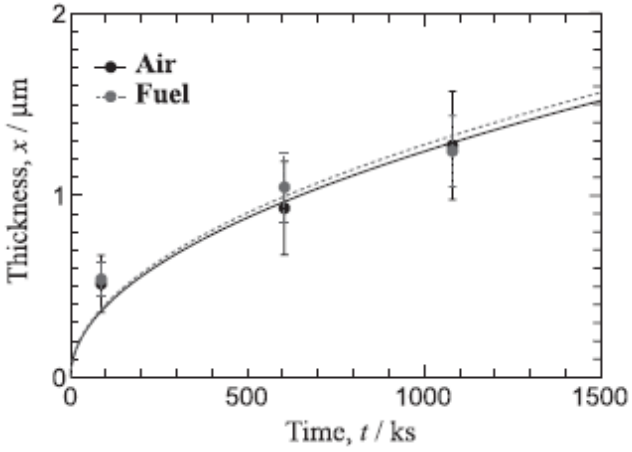

Figure 1.6: Scale thickness of SUS430 after oxidation in air and fuel at 1073 K.

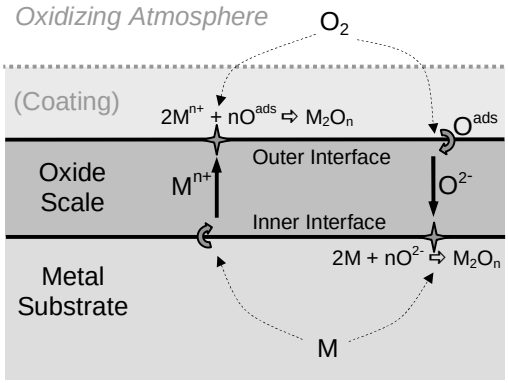

Figure 1.7: Schematic of the two main chains of processes leading to oxide scale growth.

1.4.3 Kinetics model of steady-state high-temperature oxidation

In first approximation, the long term high-temperature oxide scale growth can commonly be described by a parabolic law:

$$x_{ox}^2 = k_{p,l} \cdot t \quad \text{or} \quad \left(\Delta M / S\right)^2 = k_{p,m} \cdot t \tag{1.5}$$

where x_{ox} is the thickness of the oxide scale formed; $k_{p,l}$ and $k_{p,m}$ are the mass and length parabolic rate, respectively; $\left(\Delta M / S\right)$ is the mass gain per unit surface area; and t is the oxidation time. This regime is referred to as steady-state oxidation, corresponding to the slow progressive growth of a compact oxide scale. The mass formulation is the most commonly encountered, since practically it is much easier to monitor the change in weight of the oxidized sample than to measure a mean oxide scale thickness. The change in mass results from the absorption of oxygen by the metal sample during oxidation. It can be related to a mean oxide scale thickness through:

$$\frac{x_{ox}}{\Delta M / S} = \frac{1}{\rho_{\mathrm{M}_n\mathrm{O}}}\left(\frac{M_{\mathrm{M}_n\mathrm{O}}}{M_{\mathrm{O}}}\right) \tag{1.6}$$

where ρ represents the mass density and M the molar mass. The approximate parabolic constants ratio in commonly used units is for chromia:

$$\frac{k_{p,l}\left[\mathrm{m}^2/\mathrm{s}\right]}{k_{p,m}\left[\mathrm{g}^2/\mathrm{cm}^4\mathrm{s}\right]} \approx 3.7\times10^{-5}$$

For instance, the parabolic long term rate constants for chromia-forming alloys around 800°C in air are of the order of 10^{-12}-10^{-14} $g^2cm^{-4}s^{-1}$, or 10^{-17}-10^{-19} m^2s^{-1} (Fergus 2005).

The predictive capacity of the empirical parabolic rate law is limited, since the parabolic rate needs to be experimentally measured over a significant time period (typically few hundreds of hours) to accurately describe the long term growth. Therefore modeling the oxidation kinetics in terms of materials and environment properties is a key step in developing predicting capabilities. The parabolic rate law can easily be derived by considering:

– a steady-state Fickian diffusion through the oxide scale with fixed boundary concentrations,

– a Stefan's boundary condition at the evolving boundary.

The derivation is provided here. Let's consider a one dimensional oxide scale growth controlled by the mass transport of one species through the growing scale. Fick's first law of diffusion relates the flux vector of a species *i*, $\mathbf{J}_i$, to the concentration gradient, ∇C_i:

$$\mathbf{J}_i = -\mathbf{D}_i^{\varphi}\nabla C_i \tag{1.7}$$

where $\mathbf{D}_i^{\varphi}$ is the diffusivity matrix of species *i* in the material φ and is assumed uniform

through the material. The local statement of mass (species) conservation within the material, when no sink/source is present is:

$$\frac{\partial C_i}{\partial t} + \nabla \cdot \mathbf{J}_i = 0 \tag{1.8}$$

where t is the time variable and $\nabla \cdot$ represents the divergence operator. This statement indicates that at steady-state and in a one-dimensional problem, the diffusion flux must be uniform through the material. From Fick's first law, using superscripts *I* to denote the metal/oxide interface and *II* to denote the oxide surface (values are to be taken on the oxide side of the discontinuities), the steady-state diffusion flux of species i through the oxide scale of thickness l is given by:

$$J_i = D_i^{ox} \frac{C_i^{II} - C_i^{I}}{l} \tag{1.9}$$

It is now furthermore assumed that the oxide scale growth is controlled by the mass transport of solely one species. The normal propagation velocity, v_n, of a phase boundary whose motion is driven by mass transport is obtained through the mass conservation statement for the phase formation controlling species at the interface:

$$v_n = \frac{J_{in} - J_{out}}{C_{created} - C_{replaced}} \tag{1.10}$$

where J_{in} and J_{out} are the mass fluxes arriving and leaving at the interface, respectively, and $C_{created}$ and $C_{replaced}$ are the species concentration in the created and replaced phase (if any), respectively. This equation is sometimes referred to as Stefan's law (Stefan 1889).

Denoting I_v the moving interface and assuming a negligible solubility for the species in the replaced phase ($J_{out} = 0,\ C_{replaced} = 0$), the pseudo-steady-state interface velocity is:

$$v_n = \frac{dl}{dt} = \frac{D_c^{ox}}{l} \frac{\left(C_c^{II} - C_c^{I}\right)}{C_c^{I_v}} \tag{1.11}$$

where subscript *c* denotes the controlling species (oxygen at the inner interface *I*, the oxide-constituting metal cation at the surface *II*). The time integration of equation (1.11) with zero initial conditions yields:

$$l^2 = k_{p,l} \cdot t \quad \text{with} \quad k_p = 2D_c^{ox} \frac{\left|C_c^{II} - C_c^{I}\right|}{C_c^{I_v}} \tag{1.12}$$

The parabolic rate law is thus obtained, depending on the diffusivity and the boundary values for the diffusion through the oxide scale of the oxidation limiting species.

A finer derivation is provided by the celebrated Wagner theory (1933, (Wagner 1933)) on thick oxide film growth during high temperature oxidation of metals. The main assumptions of the theory are listed below (Atkinson 1985; Birks, Meier et al. 2006):

- The oxide scale is compact, perfectly adherent.
- Transport across the oxide scale, through diffusion/migration of ions or electrons, is the rate controlling process.
- Thermodynamic equilibrium is established at metal substrate/oxide scale and oxide scale/gas interfaces.
- Thermodynamic equilibrium is established locally throughout the scale.

- The oxide scale presents only small deviations from stoichiometry and the defect density is sufficiently low to consider the moving species to be in an ideal solution.
- A pseudo-steady-state is assumed, and there is no divergence in the ionic and electronic currents within the scale.
- The scale is thick compared with the distance over which space charge effects occur.

Local electrical neutrality has not been assumed in Wagner's theory, but practically results from the assumptions. Attention must be paid to the fact that the last assumption provides a significant limit for the theory's validity, depending notably on the charged defect concentrations (Atkinson 1985). Indeed, the Nernst-Einstein relationship used to describe charged species diffusion is only valid for scales (or grains in polycrystals) of dimensions much greater than 20 nm. This constitutes an absolute limit of the theory, but according to Atkinson a film thickness greater than about 1 μm for temperatures above 500°C is required by the local equilibrium assumption (Atkinson 1985). The reality of oxide scale growth is very complex and provides several other limitations to the theory (Huntz 1995), but the model has proved to satisfactorily describe the growth kinetics.

Based on the previous assumptions, it is possible to eliminate from the coupled transport equations the electric field and all the chemical potentials except one (a comprehensive derivation is provided by Birks et al (Birks, Meier et al. 2006)), which is generally conveniently taken to be the one of oxygen. In the case of a pure electronic conductor (as are chromia scales above 700°C (Liu, Stack et al. 1998)), and for an $MO_{n/2}$ oxide, the parabolic rate constant can be expressed from Wagner's theory by:

$$k_p = \frac{1}{R\theta}\int_I^{II}\left(\frac{n}{2}D_{\mathrm{M}} + D_{\mathrm{O}}\right) d\mu_{\mathrm{O}} \tag{1.13}$$

where *I* and *II* refer again to the internal (metal/oxide) and external (oxide/gas) interface, respectively, D represents the species diffusivity through the oxide scale and μ the chemical potential. Then, relating the oxygen chemical potential to the oxygen partial pressure (Birks, Meier et al. 2006),

$$\mu_{\mathrm{O}} = \frac{1}{2}\left(\mu^{\circ}_{\mathrm{O}_2} + R\theta \ln P_{\mathrm{O}_2}\right) \tag{1.14}$$

it yields:

$$k_p = \frac{1}{2}\int_I^{II}\left(\frac{n}{2}D_{\mathrm{M}} + D_{\mathrm{O}}\right) d\left(\ln P_{\mathrm{O}_2}\right) \tag{1.15}$$

It is worthwhile to note that the two terms in the parabolic rate correspond to scale growth at the two interfaces respectively (internal for O and external for M), and thus are not competing processes. The two boundary pressures correspond to the dioxygen partial pressure in the reaction gas, which depends on the experimental atmosphere (from 0.2 atm for air to 10^{-22} atm for H_2/H_2O fuel at 800°C for instance), and to the oxygen partial pressure at the scale/alloy interface, which is typically assumed to be the fixed (at constant temperature) alloy/oxide decomposition pressure (around 10^{-27} atm at 800°C for chromia/chromium and 10^{-31} for alumina/aluminium at 1100°C, see Figure 1.5).

1.4.4 Species diffusion in oxide scales at high temperature

As can be inferred from the previous section, prediction of oxide scale growth kinetics at high temperature relies in large part on the knowledge of species diffusivities

through the oxide scale. It is important to mention here that chromia or alumina scales developed on metallic alloys at high temperature exhibit a polycrystalline nature. Therefore, two paths are available for diffusion: through the grain lattice bulks or along the grain boundaries. While grain boundaries occupy a very low volume fraction of the oxide scale, they exhibit very high diffusivities such that the grain boundaries' contribution cannot be neglected and even often dominate at the considered oxidation temperatures (Tsai, Huntz et al. 1996).

Data and information on diffusion mechanisms are mainly extracted from three sources. The most direct is tracer diffusion, which provides diffusion coefficient data from the fitting of theoretical curves, based usually on Fick's law, with experimental concentration profiles (Atkinson 1985; Huntz 1995; Tsai, Huntz et al. 1996; Sabioni, Huntz et al. 2005). The results are therefore attached to a diffusion model, and thus constitute only semi-experimental values. While reading these data, special attention should be paid to the nature and preparation of the oxide material (is it a made up sample or a scale developed by oxidation, in what conditions and during how much time, is there a significant concentration of 2D or 3D defects, like dislocation, micropores, microcracks…), and on the diffusion experiment conditions (temperature, atmosphere). This remains obviously true for the analysis of other data.

Conductivity measurements are relevant experimental data for the identification of the dominant diffusion mechanism. The material electrical conductivity variation with temperature and/or atmospheric oxygen pressure is monitored. From the first results, activation energies are extracted (a change in value revealing a change of dominant process), and from the second, dependencies relevant to the defects' thermodynamic

equilibriums are identified (Holt and Kofstad 1994; Birks, Meier et al. 2006). Conductivity data are then related to diffusion through the theory of point defect equilibrium. This theory, applied to the bulk of ionic crystals, like any metal oxide, considers that material transport occurs only through charged point defects. However, higher dimensional non equilibrium defects (like dislocations, pores) will always be present in addition in practical materials, even if their concentration can be reduced by high temperature annealing. It is important to mention also that the situation may be different in, or in the vicinity of grain boundaries. Therefore the theory only exactly applies to bulk lattice diffusion.

Two kinds of point defects are to be considered: ionic point defects, which are cation or anion vacancies and interstitials; and electronic point defects, constituted of electrons and electron holes. These defects are generated or annihilated during electrochemical reactions, which take place mainly at the oxide scale surface or interface. The thermodynamic equilibriums of these reactions, coupled with a local electroneutrality (consequence of the predominance of electrostatic forces and the high mobility of electronic defects), are the base of the theory which is notably used in the Wagner's law derivation.

Finally, estimates of diffusion coefficient values and dependencies can be extracted from oxidation kinetics parabolic rate data, by matching a kinetic model as derived previously with experimental results. While this method constitutes the most uncertain source, the large amount of available data makes it useful to identify the global influence of certain parameters.

Diffusion data, obtained directly or indirectly through experiments, have demonstrated significant variations with alloy constitution, including particular sensitivity to some minor element contents, alloy preparation (microstructure, surface state), oxidizing atmosphere (Atkinson 1985; Dieckmann 1998). Furthermore, defect concentration and nature can vary along the scale thickness, and the oxide scale itself can present varying microstructure and composition in space and time, possibly resulting in a modification of the diffusion mechanism. The difficulty of assessing the main diffusion mechanisms and the lack of understanding of the role and contribution of the different parameters prevent any general modeling of these key data that are the diffusion coefficients, and thus will fail the prediction capability of a general oxidation kinetics model (Atkinson 1985; Heuer 2008). Therefore empirical or phenomenological formulations are fitted with experimental data for practical descriptions.

1.5 Stress development and mechanical failure

While decreasing the oxide scale growth kinetics has been an essential step for the development of metallic alloys sustaining an oxidizing atmosphere at high temperature, satisfactory progress has been made, and most current efforts now concentrate on increasing the oxide scale lifetime. Different phenomena might limit its functional lifetime depending on the required properties. For instance, chemical degradation which may include pores and holes formation, or the development of detrimental properties of the oxide scale, notably due to the formation of undesired phases, might lead to the oxide

scale loosing its low permeability to reactant species or to a loss in electrical conductivity (an important property for an SOFC interconnect).

In this work, we focus on stress development leading to mechanical failure of the oxide scale, which results in the detrimental exposure of the substrate alloy. The lifetime of growing oxide scales is often limited at mid or long term by intrinsic mechanical failure. In thermal barrier coatings, stresses developing in relation with the oxide growth lead to the development of large deformations with thermal cycling; these eventually result in the local delamination, failure and spallation of the thermal barrier coating, which may expose the structural metallic alloy to an unsustainable temperature (Padture, Gell et al. 2002; Evans, Clarke et al. 2008). This mechanism is presented in Figure 1.8 (Karlsson, Hutchinson et al. 2002). In the case of uncoated SOFC interconnect alloys, stress development directly results in local oxide scale spallations and failures. A typical route to failure for an oxide scale grown on a regular alloy is illustrated in Figure 1.9 (Suo 1995). As shown on the schematic and depending on the environment, the metallic substrate might be able to heal itself by reforming a protective oxide scale. Nevertheless, this could lead in time to a loss of electrical conductivity, fuel conduct obstruction or severe consumption of the metallic component, potentially jeopardizing its reliability (Belogolovsky, Hou et al. 2008).

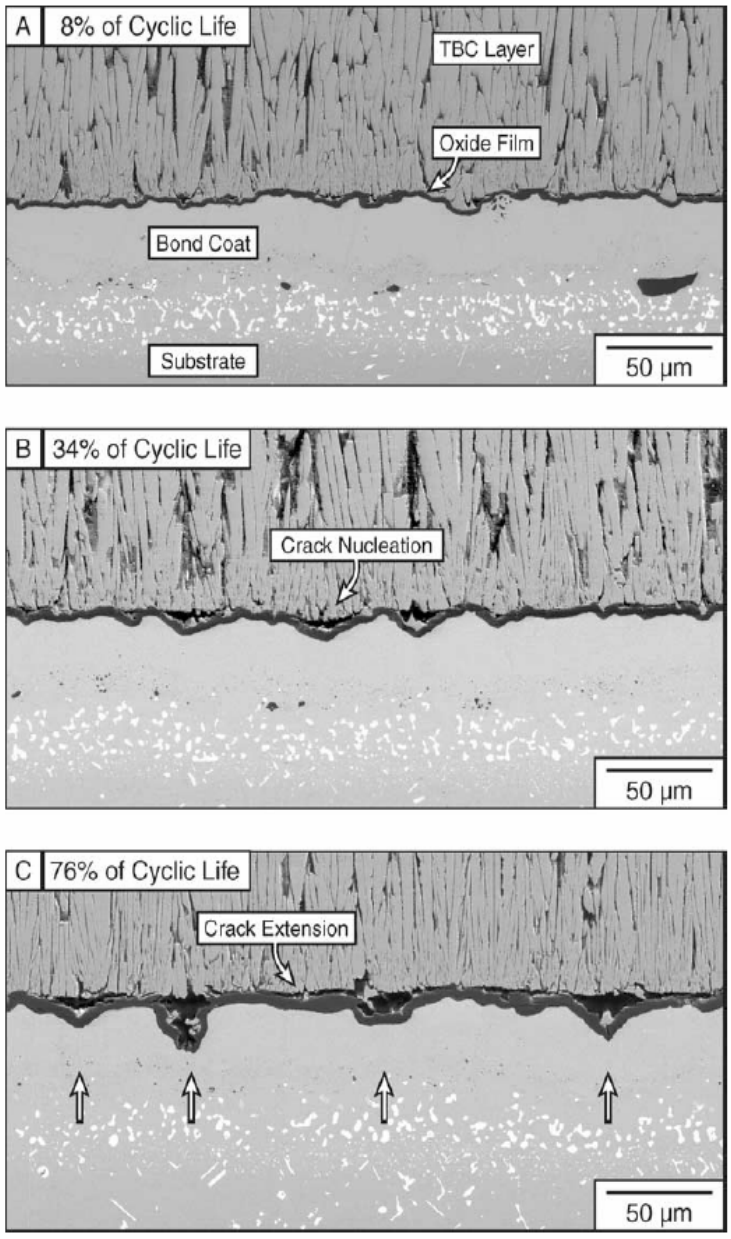

Figure 1.8: Cross-section SEMs presenting an example of oxide scale large deformations with thermal cycles in a TBC system. The phenomenon leads to in-plane crack nucleation and extension and eventually results in the thermal coating spallation.

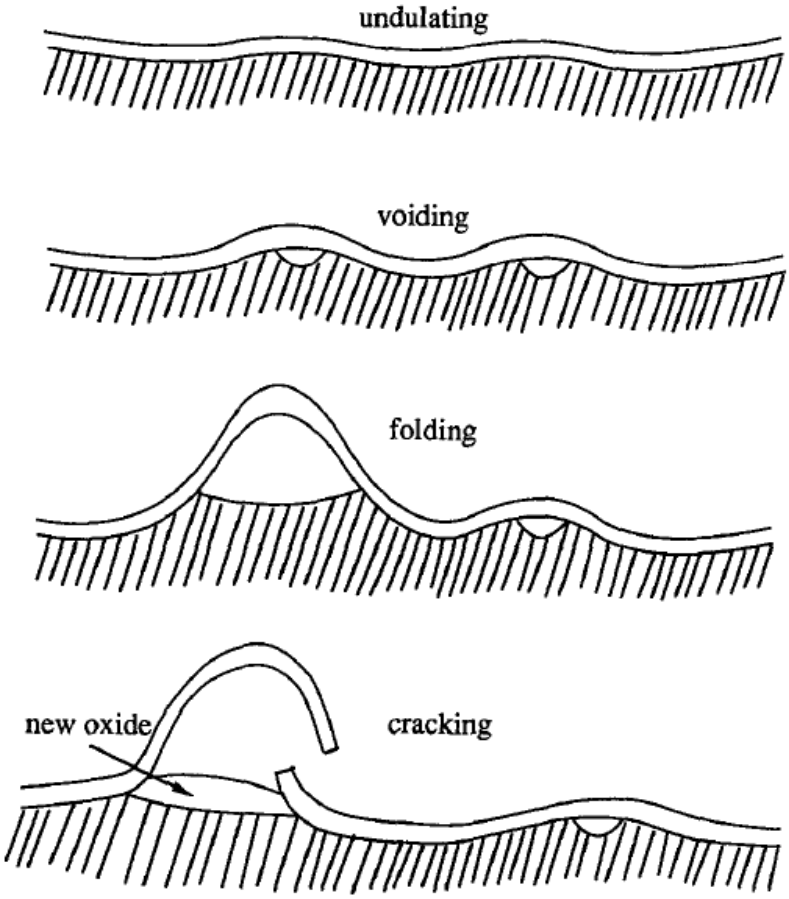

Figure 1.9: Cross-section sketches presenting an oxide scale undulation, spallation and failure during isothermal oxidation.

Intrinsic stresses in oxide/metal systems can be separated into two types, depending on their origin: stresses developed during scale growth at oxidation temperature (growth stresses) and those developed during cooling/heating sequences on account of the differences between the thermal expansion behaviors of the scale and the underlying substrate (thermal mismatch stresses). Stresses can also result from a temperature gradient between the scale and its substrate, but are not likely to be dominant in our cases

of interest due to the very limited thickness of the oxide scale and the good thermal conductivity of the metallic substrate. Finally, it is worth mentioning that in the case of non planar systems, stresses might be induced by the oxide growth over a non-uniform geometry (Evans 1995). “External” stresses might also be induced by the deformation of the system, for instance as a consequence of the substrate creep under an applied load.

1.5.1 Stress measurement

While evidence of stress development, such as sample elongations or bending, oxide scale buckling and spallations, can be observed, direct measurements of stresses within oxide scales are not easily obtained. Therefore different techniques have been developed in order to measure associated relaxation strains, such as specimen extension tests, catenary and deflection methods (see (Evans 1995) for a brief review). In-situ measurements during oxidation at high temperature present several difficulties, and therefore historically most measures have been taken at room temperature, preventing a direct assessment of growth stresses. Analytical models available for thermal stresses are then used to recover stresses developed during the oxidation, but the accuracy of the estimate then relies on the knowledge of the thermal expansion coefficients of the different materials (see the model described further). Uncertainty is then introduced since the materials are evolving at high temperature and might develop a non-homogeneous structure. This is especially true for the oxide scale, which is forming during the experiment and remains very thin, and can therefore present significantly different properties than larger and differently made samples (see for instance (Mougin, Galerie et al. 2002)).

Over the last decade, in-situ measurements have been performed during high temperature oxidation, allowing for a better assessment of growth stresses (Mougin, Rosman et al. 2001). X-ray diffraction (XRD) is the most common technique for stress measurements. The strain is measured as a change in lattice spacing, for a given inclination with respect to the sample surface, from the stress-free situation. It is important to note here that the need for this reference state constitutes a limit to the method in cases where the composition of the oxide is complex and might evolve with time.

Since the technique relies on the detection of a change in lattice spacing, a lower limit exists on the stress measure resolution, estimated to be around or greater than 100MPa depending on the oxide considered (Evans 1995). The spatial resolution also presents a limit to the measurement. Since the incident beam penetrates up to a certain depth within the sample, the values obtained are averages over a surface layer. This vertical resolution is typically greater than 1µm, which prevents accurate mean stress measurements in thinner oxide scales. It is important to notice that a reverse consequence of this limitation is that for thicker scales, only an average stress over a surface layer of given thickness is measured.

Recently other techniques have been developed for stress measurement. Laser Raman spectroscopy has been employed for chromia scales (Birnie, Craggs et al. 1992). This technique has the advantage compared to XRD that it does not require a specific environment (a simple laser is used) and that it presents better lateral and vertical resolutions, thus allowing for stress measurements in thinner oxide scales (Kemdehoundja, Grosseau-Poussard et al. 2008). For alumina scales, photostimulated

chromium luminescence spectroscopy has been proved efficient for stress measurement (Lipkin and Clarke 1996), and might allow notably for the measurement of stresses developed in the oxide scale below the thermal barrier coating (Christensen, Lipkin et al. 1996; Zhao and Xiao 2007). Despite the progress made in stress measurement techniques, major limitations remain and render models and simulations essential to get insights on the likely stress development and resulting mechanical failure mechanisms.

1.5.2 Thermal stresses

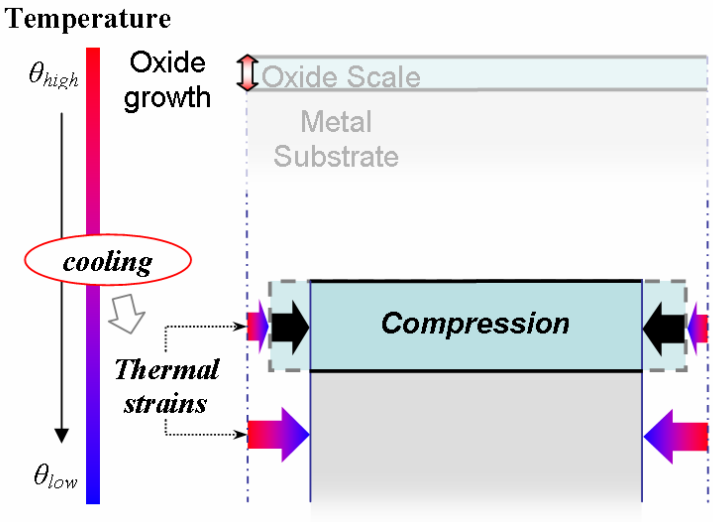

Figure 1.10: Schematic presenting the thermal strain mismatch induced upon cooling between the developed oxide scale and the metallic substrate, and the in-plane compression resulting from the adherence of the oxide layer.

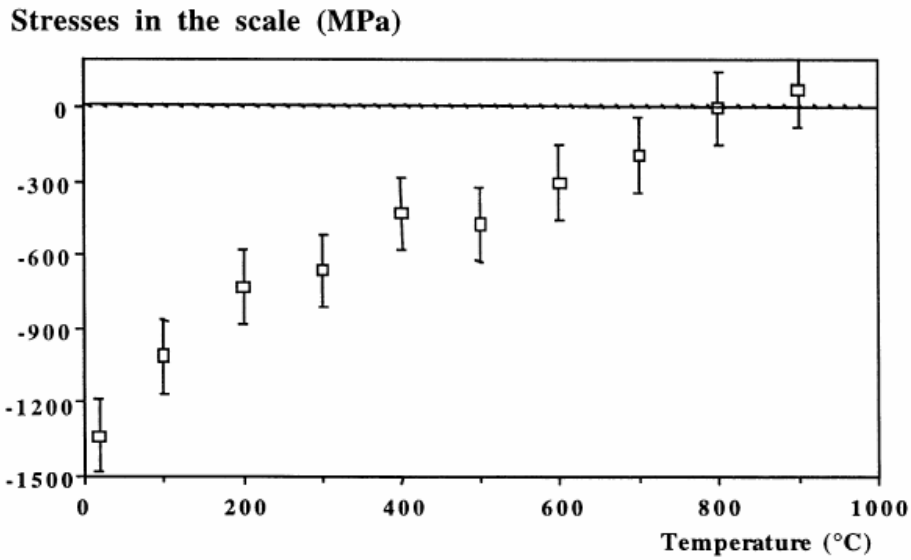

Figure 1.11: Thermal stress relaxation measured during the reheating of a metal/oxide sample. The oxide is a 1.4 µm thick chromia scale grown for 96 hours at 900°C over a 1mm thick substrate.

Thermal expansion mismatch is largely reported as the main origin for the residual stress in the oxide scales observed at room temperature, and as a consequence as the main driving force for mechanical failure. The free volumetric thermal strain corresponding to a variation in temperature from θ_1 to θ_2 is obtained through:

$$\varepsilon_{vol}^{th} = \int_{\theta_1}^{\theta_2} \alpha \, d\theta \tag{1.16}$$

where α is the isotropic thermal expansion coefficient and is a material property, which is often considered constant but might depend on temperature. It is in most cases much higher for metals than for oxides, and the larger retractation of the metal substrate then results in the compression of the adherent oxide scale, as illustrated in Figure 1.10. Figure 1.11 presents a measured relaxation of thermal stresses upon reheating of the metal/oxide scale system (Huntz, Daghigh et al. 1998). If two plane, perfectly bonded, elastic layers

in equal biaxial stress states are considered, and if it is furthermore assumed that the two materials present similar Poisson ratios and that the oxide scale thickness is small in front of the metal one, the in-plane stress in the oxide scale can be expressed by (Birks, Meier et al. 2006):

$$\sigma_{ox} = \frac{-E_{ox}\left(\alpha_{ox} - \alpha_{met}\right)\Delta\theta}{1-\nu} \tag{1.17}$$

where the subscripts *ox* and *met* refer to the oxide and metal layers, respectively, E is the Young Modulus of elasticity and ν the Poisson ratio. This formulation allows predicting compressive in-plane stresses upon cooling from thermal coefficients data. The stresses can reach several gigapascals, in agreement with experimental measurements, see for instance Figure 1.12 (Lipkin, Clarke et al. 1997). Stresses up to 6 GPa have been reported for alumina scales (Evans, Clarke et al. 2008). Consequently alloys are selected and designed in the first place to match as closely as possible the thermal expansion behavior of the oxides they develop and to be mechanically resistant enough to sustain the inevitable thermal mismatch stress (Yang, Weil et al. 2003; Evans, Clarke et al. 2008).

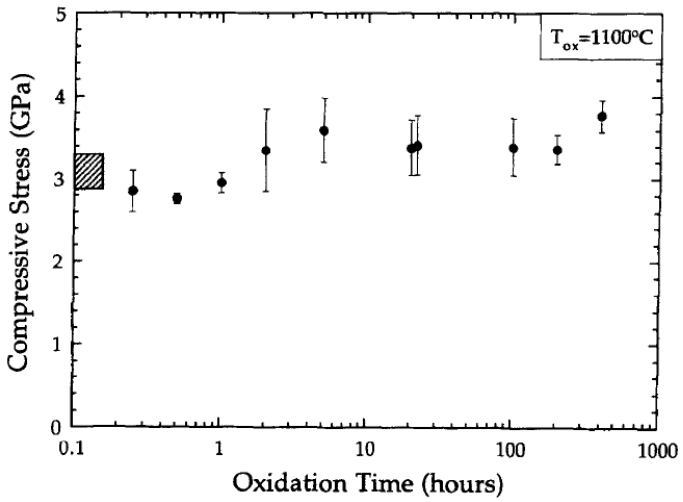

Figure 1.12: Mean stress in the oxide scale measured under a TBC by luminescence spectroscopy. The error bars indicate the standard deviation with measurement location. For comparison, the calculated thermal stress upon cooling is indicated by the hatched box on the left axis.

1.5.3 Accommodation of in-plane compressive stress

Planar metal/oxide material systems such as those considered here usually fail in response to the development of a compressive in-plane stress within the oxide scale, as induced upon cooling to room temperature. Depending on the different material mechanical behaviors (ductile or fragile, low or high strength) and the interfaces' strengths, different mechanisms of stress accommodation might take place, as illustrated on Figure 1.13 (Sarioglu, Stiger et al. 2000).

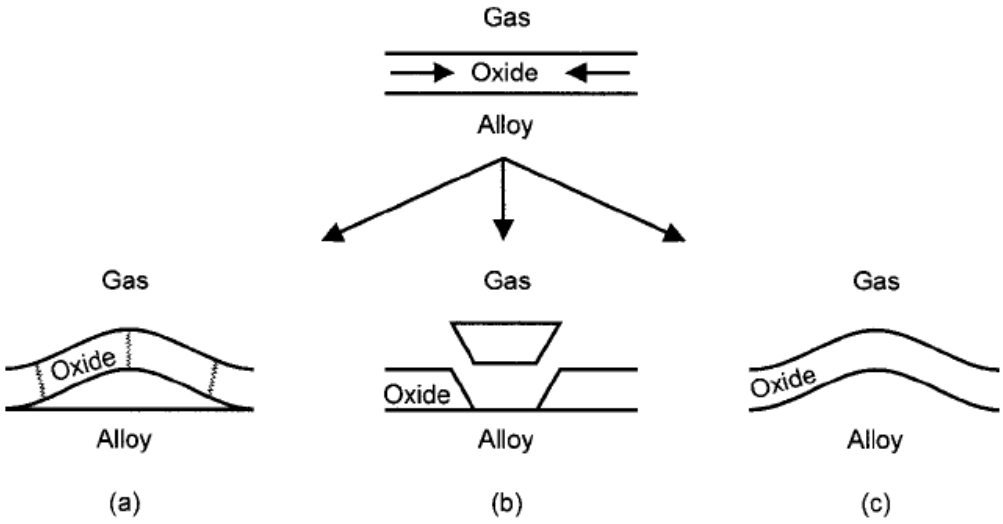

Figure 1.13: Schematics of the main responses to the development on an in-plane compressive stress in the oxide scale. (a) buckling, (b) shear cracking and (c) plastic deformation of the oxide scale and the alloy substrate.

From linear elasticity and thermodynamic considerations, the spalling of an oxide film undergoing a compressive stress is likely to occur when the elastic energy stored within the oxide scale exceeds the fracture resistance, G_I, of the interface (energy per unit surface) (Evans 1948; Birks, Meier et al. 2006). A criterion for the spallation of an oxide scale in a bi-axial symmetric compressive state can then obtained:

$$\frac{(1-\nu_{ox})}{E_{ox}}\sigma_{ox}^2 h_{ox} > G_I \tag{1.18}$$

where the subscript *ox* refers to the oxide scale, E is the Young Modulus of elasticity, ν is the Poisson ratio, σ_{ox} is the bi-axial compressive stress in the oxide scale and h_{ox} represents the oxide scale thickness. According to this criterion, oxide scale spallation is favored by a high compressive stress, a high layer thickness and a low interface strength. This simple criterion thus offers a logical understanding of the failure of a flat interface:

the thickening of the oxide layer with oxidation time renders it more likely to spall off upon cooling, a situation possibly aggravated by additional compressive stress development and the weakening of the metal/oxide interface. However, this criterion constitutes a necessary but not sufficient condition for the event, since it does not provide a mechanism leading to the oxide scale spallation. Two routes have been proposed: the development of a buckling instability or the nucleation and propagation of a wedge crack.

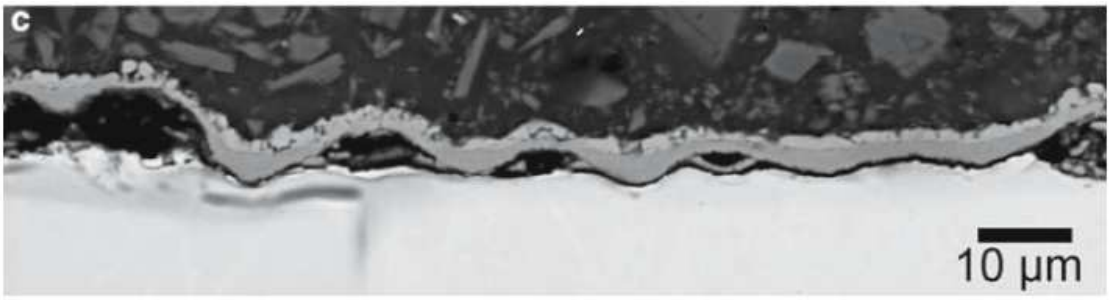

Figure 1.14: Oxide scale buckling and spallation.

Buckling, as illustrated on Figure 1.13 (a) and shown with a scanning electron micrograph in Figure 1.14, is the combined local delamination and undulation of the oxide scale. It is likely to occur when the metal/oxide interface is weaker than the oxide scale (from a resistance to failure point of view). It is a typical response for oxide scales grown on non-coated non-doped alloys. The deformation then induces local in-plane tensile stresses likely to prompt through-scale crack nucleation and propagation, eventually leading to the oxide scale failure, as shown in Figure 1.13 (a).

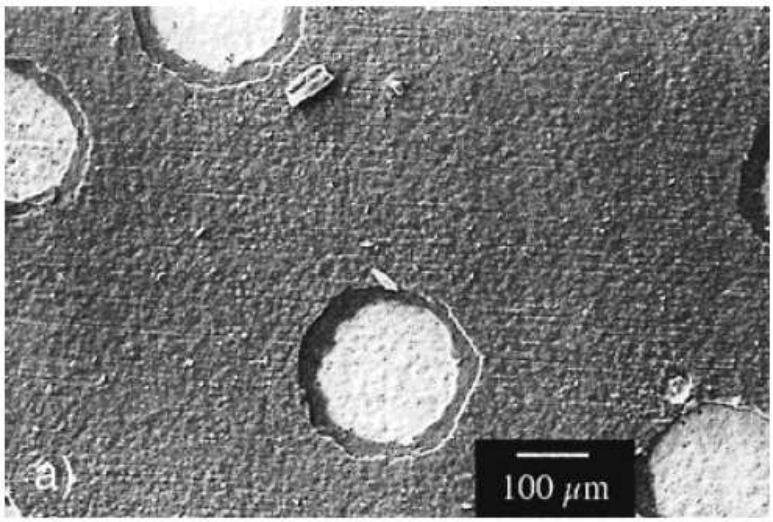

Figure 1.15: Top view showing local spallations of a flat oxide scale.

If compressive stresses are not relaxed by buckling, as it is likely to be the case when the metal/oxide interface strength is high, shear cracks might develop within the oxide scale, leading to its spallation by a wedging mechanism as illustrated in Figure 1.13 (b) (shear cracks form within the oxide scale and propagate toward the surface as well as to and along the interface until total delamination occurs). An example of local spallation of a flat scale is provided in Figure 1.15. Buckling and shear cracking are the main failure mechanisms for chromia scales at SOFC operating temperatures, around 800°C, at which limited plastic relaxation occurs within the oxide layer.

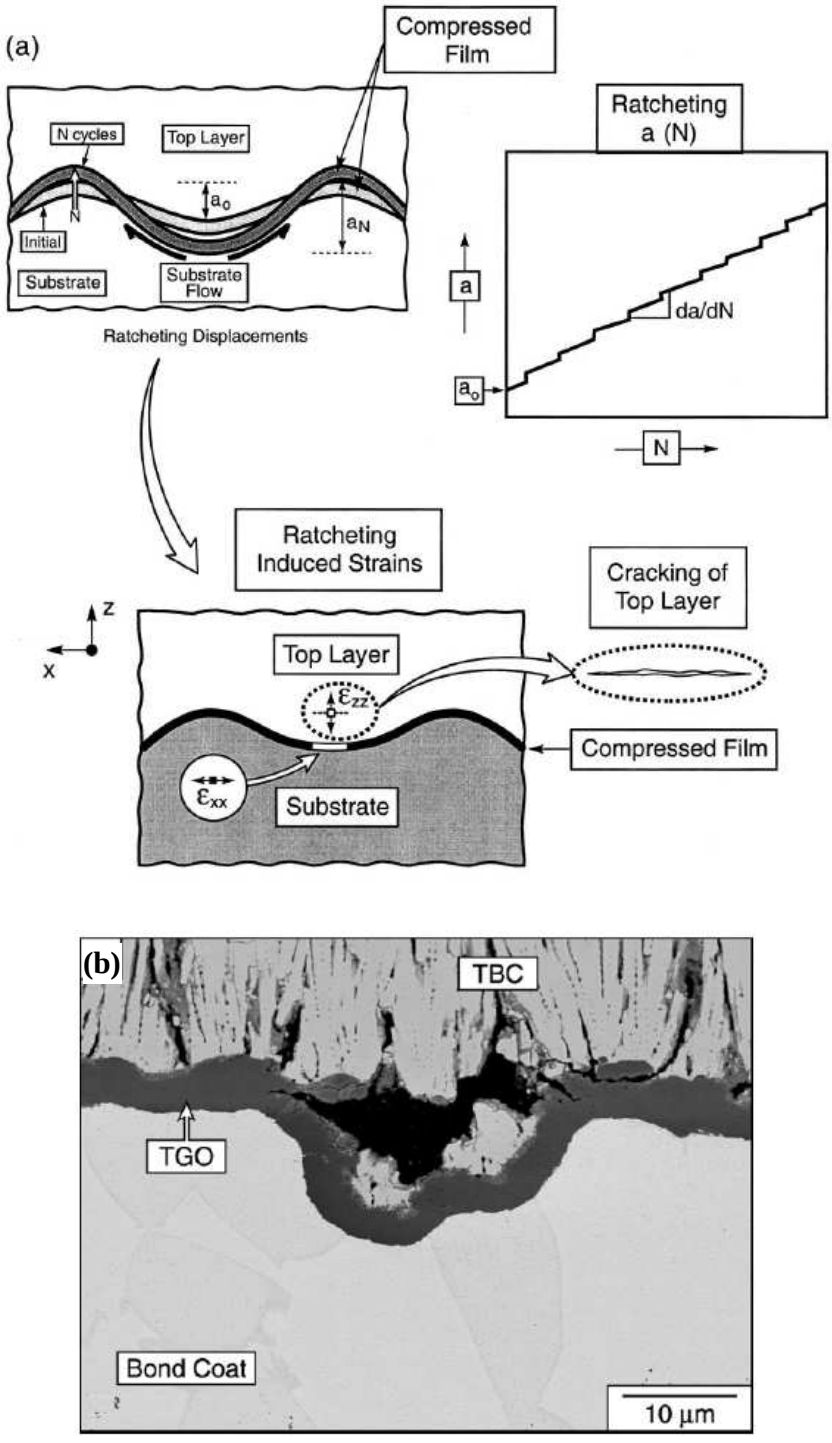

Figure 1.16: (a) Schematic of the ratcheting mechanism presenting the oxide scale deformation, the undulation amplitude growth with the number of thermal cycles, and the induced out-of-plane tensile strain likely to result in the delamination of the top coat. (b) SEM showing actual large deformation and cracks development leading to the delamination of the thermal barrier coating.

In contrast, important inelastic relaxation occurs in alumina scales growing under thermal barrier coatings at around 1100°C. Here, combined plastic deformations of the oxide and the alloy take place, restrained in the TBC environment by the thick ceramic coating. However, even limited undulations might grow with time due to thermal cycling. In fact, if thermal stresses are partially relaxed by plastic deformation upon cooling, then the oxide scale will remain deformed upon reheating, and thus its geometry will be affected at each thermal cycle. This phenomenon might lead to the development of large growing undulations, and is then referred to as a ratcheting mechanism. A schematic of the ratcheting mechanism is presented in Figure 1.16 (a) (He, Evans et al. 2000) and (b) (Evans, Mumm et al. 2001). As shown, the amplitude of the undulations increases with the number of thermal cycles, which induces growing out-of-plane tensile strains in the valley regions, likely to result in in-plane crack nucleation and propagation at interfaces or in the fragile YSZ coating and alumina scale, and eventually leading to the delamination of the protective coating.

It is worth mentioning that alloy substrate mechanical failure has not been discussed here because it is usually unlikely to occur, due to the high plasticity of the metallic materials at the considered oxidation temperature. However, vacancy diffusion and condensation at grain boundaries might weaken the polycrystalline alloy, allowing for its failure. Finally, it is important to note that in specific situations,a significant in-plane tensile stress might develop within the oxide layer. This would be the case if the material system is heated at a temperature higher than the one at which the oxide scale has grown; or if the development of a plastic in-plane shrinking deformation of the oxide layer during cooling phases is not recovered upon reheating. A simulated example of the latter

mechanism is presented Figure 1.17 (Huntz, Daghigh et al. 1998). Nevertheless, in-plane tensile situations, if they need to be explained in their origin, are much less complex regarding failure mechanisms. Indeed, on one hand they directly provide a driving force for through-scale crack nucleation and propagation; and on the other hand their relaxation should result in a flattening of the oxide layer (to maximize its in-plane dimension) and is therefore stabilizing with respect to geometrical evolution.

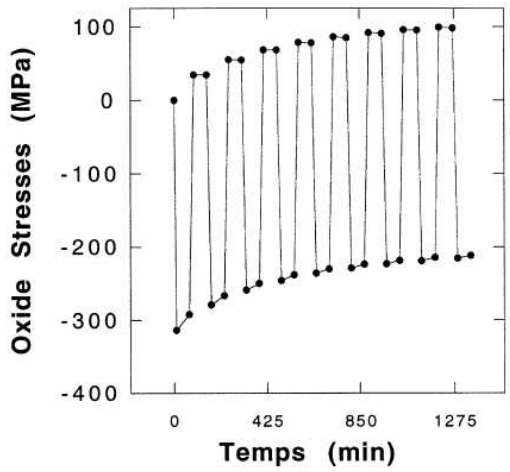

Figure 1.17: Simulation results of the in-plane stress evolution in a chromia film associated with thermal cycling during which plastic relaxation occurs. The oxide scale developed at 900°C and thermal cycles range from 900 to 800°C, with a 1 hour isothermal hold period between consecutive cycles.

1.5.4 Growth stresses

While thermal stresses are thought to be responsible for the eventual oxide scale failure in most cases, growth stresses might play a significant role in the failure mechanism. Growth stresses might contribute in two ways depending on their relaxation. They might contribute directly in constituting an additional in-plane compressive stress to the thermal stresses upon cooling, if they are not significantly relaxed at oxidation

temperature, or they might contribute indirectly in inducing oxide scale deformations resulting from growth strain accommodation at oxidation temperature. This would lead to a rougher oxide layer and consequently engender higher local tensile stresses upon cooling, an effect similar to that of the ratcheting mechanism. A schematic of the varying in-plane and out-of-plane stress fields along the oxide layer induced upon cooling by the scale roughness and the resulting effects on failure for an uncoated system is presented in Figure 1.18 (Mougin, Lucazeau et al. 2001).

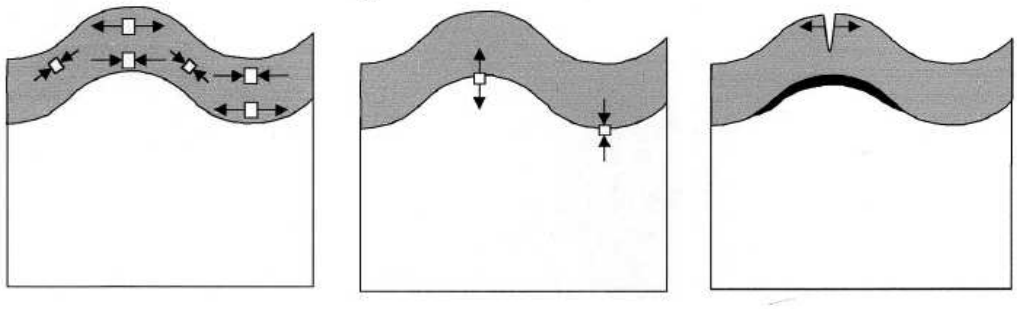

Figure 1.18: Schematic of the varying in-plane and out-of plane stresses in the oxide layer induced upon cooling by the scale roughness, and likely resulting failures.

Growth stresses are mostly in-plane compressive, although a tensile state might arise in specific situations (see the discussion on the origins of growth stresses further), and they might reach important levels. Stresses up to few GPa have been measured when relaxation processes are limited (Christensen, Lipkin et al. 1996; Tolpygo, Dryden et al. 1998; Sarioglu, Stiger et al. 2000; Mougin, Galerie et al. 2002; Kemdehoundja, Grosseau-Poussard et al. 2007). An example of growth stresses in an alumina scale growing at 1000°C, measured in-situ by XRD as a function of oxidation time is presented in Figure 1.19 (Sarioglu, Stiger et al. 2000). In a case representative of SOFC

interconnect conditions, in-situ measurements by Raman spectroscopy on a Fe-18Cr ferritic stainless steel oxidized at 750°C showed compressive growth stresses in the chromia scale of more than 2GPa, almost ten times greater than the thermal stresses (Mougin, Galerie et al. 2002). This situation is shown in Figure 1.20 presenting the stress evolution during cooling.

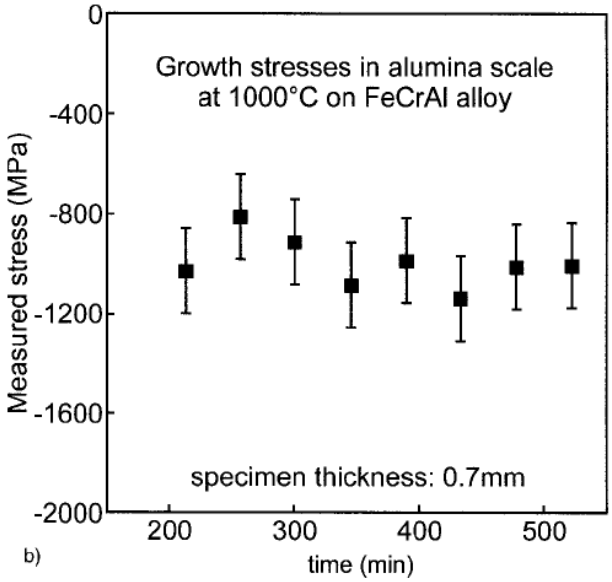

Figure 1.19: Growth stresses in an alumina scale growing at 1000°C as a function of oxidation time, measured by XRD.

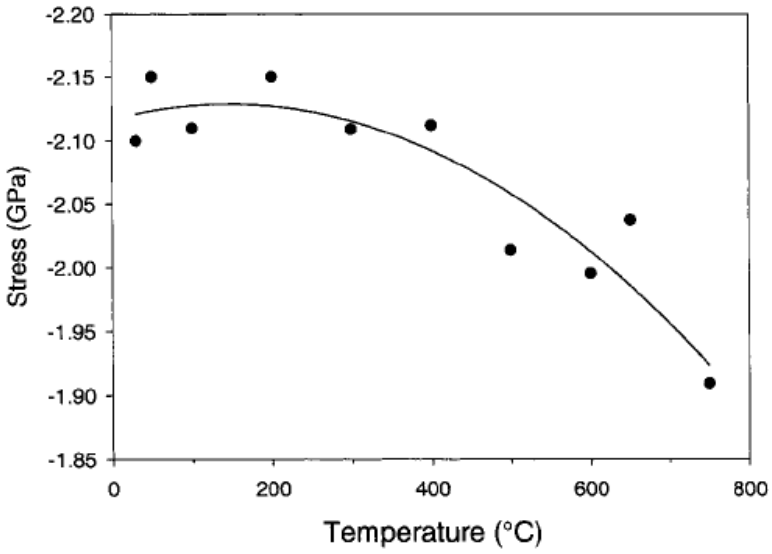

Figure 1.20: Raman spectroscopy measurements showing the evolution during cooling of the stress state of a chromia scale grown on a stainless steel sample for 3 hours at 750°C.

Growth stresses have also been shown to play a key role in oxide scale deformation mechanisms during isothermal oxidation. In fact, convolutions (wrinkling) or buckling of the oxide scale have frequently been reported as mechanisms of growth strain accommodation (Kofstad and Bredesen 1992; Clarke 2002). At high temperature, strong inelastic relaxation processes might counteract the development of growth stresses by accommodating the underlying strain, then possibly inducing morphological evolutions. Significant defect diffusion allowing for high creep rates, and low resistance to plasticity particularly in the metallic alloy, might thus maintain a quite limited stress level in the oxide scale. Nevertheless, such processes can on the other side lead to large deformations of the system with time, such as substrate extension, grain uplift, oxide scale wrinkling (undulations) or ridging, or also result in voids and porosity development (Caplan and Sproule 1975; Tolpygo and Clarke 1998; Clarke 2002).

At moderate temperatures (especially below 800°C), the contribution of creep might be reduced. However, significant effects have been observed even in this temperature range. Thus, Huntz et al. (Huntz, Daghigh et al. 1998) quantified significant creep relaxation for a chromia scale in the range 700-900°C. Figure 1.21 presents growth stress development and relaxation at short term, as measured in-situ during the growth of a chromia oxide layer on a Ni-30Cr substrate at different temperatures (Kemdehoundja, Grosseau-Poussard et al. 2007). Finally, it is worth noting that even during thermal cycling, a growth strain has been shown to be essential to the ratcheting mechanism (increase of undulations amplitude with thermal cycles) (He, Evans et al. 2000; Tolpygo and Clarke 2000). Thus growth stresses undoubtedly constitute a basic driving force for the processes leading to mechanical failure under functioning conditions.

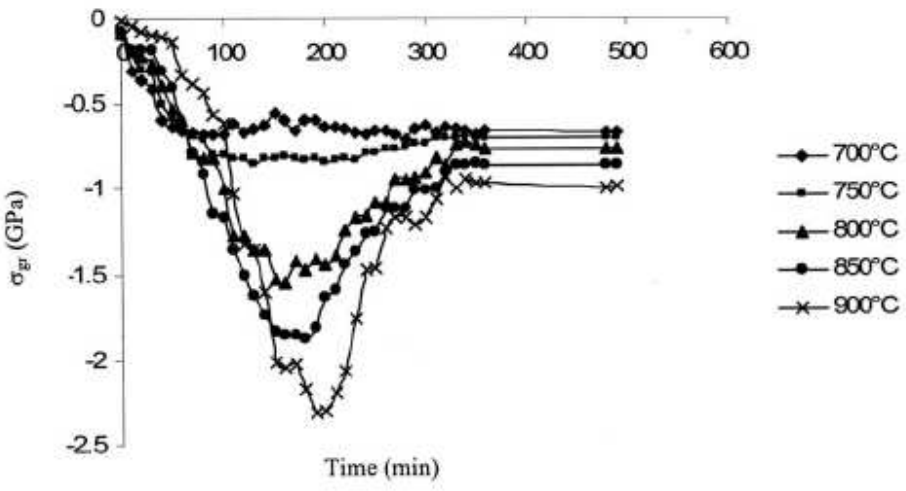

Figure 1.21: Growth stress development and relaxation with time, as measured in-situ during the growth of a chromia oxide layer on a Ni-30Cr substrate at different temperatures.

The possible origins of growth stresses have been reviewed by many authors over the last decade (Stott and Atkinson 1994; Evans 1995; Huntz 1995; Clarke 2002; Panicaud, Grosseau-Poussard et al. 2006). The most cited are the epitaxial relationship between the metallic substrate and the oxide scale, compositional changes due to species diffusion, the oxidation process or other phase transformations, the specific volume change accompanying the metallic phase oxidation and finally new oxide formation at existing oxide scale grain boundaries within the oxide layer.

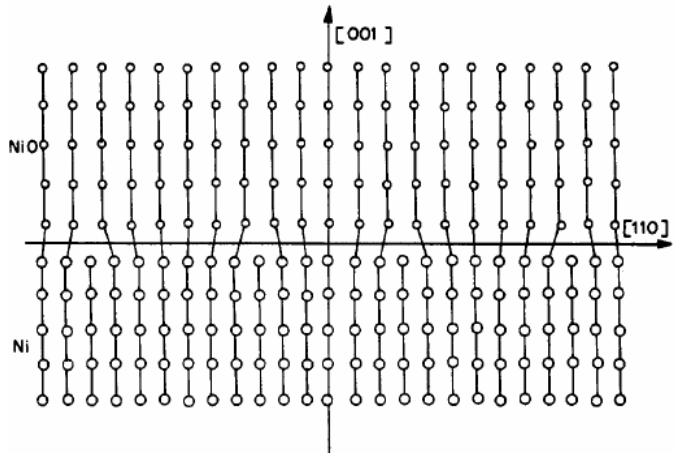

Figure 1.22: Metal lattices epitaxial arrangement through a dislocation structure for an NiO scale on a Ni substrate.

Epitaxial stresses can develop from lattice incompatibility between the nominal oxide phase and the metallic substrate. An illustrative schematic is presented in Figure 1.22 (Pieraggi and Rapp 1988). A mismatch strain necessarily accommodates the difference in lattice parameters at the interface, decreasing away from the boundary where the lattice is relaxed. This phenomenon induces stresses at the microscopic level, and is thus significant through the scale only for thin films. The stresses can be either

compressive or tensile according to the epitaxy relationship. However, the oxides formed by high temperature oxidation on oxidation-resistant metallic alloys are polycrystalline; furthermore in practice several alloying species and impurities segregate at the interface. It is therefore unlikely that coherency stresses are important, in contrast to the case of the epitaxial growth of semiconductor films on single crystal substrates (Clarke 2002).

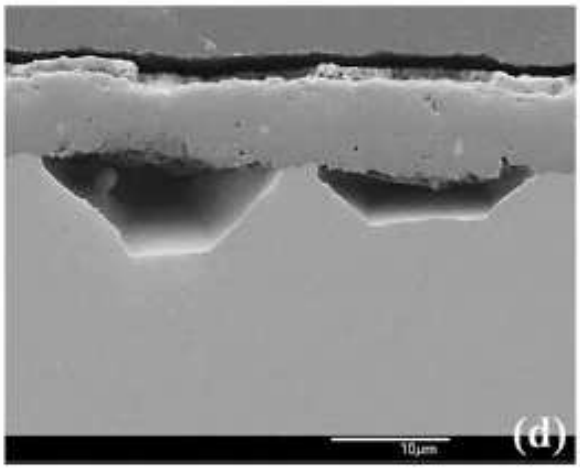

Figure 1.23: Cross-section micrograph of a bulk sample of Pt-modified NiAl after oxidation at 1150 °C for 300 hours, showing voids in the metallic substrate caused by selective oxidation.

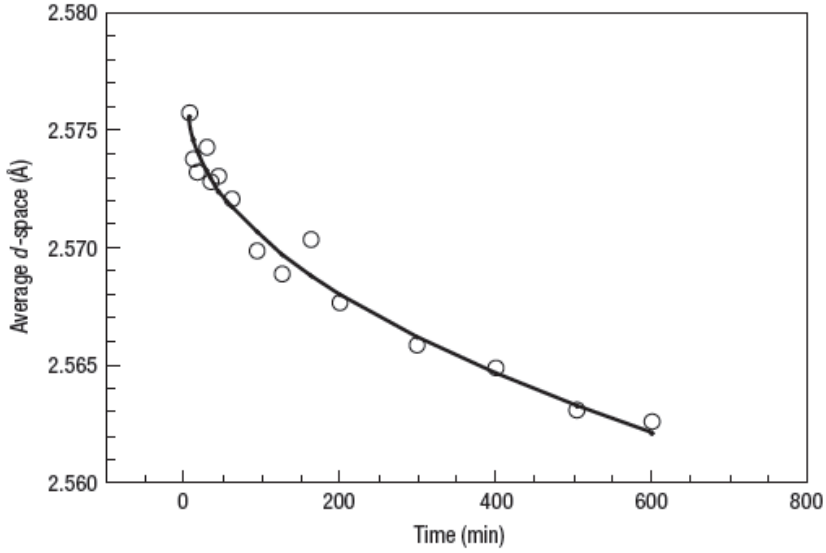

Figure 1.24: Measured change with oxidation time at 1100°C of average lattice spacing in the oxide scale, as the composition of the growing oxide evolves from hematite $(Fe,Cr,Al)_2O_3$ to corundum α-Al_2O_3.

Compositional changes in the metallic alloy or the oxide scale, accompanied or not by phase transformations, are another likely source of stress induced by the oxidation process and species diffusion at high temperature. Oxygen incorporation in the metallic substrate, either in solid solution or as internal oxide particles, induces a specific volume expansion and is thus a significant source of stress for certain metals, such as niobium, tantalum or zirconium (Stott and Atkinson 1994; Huntz 1995). This phenomenon is limited by the solubility of oxygen into the metallic alloy, which is negligible for most metallic compounds (with the notable exception of Ti_3Al and Ni_3Al, phases which might form on NiAl bond coats sometimes used in TBC) (Birks, Meier et al. 2006). Selective oxidation, i.e. the formation of a specific oxide on a metallic alloy (for instance chromia on Fe-Cr or alumina on Ni-Al) might also engender stresses if the two metallic species do

not present matching diffusion kinetics. The resulting stresses might be either tensile or compressive (Suo, Kubair et al. 2003).

More generally, composition gradients induced by the oxidation process have been proven to possibly engender significant stresses or strains, especially in metallic alloys (Tolpygo and Clarke 2000). An important phenomenon that may weaken the oxide scale, the metal substrate or their interface is metal depletion, due to its consumption in oxide scale growth and insufficient local diffusive replacement. The vacancies generated may condense and form pores or voids, more particularly along grain boundaries and at the metal/oxide interface (Howes 1967). A striking example of void formation is shown in Figure 1.23 (Suo, Kubair et al. 2003). Oxide scales might also be affected by composition gradients if they exhibit large deviations from stoichiometry, as it is the case for iron and zirconium oxides (Birks, Meier et al. 2006). In such oxides, a significant point defect gradient might establish through the growing layer, inducing local variations in the lattice parameter. This phenomenon is nevertheless unlikely in alumina and chromia which present a very high stoichiometry, with maximum deviations below 0.1% (notice that a high stoichiometry is equivalent to a very low density of point defects) (Birks, Meier et al. 2006). However, the development of a mixed scale constituted of several oxide phases might lead to the rise of a compositional strain gradient.

Finally, another phenomenon generating stress at the initial stage of oxidation is worth mentioning: depending on the substrate alloy and the experimental conditions (atmosphere, temperature), transient oxide phases might develop at first, and then further evolve to form the most stable oxide. This process induces a specific volume change within the existing oxide phase, and has been proven to engender significant stresses at

short terms, which might be tensile (Howes and Richardson 1969; Veal, Paulikas et al. 2006). An example of measured variation in average lattice spacing in the oxide scale with oxidation time at short term is provided in Figure 1.24 (Veal, Paulikas et al. 2006).

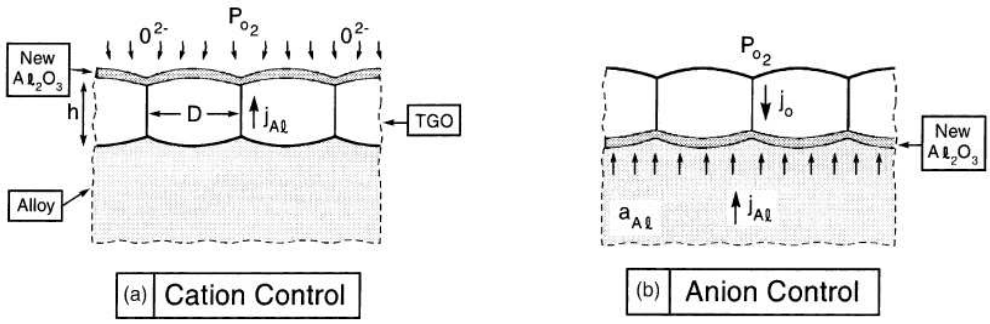

Figure 1.25: Principal oxide growth location depending on the controlling ionic diffusion (Kang, Hutchinson et al. 2003).

The historically most renowned growth stress generation mechanism is directly related to the alloy oxidation process. It has been proposed by Pilling and Bedworth (Pilling and Bedworth 1923), and is based on the idea that if the oxide scale at the metal/oxide interface grows by consumption of the metallic substrate, the change of specific volume between the consumed phase and the created one would engender a volume eigenstrain (inelastic strain). The parameter associated with this phenomenon is the Pilling-Bedworth ratio (PBR), measuring the ratio of the transformed phase molar volume to that of the consumed one, following the chemical reaction stoichiometric equation:

$$PBR = \frac{\Omega_{ox}}{\Omega_{met}} \tag{1.19}$$

Ω_{ox} and Ω_{met} then refers to the specific volume of the oxide and the metal phases, respectively, for a same number of moles of metal. The accommodation of this volume strain in a constrained space would then result in the development of stresses.

The success of this theory relies on its capacity to qualitatively predict the sign of growth stresses in the oxide scale. In most oxidation cases the Pilling-Bedworth ratio is greater than one, corresponding to a volume expansion, and consequently compressive stresses are expected in the scale. It is the case for alumina and chromia, which present respective PBR of 1.28 and 2.07 (Evans 1995). Conversely, a ratio lower than unity predicts a tensile state, which can explain why concerned metals such as potassium, magnesium and sodium can generally not maintain a protective oxide scale (Birks, Meier et al. 2006) (tension engenders porosity and cracks development).

Despite this qualitative experimental agreement, it is now largely recognized that this theory is incomplete for growth stress prediction. Detractors of this model argue that this phenomenon would result in unrealistic stress levels, of the order of several tens of gigapascals considering typical Pilling-Bedworth ratio values between 1.2 and 2 (Clarke 2002; Limarga, Wilkinson et al. 2004). This raises the point that simultaneous plastic accommodation processes would necessarily be involved. The energy released by the oxidation reaction being much higher than the work required for plastic accommodation (Harris and Crossland 1979), the combination of the two processes is relevant. In the case of a high creep rate, it is even possible that the volume strain is spontaneously accommodated, leading to a global outward displacement of the existing scale without significant stress generation. However, this is unlikely for refractory oxides as considered here (Evans 1995).

Another sometimes opposed argument is that this mechanism would not lead to an increasing stress level with oxidation time and therefore could not explain isothermal mechanical failures. This argument is easily disproved by the fracture energy approach, in which the total elastic energy stored within the oxide scale is considered for the failure criterion (Evans 1948; Evans and Taylor 1997; Schutze 2005), see equation (1.18). Accordingly, it is not necessary for a growing oxide scale that the stress level increases in order to lead to fracture or spallation.

A strong limitation in the theory is the fact that the phenomenon would engender stresses only if the oxide scale grows inward over the metallic substrate, and therefore by anionic (oxygen) diffusion. Oxide scale growth at the outer free interface is usually considered to occur without significant stress generation or deformation, due to the direct possibility of accommodation for the new oxide formed on top of the existing layer. A schematic of the two growth mode is provided in Figure 1.25 (Kang, Hutchinson et al. 2003). Inward growth is the preferred development direction for alumina, which exhibits a higher oxygen diffusivity than does metal (Kang, Hutchinson et al. 2003). In contrast, regular chromia scales have been widely reported to develop outwards as a consequence of a metal diffusion control (Kofstad and Bredesen 1992). However, dopants and/or coatings are now systematically added to the metallic alloys to reduce the oxide scale growth rate (Yang 2008). In this situation, the chromium outward diffusion is decreased and the chromia scales have been proved to develop by significant if not dominant inward oxidation (Hou and Stringer 1995). Therefore the Pilling-Bedworth mechanism might be relevant.

Overall, it is likely that the oxidation process at the oxide-metal interface locally induces stresses, since phase dissolution and formation occur probably accompanied by local volume variations. The resulting overall volume strain should be related to the Pilling-Bedworth ratio but is likely to quantitatively differ, due to species interdiffusion, creation and annihilation of vacancies and other possible accommodation processes on both side of the phase boundary. A volumetric growth strain associated with oxidation at the inner oxide/metal interface has been experimentally measured to 2.2 for an alumina scale on a FeCrAlY alloy (Kang, Hutchinson et al. 2003).

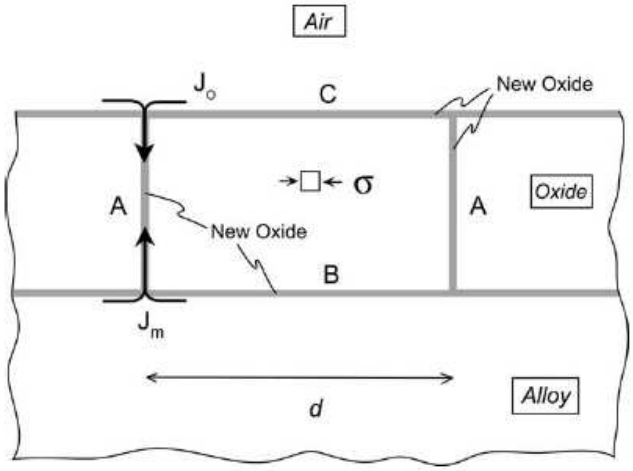

Figure 1.26: Likely locations of new oxide formation resulting from inward diffusion of oxygen and outward diffusion of metal. Oxide formation along grain boundaries lying perpendicular to the interface would induce the in-plane compression of the oxide scale.

Over the last decade, a last mechanism has gained considerable interest. Initially described by Rhines and Wolf (Rhines and Wolf 1970), it is based on the idea that new oxide formed along grain boundaries lying perpendicular to the interface would generate an in-plane expansion strain. Since the oxide scale is laterally constrained (by the

substrate and any coating), this in turn generates a compressive in-plane stress, as mainly measured during oxidation experiments. An illustration of the mechanism is provided in Figure 1.26 (Clarke 2003). This phenomenon requires concurrent inward diffusion of oxygen and outward diffusion of metal ions, a situation which has been evidenced for doped or coated chromia scales (Tsai, Huntz et al. 1996) and as well as for alumina layers (Nychka and Clarke 2005).

As briefly demonstrated by Clarke, a very limited strain (~0.1%) corresponding to the insertion of an extra plane of atoms along vertical grain boundaries with an average in-plane grain size of half a micron, would result in a compressive stress of about 0.5 GPa if the scale is fully constrained by the underlying substrate (Clarke 2003). Thus minor oxidation, negligible to the oxide scale growth and requiring only very weak species fluxes, which always exist, could lead to the stress levels that are experimentally measured. This proves the likely significance and relevance of internal oxidation along grain boundaries as a growth stress origin, even in the case of a predominant growth direction. This last fact constitutes the main reason for the acknowledgement of this mechanism, since it has been observed that growth stresses can develop even in cases of exclusive external growth (Huntz 1995). It is worth mentioning that this phenomenon is fully analogous to grain coarsening (in-plane growth), sometimes also cited as a process leading to growth stresses.

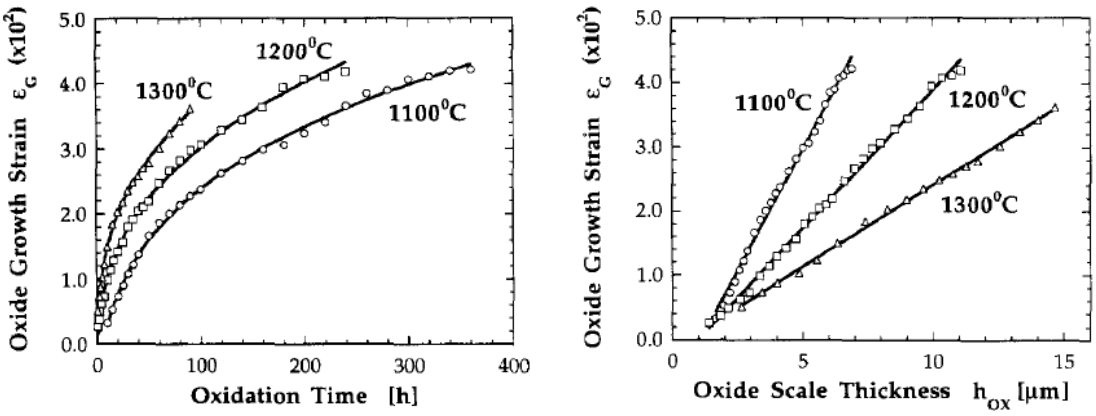

Figure 1.27: Unconstrained in-plane growth strain development in the oxide scale at different temperatures, versus oxidation time and oxide scale thickness. The data are indirectly extracted from experimental measurements.

Just like the Pilling-Bedworth theory, the Rhines and Wolf concept provides a meaningful mechanism for the development of in-plane compressive growth stresses, but direct experimental evidence of oxide formation within grain boundaries of an oxide scale is missing. Even at the macroscopic level, concurrent stress relaxation processes render difficult the measurement and interpretation of a lateral growth strain. Through analysis of the evolution with time of the macroscopic elongational strain and the residual stress in the oxide scale during the oxidation of metal sheets, lateral growth strains of up to 4% have been identified in an alumina scale on a FeCrAlY alloy oxidized in the range of 1100-1300°C (Tolpygo, Dryden et al. 1998). In this study, comparison of the experimental data for different metal sheet thicknesses is used to differentiate the growth strain from the large creep accommodation strain. The identified growth strain development is presented in Figure 1.27 (Tolpygo, Dryden et al. 1998). It is found to be proportional to the oxide scale growth, and thus to be most probably directly related to diffusion processes through the oxide scale, as supported by the Rhines-Wolf theory.

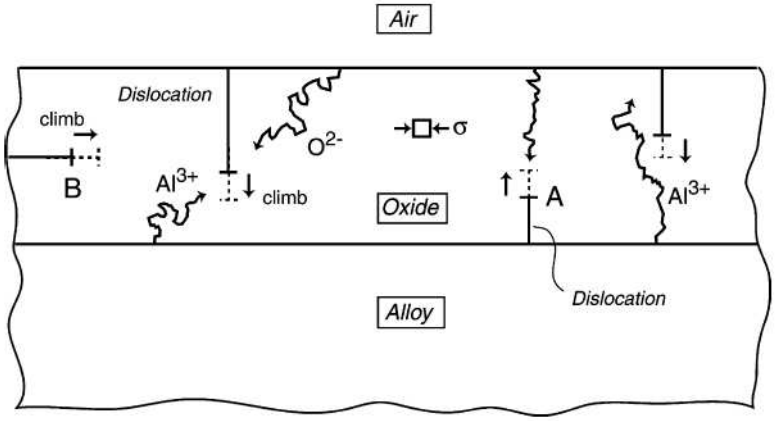

Figure 1.28: Schematic diagram of Clarke's mechanism. Edge dislocation climb results from the local trapping of counter-diffusing metal and oxygen ions. An in-plane growth strain is produced when the dislocation present a Burgers vector parallel to the interface.

While the Rhines and Wolf model constitutes a powerful concept, no defect mechanism and reaction sites have been proposed initially. From the point defect theory, Atkinson analyzed the possibility of oxide formation or consumption depending on the diffusing defects for oxygen and metal through the oxide scale (Atkinson 1982). However, little is known on the precise diffusing defects in alumina and chromia scales thus preventing any reliable conclusion. From the experimental observations described above, in which the growth strain is found to be proportional to the oxide scale thickness, Clarke proposed a mechanism based on geometric microstructural considerations. Here the lateral growth strain would result from the climb of edge dislocations having a Burgers vector parallel to the oxide/alloy interface, in response to trapping of counter-diffusing cations and anions at the core of the dislocations (Clarke 2003). A schematic of the mechanism considered is provided in Figure 1.28 (Clarke 2003). While it would be extremely difficult to experimentally assess this process, it provides a meaningful

phenomenological model which has gained considerable recognition (Balint and Hutchinson 2005; Jedlinski 2005; Kitamura, Nishiyama et al. 2005; Zhu, Fleck et al. 2005; Busso and Qian 2006; Karadge, Zhao et al. 2006; Panicaud, Grosseau-Poussard et al. 2006; Hou, Paulikas et al. 2007; Limarga and Wilkinson 2007).

1.6 Focus of the study and methodology

As can be inferred from the previous sections, the optimization of the composition and preparation of the material systems in view of increasing the devices' lifetime is a challenging work. On top of the mechanical evolution, additional requirements may render the task even more complex. For instance, loss of electrical conductivity and chromium volatilization at the free surface are major issues degrading SOFC interconnect performances (Fergus 2005). Therefore, there is a pressing need for models and simulation tools allowing for better understanding and description of the main processes taking place during high temperature oxidation and their relative contributions to system failure. Such advances are required to identify the key properties of metallic alloys and oxide scales, along with their optimal values, allowing professionals as a result to design better performing structures and material compositions. In a second approach, such models can also help predict the oxide/metal system lifetime as well as the failure mode depending on key characteristics (see for instance (Busso, Wright et al. 2007)).

In this thesis, modeling efforts have focused on the couplings between stress development and oxide scale growth during high-temperature oxidation, in view of investigating the possibility of stress-induced non-uniform morphological developments of the oxide layer. The focus on non-uniform oxide growth is motivated by the fact that

most oxide scales grown in the studied systems at high temperature exhibit an irregular morphology (characterized here by a varying thickness). This situation has been identified by many authors as highly detrimental to the material system mechanical lifetime (Galerie, Toscan et al. 2004; Evans, Clarke et al. 2008). Despite this strong conclusion, to our knowledge no study has been performed on the processes and mechanisms possibly leading to such a phenomenon. The detrimental contribution of oxide scale non-uniformity is discussed in the next section, along with the different situations that might lead to such morphology. The review points out the likely substantial role that growth stresses might play by locally affecting the oxidation process. Eventually, the general methodology applied in this study is presented.

1.6.1 Non-uniform oxide scale development

The development of an oxide scale of non-uniform thickness is critical to the mechanical lifetime of metal/oxide systems for two main reasons. In our review of mechanical failure associated with high temperature oxidation of thermal barrier coatings and SOFC interconnects, we point out the primary importance of the oxide scale interfaces. While strength is of major concern, the geometry has been identified as a key characteristics for the mechanical failure mechanisms (upon thermal cycling (Evans, Mumm et al. 2001) or during isothermal oxidation (Karlsson, Hutchinson et al. 2002; Panat, Hsia et al. 2005; Busso, Wright et al. 2007)). Indeed, the oxide layer interfaces are a typical location of mechanical failure (Padture, Gell et al. 2002; Galerie, Toscan et al. 2004). The geometry has been shown to play a major role in crack development upon cooling due to the raise of induced tensile tractions (see Figure 1.18). Furthermore, a non-

uniform thickness inevitably results in a varying rigidity of the oxide layer, likely to locally induce enlarged plastic deformations at the weakest sections under the effect of an in-plane compressive stress. Such a phenomenon could lead to an accelerated fracture or spallation of the oxide scale, at oxidation temperature if growth stresses are important, or upon cooling. Moreover, even in the case where plastic deformation would be quite limited during isothermal oxidation and cooling, it could become significant by a ratcheting mechanism associated with thermal cycling. Therefore any local variations of the oxide scale growth kinetics, inducing morphological developments and a non-uniformity of the oxide scale thickness, might be very detrimental to the system mechanical lifetime.

Inhomogeneities in the local chemical compositions and microstructures of the different materials are likely to engender locally varying oxidation kinetics.

As stated earlier, the oxide growth at high temperature in the cases studied is essentially controlled by oxygen and metal diffusion through the oxide scale, with a significant contribution of the grain boundaries as fast diffusion paths. Therefore higher oxide growth rates could be expected in the vicinity of grain boundaries, resulting in "bumps" with an occurrence related to the microstructure. Such a situation is presented in Figure 1.29 (Evans, Clarke et al. 2008). However, such dramatic variations in oxide scale thickness are not typical and significant non-uniformities related to the oxide microstructure have not been reported for the studied material systems. This can be due to the thermally grown oxide scales exhibiting a much finer microstructure. However, this could also be explained by the fact that the interface (or surface) itself constitutes a

fast diffusion path. It might then allow for the homogenization of the incoming species flux under the effect of a surface minimization driving force.

Inhomogeneities in the chemical composition of the substrate alloy might also prompt varying oxidation kinetics, by inducing the local development of different oxide phases. An example is the phenomenon referred to as secondary oxidation. In this case, the depletion with time of the metal species forming the protective oxide (Cr or Al) in the vicinity of the oxide/metal interface eventually prevents the selective oxidation from taking place. Therefore a secondary oxide phase develops, which is less protective than the targeted one, i.e. exhibits higher oxygen and possibly metal diffusivities. Typically an iron oxide will develop during the secondary oxidation of a high-temperature oxidation-resistant Fe-Cr alloy. This phenomenon is likely to appear non-uniformly along the oxide scale, thus engendering inhomogeneities in the through-scale diffusivity and consequently in the local oxidation kinetics. However, metallic alloy compositions are designed to include a high-enough Cr or Al content to prevent the occurrence of such a detrimental process (Yang, Weil et al. 2003).

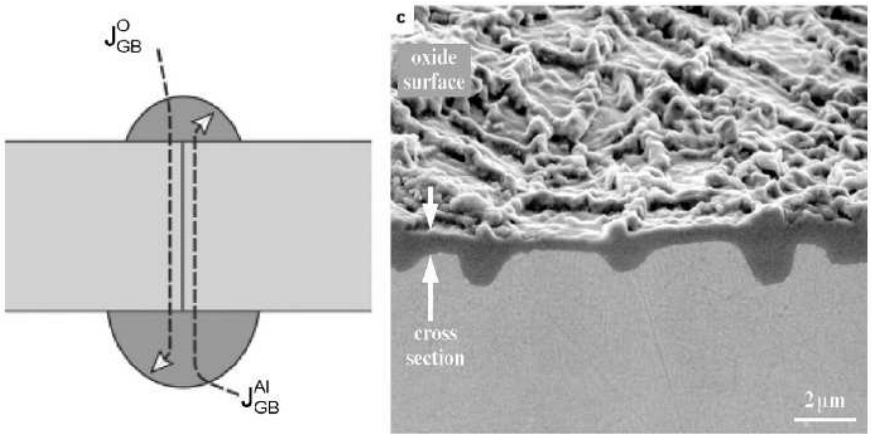

Figure 1.29: Illustration of oxide formation near oxide scale grain boundaries. The micrograph presents the second growth of an alumina scale during re-oxidation after smooth polishing of the oxide layer formed in a first oxidation step.

As seen previously, the oxide scale growth can directly engender significant stresses at high temperature. These stresses are likely to in turn affect the oxide scale development, through large deformations induced by a diffusion creep, or through an influence on the oxidation kinetics at the interfaces (Evans 1995). If the effect is uniform along the scale, this will only modify the global scale growth (and still probably its lifetime). In a worse scenario in which the geometry or heterogeneities in the mechanical behavior or stress generation processes lead to a varying stress field along the oxide scale, a stress influence on local oxide scale growth could result in the development of interfacial morphologies and an oxide scale of non-uniform thickness. These two characteristics have been identified as being very detrimental to the system's reliability upon cooling and thermal cycling (Evans, Clarke et al. 2008). Few direct assessments of stress effects on oxide scale growth kinetics have been reported (Calvarin-Amiri, Molins et al. 2000; Gosmain, Valot et al. 2001). Nevertheless, stress development is thought to be responsible for the anomalous kinetics (non-parabolic) observed during oxidation of zirconium alloys (Evans 1995; Favergeon, Montesin et al. 2005), or nitridation of TiAl (Limarga and Wilkinson 2007).

1.6.2 Methodology

Growth stresses play a key role in most mechanical failure mechanisms. Their generation is directly related to the oxide scale growth, and they may in turn affect the oxide scale growth kinetics. A full coupling exists between the two processes whose extent, influences and consequences need to be investigated. The build up of a comprehensive, specially designed model of stress-affected oxide scale growth and the

development of an adapted simulation tool will contribute to this task. We therefore focus our innovative modeling and simulation efforts on this issue. The research project divides into the following principal tasks:

i. Develop a local formulation of stress-affected oxide scale growth adapted to high temperature oxidation of chromia and alumina forming alloys.

ii. Complete the local formulation with an adequate macroscopic framework describing species diffusion, growth strain development and materials mechanical response.

iii. Develop a numerical framework for implementation of the model allowing for realistic simulations.

iv. Investigate two practical cases concerning a solid oxide fuel cell interconnect and a thermal barrier coating:

− Analyze the mechanism of stress-induced morphological development: investigate the main processes, identify the key physical properties and their respective influence.

− Study the influence of the morphological development on mechanical failure: investigate the effect on identified critical stresses for failure mechanisms, during isothermal oxidation and upon cooling to room temperature.

− Provide optimization tracks for the design of metallic alloy compositions and preparations which should allow for a longer mechanical lifetime of the studied material systems.

A schematic of the research project is provided in Figure 1.30.

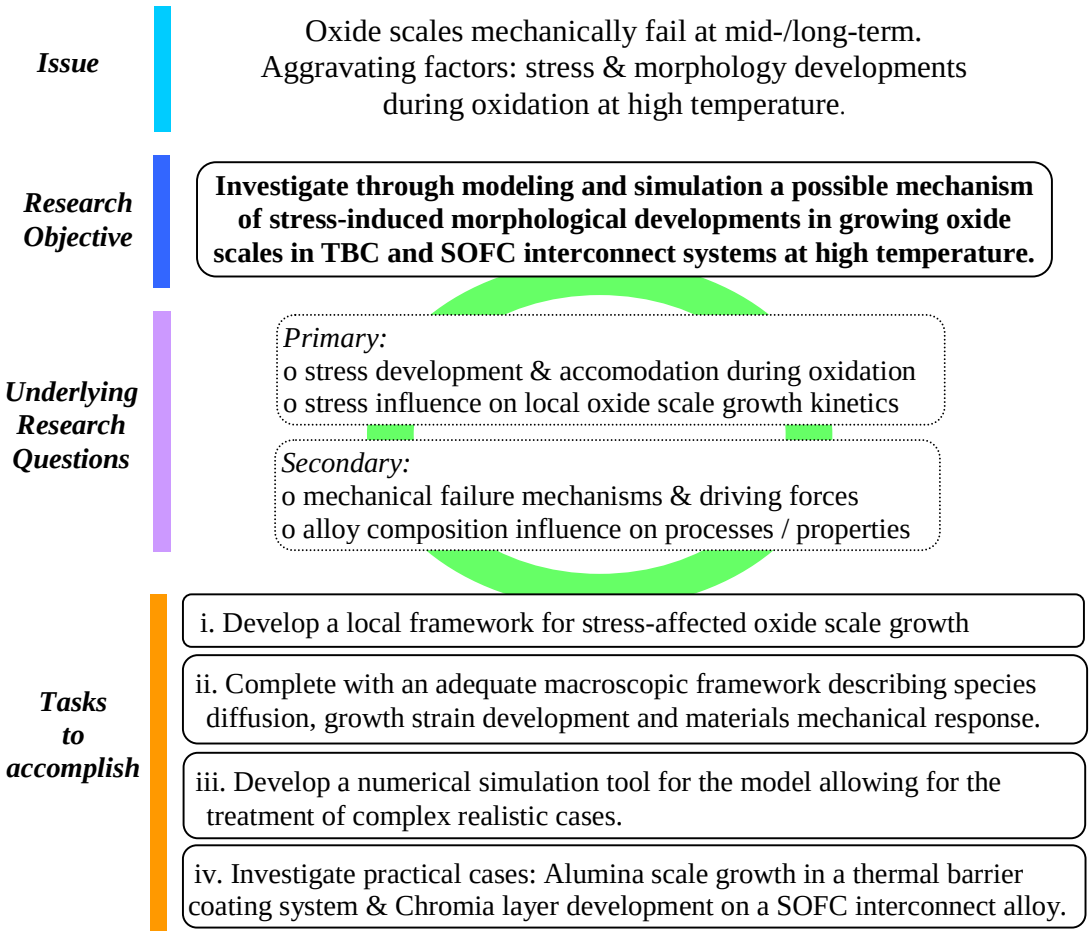

Figure 1.30: schematic of the research project.

1.7 References

Atkinson, A. (1982). "Conditions for the formation of new oxide within oxide films growing on metals." Corrosion Science **22**: 347.

Atkinson, A. (1985). "Transport processes during the growth of oxide films at elevated temperature." Reviews of Modern Physics **57**(2): 437.

Balint, D. S. and J. W. Hutchinson (2005). "An analytical model of rumpling in thermal barrier coatings." Journal of the Mechanics and Physics of Solids **53**(4): 949-973.

Belogolovsky, I., P. Y. Hou, C. P. Jacobson and S. J. Visco (2008). "Chromia scale adhesion on 430 stainless steel: Effect of different surface treatments." Journal of Power Sources **182**(1): 259-264.

Birks, N., G. H. Meier and F. S. Pettit (2006). Introduction to the high-temperature oxidation of metals. New York, Cambridge University Press.

Birnie, J., C. Craggs, D. J. Gardiner and P. R. Graves (1992). "Ex situ and in situ determination of stress distributions in chromium oxide films by raman microscopy." Corrosion Science **33**(1): 1-12.

Busso, E. P. and Z. Q. Qian (2006). "A mechanistic study of microcracking in transversely isotropic ceramic-metal systems." Acta Materialia **54**: 3325-338.

Busso, E. P., L. Wright, H. E. Evans, L. N. McCartney, S. R. J. Saunders, S. Osgerby and J. Nunn (2007). "A physics-based life prediction methodology for thermal barrier coating systems." Acta Materialia **55**(5): 1491-1503.

Calvarin-Amiri, G., R. Molins and A. M. Huntz (2000). "Effect of the application of a mechanical load on the oxide-layer microstructure and on the oxidation mechanism of ni-20cr foils." Oxidation of Metals **53**(3-4): 399-426.

Caplan, D. and G. I. Sproule (1975). "Effect of oxide grain structure on the high temperature oxidation of cr." Oxidation Met. **9**: 459-471.

Christensen, R. J., D. M. Lipkin and D. R. Clarke (1996). "Nondestructive evaluation of the oxidation stresses through thermal barrier coatings using cr^{3+} piezospectroscopy." Applied Physics Letter **69**(24): 3754-3756.

Clarke, D. R. (2002). "Stress generation during high-temperature oxidation of metallic alloys." Current Opinion in Solid State and Materials Science **6**(3): 237.

Clarke, D. R. (2003). "The lateral growth strain accompanying the formation of a thermally grown oxide." Acta Materialia **51**: 1393-1407.

Dieckmann, R. (1998). "Point defects and transport in non-stoechiometric oxides: Solved and unsolved problems." J. Phys. Chem. Solids **59**(4): 507-525.

Evans, A. G., D. R. Clarke and C. G. Levi (2008). "The influence of oxides on the performance of advanced gas turbines." Journal of the European Ceramic Society **28**(7): 1405-1419.

Evans, A. G., D. R. Mumm, J. W. Hutchinson, G. H. Meier and F. S. Pettit (2001). "Mechanisms controlling the durability of thermal barrier coatings." Progress in Materials Science **46**(5): 505-553.

Evans, H. E. (1995). "Stress effects in high-temperature oxidation of metals." International Materials Reviews **40**(1): 1-40.

Evans, H. E. and M. P. Taylor (1997). "Creep relaxation and the spallation of oxide layers." Surface & Coatings Technology **94-5**(1-3): 27-33.

Evans, U. R. (1948). An introduction to metallic corrosion. London, Edward Arnold.

Favergeon, J., T. Montesin and G. Bertrand (2005). "Mechano-chemical aspects of high temperature oxidation: A mesoscopic model applied to zirconium alloys." Oxidation of Metals **64**(3-4): 253-279.

Fergus, J. W. (2005). "Metallic interconnects for solid oxide fuel cells." Materials Science and Engineering **A397**: 271-283.

Galerie, A., F. Toscan, M. Dupeux, J. Mougin, G. Lucazeau, C. Valot, A. M. Huntz and L. Antoni (2004). "Stress and adhesion of chromia-rich scales on ferritic stainless steels in relation with spallation." Materials Research **7**(1): 81-88.

Gosmain, L., C. Valot, D. Ciosmak and O. Sicardy (2001). "Study of stress effects in the oxidation of zircaloy-4." Solid State Ionics **141**: 633-640.

Harris, J. E. and I. G. Crossland (1979). "Mechanical effects of corrosion - old problem in a new setting." Endeavour **3**(1): 15-26.

He, M. Y., A. G. Evans and J. W. Hutchinson (2000). "The ratcheting of compressed thermally grown thin films on ductile substrates." Acta Materialia **48**(10): 2593-2601.

Heuer, A. H. (2008). "Oxygen and aluminum diffusion in alpha-al2o3: How much do we really understand?" Journal of the European Ceramic Society **28**(7): 1495-1507.

Holt, A. and P. Kofstad (1994). "Electrical-conductivity and defect structure of cr2o3 .2. Reduced temperatures (less-than-similar-to-1000-degrees-c)." Solid State Ionics **69**(2): 137-143.

Hou, P. Y., A. P. Paulikas, B. W. Veal and J. L. Smialek (2007). "Thermally grown al2o3 on a h-2-annealed fe3al alloy: Stress evolution and film adhesion." Acta Materialia **55**(16): 5601-5613.

Hou, P. Y. and J. Stringer (1995). "The effect of reactive element additions on the selective oxidation, growth and adhesion of chromia scales." Materials Science and Engineering a-Structural Materials Properties Microstructure and Processing **A202**(1-2): 1-10.

Howes, V. R. (1967). "Observations of a metal-oxide interface." Nature **216**: 362.

Howes, V. R. and C. N. Richardson (1969). "Initial stresses developed during high temperature oxidation of fe-cr alloys." Corrosion Science **9**(6): 385-&.

Huntz, A. M. (1995). "Diffusion dans les couches d'oxyde en cours de croissance." Journal de Physique III **5**: 1729-1757.

Huntz, A. M. (1995). "Stresses in nio, cr_2o_3 and al_2o_3, oxide scales." Materials Science and Engineering **A201**: 211-228.

Huntz, A. M., S. Daghigh, A. Piant and J. L. Lebrun (1998). "Evidence of stress relaxation in thermally grown oxide layers - experiments and modelling." Materials Science and Engineering **A248**: 44-55.

Jedlinski, J. (2005). Defect-diffusion-stress relationships in modeling the oxidation and degradation processes of alumina formers: A brief survey. Diffusion in materials: Dimat 2004, pt 1and 2. **237-240:** 911-921.

Kang, K. J., J. W. Hutchinson and A. G. Evans (2003). "Measurement of the strains induced upon thermal oxidation of an alumina-forming alloy." Acta Materialia **51**(5): 1283-1291.

Karadge, M., X. Zhao, M. Preuss and P. Xiao (2006). "Microtexture of the thermally grown alumina in commercial thermal barrier coatings." Scripta Materialia **54**(4): 639-644.

Karlsson, A. M., J. W. Hutchinson and A. G. Evans (2002). "A fundamental model of cyclic instabilities in thermal barrier systems." Journal of the Mechanics and Physics of Solids **50**(8): 1565-1589.

Kemdehoundja, M., J. L. Grosseau-Poussard and J. F. Dinhut (2008). "Substrate grain boundary effect on residual stress distribution at micrometer scale in chromia oxide thin films." Applied Physics Letters **92**(24).

Kemdehoundja, M., J. L. Grosseau-Poussard, J. F. Dinhut and B. Panicaud (2007). "Growth stresses in alpha-cr2o3 thermal oxide films determined by in situ high temperature raman spectroscopy." Journal of Applied Physics **102**(9).

Kitamura, K., Y. Nishiyama, N. Otsuka and T. Kudo (2005). "In situ growth-stress measurement of cr_2o_3 scale formed on stainless steels by raman spectroscopy." High-Temperature Oxidation and Corrosion **522-523**: 489-495.

Kofstad, P. and R. Bredesen (1992). "High temperature corrosion in sofc environments." Solid State Ionics **52**: 69-75.

Kurokawa, H., K. Kawamura and T. Maruyama (2004). "Oxidation behavior of fe-16cr alloy interconnect for sofc under hydrogen potential gradient." Solid State Ionics **168**: 13-21.

Limarga, A. M. and D. S. Wilkinson (2007). "Creep-driven nitride scale growth in gamma-tial." Acta Materialia **55**(1): 251-260.

Limarga, A. M. and D. S. Wilkinson (2007). "Modeling the interaction between creep deformation and scale growth process." Acta Materialia **55**(1): 189-201.

Limarga, A. M., D. S. Wilkinson and G. C. Weatherly (2004). "Modeling of oxidation-induced growth stresses." Scripta Materialia **50**: 1475-1479.

Lipkin, D. M. and D. R. Clarke (1996). "Measurement of the stress in oxide scales formed by oxidation of alumina-forming alloys." Oxidation of Metals **45**(3-4): 267-280.

Lipkin, D. M., D. R. Clarke, M. Hollatz, M. Bobeth and W. Pompe (1997). "Stress development in alumina scales formed upon oxidation of (111)nial single crystals." Corrosion Science **39**(2): 231-242.

Liu, H., M. M. Stack and S. B. Lyon (1998). "Reactive element effects on the ionic transport processes in cr_2o_3 scales." Solid State Ionics **109**: 247-257.

Mikkelsen, L. and S. Linderoth (2003). "High temperature oxidation of fe-cr alloy in o_2-h_2-h_2o atmospheres; microstructure and kinetics." Materials Science and Engineering **A361**: 198-212.

Mougin, J., A. Galerie, M. Dupeux, N. Rosman, G. Lucazeau, A. M. Huntz and L. Antoni (2002). "In-situ determination of growth and thermal stresses in chromia scales formed on a ferritic stainless steel." Materials and Corrosion **53**: 486-490.

Mougin, J., G. Lucazeau, A. Galerie and M. Dupeux (2001). "Influence of cooling rate and initial surface roughness on the residual stresses in chromia scales thermally grown on pure chromium." Materials Science and Engineering a-Structural Materials Properties Microstructure and Processing **308**(1-2): 118-123.

Mougin, J., N. Rosman, G. Lucazeau and A. Galerie (2001). "In-situ raman monitoring of chromium oxide scale growth for stress determination." J. Raman Spectrosc. **32**: 739-744.

Nychka, J. A. and D. R. Clarke (2005). "Quantification of aluminum outward diffusion during oxidation of fecral alloys." Oxidation of Metals **63**(5-6).

Padture, N. P., M. Gell and E. H. Jordan (2002). "Materials science - thermal barrier coatings for gas-turbine engine applications." Science **296**(5566): 280-284.

Panat, R., K. J. Hsia and D. G. Cahill (2005). "Evolution of surface waviness in thin films via volume and surface diffusion." Journal of Applied Physics **97**(1).

Panicaud, B., J. L. Grosseau-Poussard and J. F. Dinhut (2006). "On the growth strain origin and stress evolution prediction during oxidation of metals." Applied Surface Science **252**(16): 5700-5713.

Pieraggi, B. and R. A. Rapp (1988). "Stress generation and vacancy annihilation during scale growth limited by cation-vacancy diffusion." Acta Metallurgica **36**(5): 1281.

Pilling, N. B. and R. E. Bedworth (1923). "The oxidation of metals at high temperatures." Journal of the Institute of Metals **29**: 529-582.

Rhines, F. N. and J. S. Wolf (1970). "The role of oxide microstructure and growth stresses in the high-temperature scaling of nickel." Metal. Trans. **1**: 1701-1710.

Sabioni, A. C. S., A. M. Huntz, F. Silva and F. Jomard (2005). "Diffusion of iron in cr_2o_3: Polycrystals and thin films." Materials Science and Engineering **A392**: 254-261.

Sarioglu, C., M. J. Stiger, J. R. Blachere, R. Janakiraman, E. Schumann, A. Ashary, F. S. Pettit and G. H. Meier (2000). "The adhesion of alumina films to metallic alloys and coatings." Materials and Corrosion-Werkstoffe Und Korrosion **51**(5): 358-372.

Schutze, M. (2005). "Modelling oxide scale fracture." Materials at High Temperatures **22**(1-2): 147-154.

Stefan, J. (1889). "Uber die theorie der eisbildung, insbesondere uber die eisbildung im polarmeere." Sitzungsberichte der Osterreichischen Akademie der Wissenschaften Mathematisch-Naturwissenschaftliche Klasse, Abteilung 2, Mathematik, Astronomie, Physik, Meteorologie und Technik **98**: 965-983.

Stott, F. H. and A. Atkinson (1994). "The modelling of growth stresses during high-temperature oxidation." Materials at High Temperatures **12**(2-3): 195-207.

Suo, Z. (1995). "Wrinkling of the oxide scale on an aluminum-containing alloy at high-temperatures." Journal of the Mechanics and Physics of Solids **43**(6): 829-846.

Suo, Z., D. V. Kubair, A. G. Evans, D. R. Clarke and V. K. Tolpygo (2003). "Stresses induced in alloys by selective oxidation." Acta Materialia **51**: 959-974.

Tolpygo, V. K. and D. R. Clarke (1998). "Wrinkling of a-alumina films grown by thermal oxidation." Acta Mater. **46**: 5163-5167.

Tolpygo, V. K. and D. R. Clarke (2000). "Surface rumpling of a (ni, pt)al bond coat induced by cyclic oxidation." Acta Materialia **48**(13): 3283-3293.

Tolpygo, V. K., J. R. Dryden and D. R. Clarke (1998). "Determination of the growth stress and strain in alpha-al_2o_3 scales during the oxidation of fe–22cr–4.8al–0.3y alloy." Acta Materialia **46**(3): 927-937.

Tsai, S. C., A. M. Huntz and C. Dolin (1996). "Growth mechanism of cr_2o_3 scales: Oxygen and chromium diffusion, oxidation kinetics and effect of yttrium." Materials Science and Engineering **A212**: 6-13.

Veal, B. W., A. P. Paulikas and P. Y. Hou (2006). "Tensile stress and creep in thermally grown oxide." Nature Materials **5**(5): 349-351.

Wagner, C. (1933). Zeitschrift fur Physikalische Chemie **21**: 25-41.

Yang, Z., K. S. Weil, D. M. Paxton and J. W. Stevenson (2003). "Selection and evaluation of heat-resistant alloys for sofc interconnect applications." Journal of the Electrochemical Society **150**(9): A1188-A1201.

Yang, Z. G. (2008). "Recent advances in metallic interconnects for solid oxide fuel cells." International Materials Reviews **53**(1): 39-54.

Zhao, X. and P. Xiao (2007). "Focus effect of photoluminescence piezospectroscopy and its influence on the stress measurement of thermally grown oxide in thermal barrier coatings." Scripta Materialia **57**(8): 683-686.

Zhu, H. X., N. A. Fleck, A. C. F. Cocks and A. G. Evans (2005). "Numerical simulations of crack formation from pegs in thermal barrier systems with nicocraly bond coats." Materials Science and Engineering A-Structural Materials Properties Microstructure and Processing **A404**(1-2): 26-32.

CHAPTER 2

MODEL OF STRESS-AFFECTED OXIDATION

2.1 Introduction

The challenges in phase boundary propagation modeling are extensive, since numerous processes covering highly coupled physical processes are usually involved. Among them are ionic species transport within solids, species segregation, transfer and defect generation/annihilation at the interface, thermodynamic reactions resulting in phase decomposition, precipitation and growth, mechanical strain development and accommodation, stress, cracks and cavity nucleation, heat transfer, absorption and release, just to name a few. These processes operate over a large range of length-scales (from the nanometer to the millimeter); they follow different kinetics and are controlled by specific local and global mechanisms. Thus phase boundary evolution is among the most complex and challenging phenomena to study and model. Hopefully, in most practical cases, a single mechanism dominates the kinetics of interface evolution at the macroscopic level.

As stated previously, the long-term growth of a thick and compact oxide scale is globally described by the species diffusion through the growing layer. The propagation of the phase boundary is then governed by the mass conservation of the chemical reaction limiting species at the interface. The reaction of oxidation can be considered instantaneous at the time scale of the oxide layer development. However, this thermodynamic process plays a major role in the establishment of the local interface composition and consequently in the setting of the global diffusion processes. In this

chapter, the two main approaches to a stress effect on the oxide scale growth are reviewed, and a specific local formulation for stress-affected oxidation kinetics is then presented and derived.

2.2 Models of stress effect on oxide scale growth kinetics

Two main mechanisms have been advanced to describe a stress effect on oxidation kinetics, both affecting species diffusion. This is justified by the fact that the long-term oxide growth kinetics has been identified to be diffusion-controlled, and it has furthermore been shown that the free energy released by the oxidation reaction is such that a strain accommodation work able to suppress the process would require a stress level about two orders of magnitude higher than typical oxide yield or fracture stresses (Evans 1995). Consequently, a stress influence on the chemical reaction rate is excluded.

The first mechanism considered is a stress influence on bulk diffusion. The most renowned model accounts for a stress-induced local variation of the species diffusion potential, according to a model initially developed by Larché and Cahn (Larche and Cahn 1982). It is based on the concept of chemical expansion, a modification of the phase local specific volume induced by the presence of diffusing species. This phenomenon is modeled through the coefficient of chemical expansion, which can be expressed for a species *i* in a binary isotropic and cubic phase φ by (Larche and Cahn 1985):

$$\eta_i^{\varphi} = \frac{1}{3\bar{V}_0^{\varphi}} \frac{\partial \bar{V}^{\varphi}}{\partial c_i} \tag{2.1}$$

where $\bar{V}^{\varphi}$ denotes the molar volume of the phase φ, the subscript 0 refers to the natural

configuration and c_i is the mole fraction of species i. An example of coefficient of chemical expansion data (anisotropic expansion in this case, defined relatively to the mass density of the metal) is provided in Figure 2.1 concerning oxygen in zirconium at 600°C (Favergeon, Montesin et al. 2005).

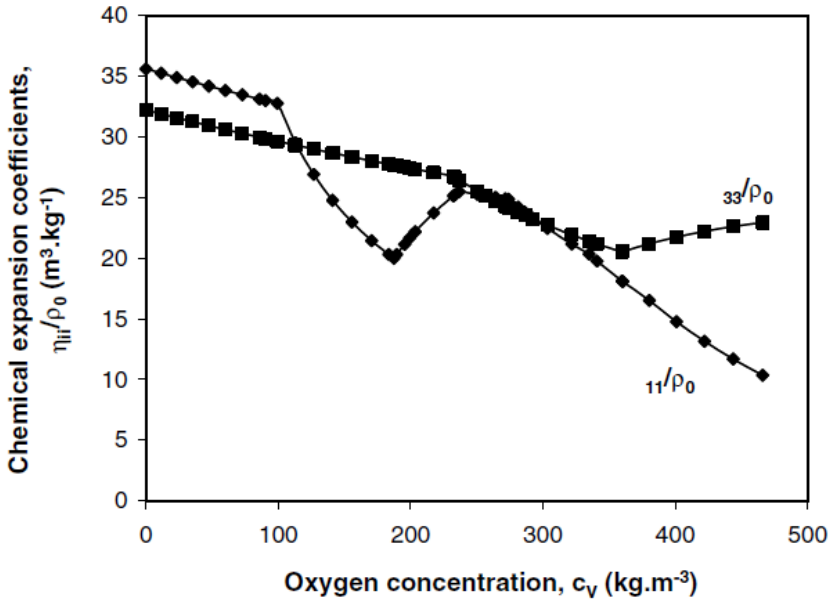

Figure 2.1: Anisotropic chemical expansion coefficients for a axis, η_{11}/ρ_0 and c axis, η_{11}/ρ_0 of the hexagonal Zr-O cell at 600°C. ρ_0 is the mass density of zirconium.

Assuming for simplicity that the elastic stiffness tensor is independent of concentration, the stress effect on the chemical potential is then modeled by:

$$\mu_i^{\varphi}(\sigma,\theta,C_i) = \mu_i^{\varphi}(0,\theta,C_i) - \eta_i^{\varphi}\ \bar{V}_i^{\varphi}\sigma_{kk} \tag{2.2}$$

where $\mu_i^{\varphi}(0,\theta,C_i)$ is the chemical potential of species i in the absence of stress, at temperature θ and molar concentration C_i, σ_{kk} is the trace of the Cauchy stress tensor (it

is then equal to three times the hydrostatic stress), $\bar{V}_i^{\varphi}$ and η_i^{φ} are the molar volume and the chemical expansion coefficient of species *i* in the considered phase φ, respectively. The simple original formulation is provided here to illustrate the modeling, but more accurate expressions introducing the Eshelby stress have since been derived (Wu 2001; Swaminathan, Qu et al. 2007). A practical application on zirconium high temperature oxidation can be found in (Favergeon, Montesin et al. 2005). The stress-affected oxide growth kinetics is shown in Figure 2.2. Note that the chemical expansion effect is accounted for in the metal substrate, which exhibits a high oxygen solubility, and not in the oxide scale.

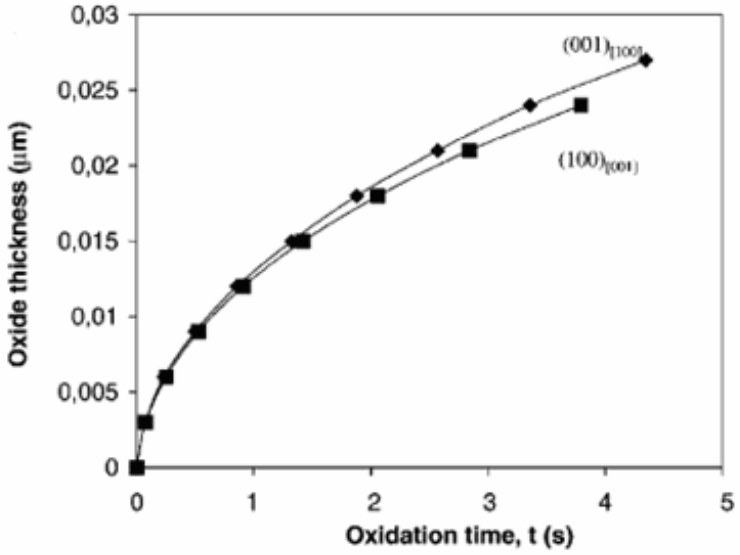

Figure 2.2: ZrO_2 scale growth kinetics on Zr at 600°C obtained from a mechano-chemical model based on a chemical expansion effect on diffusion. The mechanical anisotropy of zirconium induces different stress fields depending on the metal surface orientation, which leads to differences of oxygen uptake in the metal and then results in modified oxide growth kinetics.

Another approach considers a stress influence on the quasi-equilibrium composition at the propagating metal/oxide interface. The principle of a thermodynamic effect on the process kinetics, induced by the stress development accompanying metal oxidation at high temperature, has been reviewed by Evans (Evans 1995). He demonstrated through a simple direct influence on interface vacancy concentration that the accommodation work in response to the metal oxidation-associated volume expansion might significantly alter and even stop the uniform growth of a zirconia film. It assumes that oxygen diffusion through the oxide scale occurs through the motion of vacancies created at the interface by the oxidation reaction. A compressive stress in the oxide scale is assumed to decrease the instantaneous oxidation rate under a thermodynamic effect of the transformation / strain accommodation work. This results in lower instantaneous oxygen consumption and consequently a lower rate of vacancy creation at the interface. This phenomenon leads to a decrease in vacancy concentration at the interface. The stress influence on the vacancy concentration at the metal/oxide interface, C_{V}^{I}, is expressed through:

$$C_{\mathrm{V}}^{I}(\sigma) = C_{\mathrm{V}}^{I}(0)\exp\left(\frac{\sigma_{\mathrm{h}}\Delta\Omega}{k\theta}\right) \tag{2.3}$$

where σ_{h} is the hydrostatic stress, $\Delta\Omega$ is the local volume variation related to the formation of an oxide molecule over the metallic substrate, k is the Boltzmann constant and θ is the temperature. Since the gradient of defect concentration through the scale drives the species diffusion, the incoming flux of oxygen is in turn affected. The through-scale flux of oxygen, opposed to the one of vacancies, is considering a one-dimensional (1D) problem:

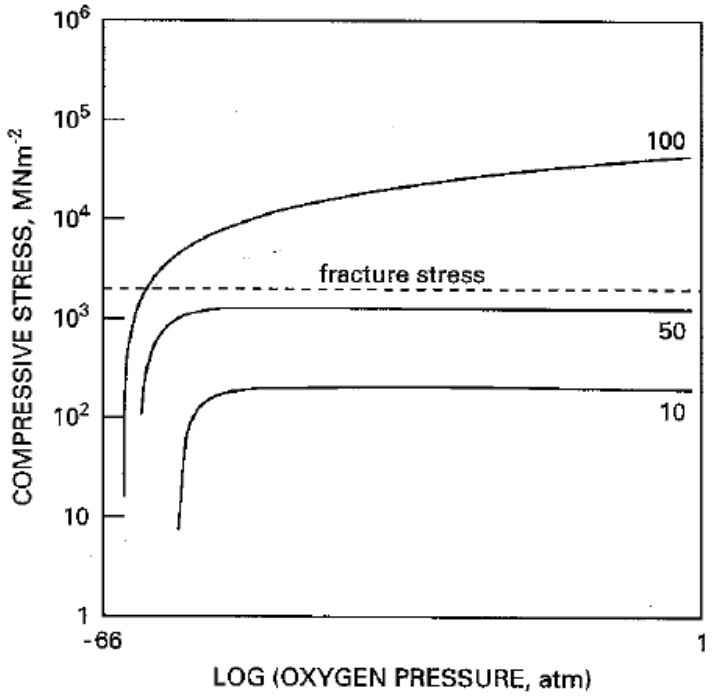

Figure 2.3: Curves of iso-reduction in inner oxidation rate for zirconia at 773K, induced by given compressive stress for a range of oxygen pressures of the oxidizing atmosphere. Numbers on curves give percentage drop in oxidation rate.

$$J_{\mathrm{O}} = -J_{\mathrm{V}} = -\frac{D_{\mathrm{V}}}{\xi}\left\{C_{\mathrm{V}}^{I}(0)\exp\left(\frac{\sigma_{\mathrm{h}}\Delta\Omega}{k\theta}\right) - C_{\mathrm{V}}^{II}\right\} \tag{2.4}$$

where D_{V} stands for the vacancy diffusivity through the oxide scale of thickness ξ, and C_{V}^{II} is the vacancy concentration at the outward interface. As a result, the global oxidation kinetics is slowed down by an in-plane compressive stress within the oxide scale. Assuming that the oxide scale only develops at the inner interface, the growth is even stopped if the hydrostatic stress reaches a critical value:

$$\sigma_{\mathrm{h}} = \frac{k\theta}{\Delta\Omega}\ln\left(\frac{C_{\mathrm{V}}^{II}}{C_{\mathrm{V}}^{I}(0)}\right) \tag{2.5}$$

Introducing the vacancy concentration dependency on oxygen partial pressure at each interface, obtained from the point defect theory, a map of reduction in inner oxidation rate can be formed. It is presented for zirconia (ZrO_2) at 500°C in Figure 2.3. It shows that if the oxidation is only likely to be stopped at very low oxygen pressures, significant reductions in oxide growth kinetics could be induced by this mechanism under reasonable stress levels.

The two models essentially differ by the localization of the stress effect and the way that it impacts the diffusion. In the first mechanism, the influence on diffusion is direct and local within the bulk phase through the stress gradient. Therefore, a chemical expansion phenomenon which would take place within the oxide scale might affect its inward growth, if the contribution of diffusing oxygen is significant, the outward development, if the diffusing ionic metal plays a significant role, or both. The second mechanism is localized at the inner oxidation front, and solely indirectly affects the diffusion through the scale. Therefore it directly impacts the inward oxide growth only. According to both theories, a compressive stress should result in a decrease in the oxidation rate and should therefore lead to a subparabolic oxidation kinetics, a situation commonly reported in our systems of interest (Busso, Lin et al. 2001; Fergus 2005). Note that for alumina scales developing a quite important thickness (above 3 µm), grain coarsening has been identified as the main cause of the oxidation rate decrease, through a reduction in grain boundary volume fraction which affects fast species diffusion (Huntz 1999; Naumenko, Gleeson et al. 2007).

2.3 Chosen approach and general mechanism description

If both mechanisms discussed here are able to justify locally modified kinetics under the effect of stress, the first suffers from the low likelihood of a significant chemical expansion phenomenon in chromia and alumina scales, which present very low composition defect concentrations (Birks, Meier et al. 2006). Furthermore, this mechanism is even more questionable within grain boundaries which exhibit a different microstructure than the bulk with numerous structural defects, and which constitute a significant if not dominant diffusion path in the oxide scales considered. Therefore an approach considering a stress effect on the quasi-equilibrium composition at the metal/oxide interface is chosen. This phenomenon affects the oxide inward development only, and consequently it affects only cases in which a significant inner oxidation occurs.

The growth of an alumina scale in the thermal barrier coating environment occurs mainly at the oxide/metal interface through the direct oxidation of the metallic bond coat (Padture, Gell et al. 2002; Busso and Qian 2006). Most commercial chromia-forming alloys considered for SOFC interconnects now include reactive elements (as yttrium, cerium and lanthanum) or their oxides (Yang 2008). The additions in minor proportions of these elements have demonstrated dramatic effects on oxide scale development, particularly in terms of growth kinetics, morphology and microstructure, as well as on stress generation. These effects can lead to significant improvement of the interconnect lifetime. However, in this situation the chromia scales have been proven to develop by significant if not dominant direct (inward) oxidation of the metallic substrate, unlike regular chromia scales which essentially grow outward at the free surface (Hou and

Stringer 1995). Consequently, the oxidation at the metal/oxide phase boundary becomes more critical.

It is noteworthy that a significant inner growth has also been related to the presence of water vapor in the atmosphere (Essuman, Meier et al. 2007) (which is necessarily the case at least at the anode side of the fuel cell where water is formed). Our review of the oxidation of thermal barrier coatings and SOFC interconnects points to the primary importance of the oxide scale/metal alloy interface morphology in mechanical failure. A non-uniform inner oxidation might play a major role in roughness development at the phase boundary. Furthermore, this interface is likely to be highly stressed due to mismatches in material properties and local volume variations induced by oxidation and diffusion processes. Thus, modeling a mechanism of stress-induced non-uniform inner oxide scale growth is of primary interest.

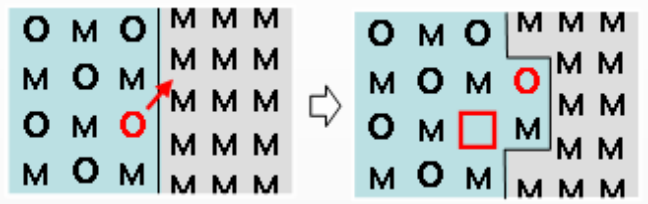

Figure 2.4: Schematic of the vacancy generation mechanism associated with oxidation at the metal/oxide boundary.

The oxygen consumption during the oxidation reaction engenders the creation of vacancies at the oxide boundary, see schematic Figure 2.4. Oxygen ions associate with metal atoms to form oxide molecules at the interface. This process is limited by oxide phase stability. As mentioned previously, the oxide phases considered can only sustain a limited vacancy density, whose maximum bound corresponds to the dissolution

composition (i.e. metal/oxide phase equilibrium composition). The created vacancies diffuse counter to oxygen ions towards the free surface exposed to an oxygen-rich atmosphere. The oxidation chemical reaction being much faster than the species diffusion through the oxide scale, a quasi-equilibrium composition can be assumed at the phase boundary, equal to the metal/oxide phase equilibrium. The inner oxidation process is then limited by the local “availability” of oxygen at the interface, and consequently the oxidation kinetics is controlled by the diffusion through the oxide scale. As a result, coupled quasi-equilibrium concentrations of oxygen and vacancy rapidly establish at the metal/oxide boundary. These are maintained during the oxide phase propagation while quasi-steady state gradients slowly evolve with the oxide scale thickness. The situation is illustrated in Figure 2.5. The mechanism proposed here for a stress influence on the local oxidation kinetics relies on a deviation from the stress-free quasi-equilibrium concentration induced by the mechanical state at the propagating interface. Since the gradient of concentration drives species diffusion, the local incoming flux of oxygen at the phase boundary is in turn affected and eventually the oxidation kinetics (oxide phase propagation) is locally modified.

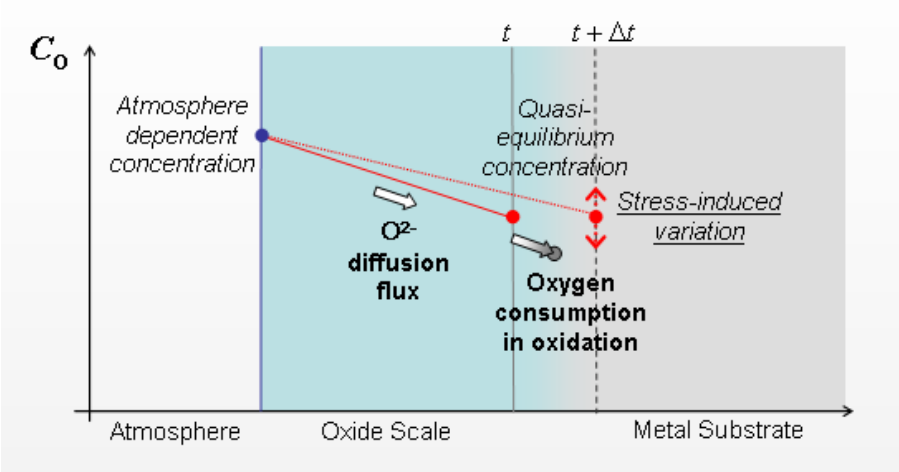

Figure 2.5: Quasi-steady state composition gradient through the oxide scale, oxygen diffusion and consumption in oxidation and oxide phase propagation over the metallic substrate. The stress-induced variation of the interface quasi-equilibrium concentration considered in the model is shown.

It is important to notice that the situation is more complex when problems of two or three space dimensions are considered. In these cases of interest here, the oxide scale geometry might be non uniform, and the composition might vary along the metal/oxide boundary, notably under the effect of a stress profile from the model proposed. Therefore in-plane diffusion gradients will form. The consequence on the previously described mechanism is that the composition corresponding to the metal/oxide phase equilibrium might not be allowed to establish at all times and points of the metal/oxide interface. A local minimum in oxide scale thickness or in interface oxygen concentration will alter the diffusion field by forming higher gradients, and then locally concentrate incoming mass, as illustrated in Figure 2.6. Note that the interface constitutes a fast diffusion path (as grain boundaries) which might here play a significant role. As a result, the dynamic evolution of diffusion and phase propagation processes would induce local deviations in

phase boundary composition. A non-equilibrium situation is then to consider at the propagating interface.

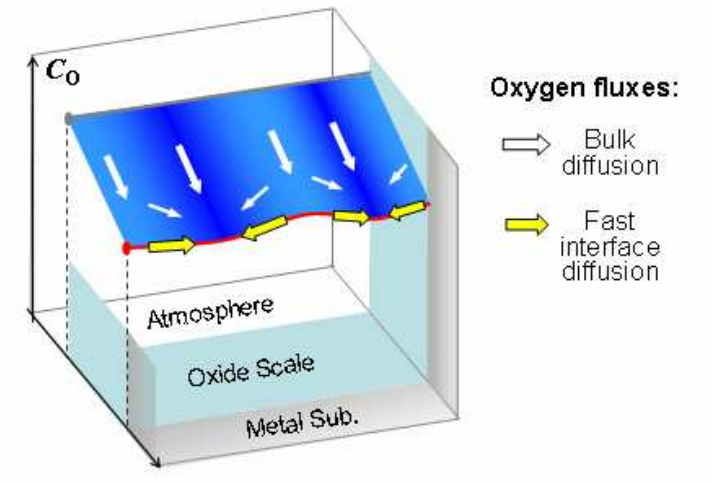

Figure 2.6: Schematic of the redistribution of incoming oxygen fluxes at the metal/oxide boundary induced by composition variation along the interface.

In order to model the stress contribution on the interface composition, a local thermodynamic treatment of the phase boundary propagation is performed, allowing for the simulation of a complex non-uniform phenomenon. A continuum mechanics description of a dissipative sharp interface propagation is derived to include the influence of the stress state and phase transformation accommodation work on the phase boundary propagation kinetics (Saillard, Cherkaoui et al. 2009). This thermodynamic approach, extensively developed over the last decades (see (Fried and Gurtin 2004) for general treatment and references), allows for a direct description of the stress, composition and morphology influences on the local interface motion kinetics. A practical example can be found in (Fischer, Simha et al. 2003) for an austenitic→ferritic phase change at 800°C. Very few works have considered a mechanical coupling with phase boundary

propagation during high-temperature oxide scale growth. Garruchet et al. derived an interfacial thermodynamic model to investigate an effect of epitaxial stress on the growth kinetics of a ZrO_2 layer on a zirconium substrate at 600°C (Garruchet, Montesin et al. 2004). Creton et al. used a similar approach to investigate stress development associated with the oxidation of an uranium dioxide substrate at 300°C (Creton, Optasanu et al. 2009). On top of the classical free energy change under small strains, the derivation presented here considers the mass diffusion fluxes, the mass consumption and the deformation work during the phase transformation process, and it incorporates the contribution of the possible large volumetric strain associated with the metal oxidation.

2.4 Time scale analysis

Several processes are involved in the mechanism of stress-affected oxidation. They act at different length and time scales which are essential to assess in view of developing a coherent model at the length scale of interest. We focus here on the oxide scale growth, driven by diffusion through the oxide layer. The length scale of interest is therefore the micrometer. From Fick's second law, the time scale of a diffusion process, τ_{diff}, is given by:

$$\tau_{diff} = \frac{\chi_{diff}^2}{D} \tag{2.6}$$

where χ_{diff} is the associated diffusion length scale and D is the diffusivity of the considered species in the given medium. From mass conservation at the propagating phase boundary, equation (1.10), and assuming furthermore a negligible solubility of the

diffusing species in the parent phase (oxygen in the metallic substrate here), the time scale for the oxide growth is:

$$\tau_{growth} = \frac{C^I}{J} \chi_{growth} . \tag{2.7}$$

Here C^I denotes the concentration at the interface, and J is the incoming flux, of the species controlling the phase boundary propagation. This expression assumes that the local oxidation reaction is much faster that the controlling diffusion process, so that it can always be considered at steady-state at the oxide growth time scale. This assumption is justified by the fact that the oxidation reaction rate at high temperature is much higher than the time scale for the ionic diffusion through the solid oxide.

Finally, Fick's first law allows expressing the diffusion species flux, J_{diff}, as:

$$J_{diff} = D \frac{\Delta C_{diff}}{\chi_{diff}} \tag{2.8}$$

where ΔC_{diff} is the species concentration variation over the considered distance χ_{diff}. Assuming that the oxide growth is controlled by a single species diffusion, equation (2.7) can be combined with equations (2.8) and (2.6) to yield:

$$\tau_{growth} = \frac{C^I}{\Delta C_{diff}} \tau_{diff} . \tag{2.9}$$

The considered phases, alumina and chromia, exhibit a very high stoichiometry (Birks, Meier et al. 2006). As a consequence, any variation of concentration within the oxide scale is small in front of the concentration value, and therefore: $\Delta C_{diff} \ll C^I$. Thus the

oxide growth is much slower than the driving diffusion process. The phase propagation is even slower compared to the diffusion process through the phase boundary, whose thickness is of the order of the nanometer (a micrometer length scale is considered for the oxide growth-driving diffusion). Therefore a chemical composition equilibrium can be considered through the interface.

In a one-dimensional description in which the oxide scale development can be directly related to a simple diffusion through the growing layer, a quasi-steady state concentration gradient then establishes, as previously discussed. The concentration at the propagating boundary is constant and given by the local phase equilibrium.

This simple local equilibrium can no more be assumed in a more complex case in which stress and geometry evolutions affect the local phase equilibrium composition. Indeed, the diffusion processes being much faster than the oxide phase propagation, the respective times for response to a stress or geometry variation will significantly differ, resulting in a dynamic non-equilibrium situation.

2.5 Mechanical description

A control volume is considered, undergoing a phase change such that at time t there is a surface, $\Gamma(t)$, which defines the boundary between the untransformed (Ω^+) and transformed (Ω^-) volumes of the material (see Figure 2.7). During this process, $\Gamma(t)$ propagates through the material with a velocity $\mathbf{v}_\Gamma$, with a normal component defined by:

$$v_n = \mathbf{v}_\Gamma \cdot \mathbf{n} \tag{2.10}$$

where $\mathbf{n}$ is the normal vector to the interface.

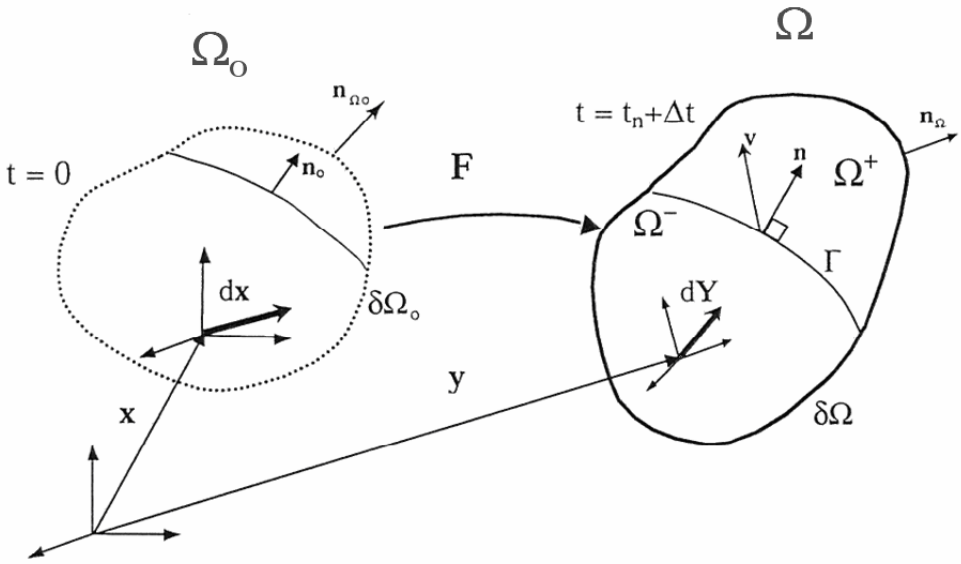

Figure 2.7: Discontinuity in current configuration Ω moving with a velocity $\mathbf{v}_\Gamma$.

The volume considered is modeled with two continuum media separated by a sharp interface, as shown in Figure 2.7. The location vectors for each particle in the reference configuration are given by $\mathbf{x}$ and, at time t, by $\mathbf{y}$, respectively. Then, the displacement of the particle is:

$$\mathbf{u}(\mathbf{x},t) = \mathbf{y}(\mathbf{x},t) - \mathbf{x}\,, \tag{2.11}$$

and the corresponding deformation gradient and material velocity at time t are:

$$\mathbf{F} = \partial_{\mathbf{x}}\mathbf{y}\,, \tag{2.12}$$

$$\mathbf{v} = \partial_t \mathbf{u}\,. \tag{2.13}$$

The quantities in the undeformed or reference configuration will be identified by a subscript zero, see Figure 2.7. Since continuum media are considered, any volume change is the result of a mechanical deformation, such that the volume ratio of the current configuration to the reference one can be obtained through the deformation gradient:

$$\det(\mathbf{F}) = \frac{V}{V_0} \tag{2.14}$$

The interface is assumed coherent at the continuum mechanics description scale, implying that $\mathbf{y}(\mathbf{x},t)$ is continuous across the interface, but that the material velocities and the deformation gradients are discontinuous. Using subscripts + and – for the limiting values of a quantity α when the interface is approached from the Ω^+ and Ω^- domains, respectively, its jump is:

$$[\alpha] = \alpha^+ - \alpha^- \text{ on } \Gamma(t)\,. \tag{2.15}$$

The discontinuities of the velocity and the deformation gradient can be related through the Hadamard compatibility condition:

$$[\mathbf{v}] = -[\mathbf{F}]\ \mathbf{n}\ v_n \qquad \text{on } \Gamma(t)\,. \tag{2.16}$$

For a local and updated description of the volume change associated with the phase oxidation, an effective measure is employed, Π_I, obtained through:

$$\Pi_I = \frac{V_{eq}^-}{V^+} = \frac{\det(\mathbf{F}^-)}{\det(\mathbf{F}^+)} \tag{2.17}$$

where V_{eq}^{-} stands for the volume of the transformed and accommodated phase, equivalent to the volume of the original phase V^{+} before its oxidation.

The global or weak form of the balance of linear momentum for quasi-static conditions requires that the equations of motion in the deformed state be such that the vector sum of the external forces $\mathbf{f}$ in Ω is equal to the rate of change of momentum. Application of the divergence theorem in the absence of body forces on any arbitrary volume Ω leads to:

$$\int_{\delta\Omega} d\mathbf{f} = 0 = \int_{\delta\Omega} \sigma\, \mathbf{n}_{\Omega} dS = \int_{\Omega} \mathrm{div}(\sigma)\, dV\,, \tag{2.18}$$

where σ represents the Cauchy-stress tensor and $\mathbf{n}_{\Omega}$ is the outward normal vector at the external boundary. At points where the displacements, $\mathbf{u}$, vary smoothly, equation (2.18) leads to the equilibrium condition:

$$\mathrm{div}(\sigma) = \nabla \cdot \sigma = \mathbf{0}\,. \tag{2.19}$$

Finally, the equilibrium condition at the solid-solid interface requires that, if any surface stress phenomena are neglected, the traction, $\mathbf{t}$, must be continuous across the boundary:

$$[\mathbf{t}] = [\sigma]\mathbf{n} = \mathbf{0} \qquad \text{on } \Gamma(t)\,. \tag{2.20}$$

Note that when the system can be considered in elastostatic equilibrium, a surface tension term must be added across a curved interface (Angheluta, Jettestuen et al. 2008):

$$[\mathbf{t}] = [\sigma]\mathbf{n} = -\gamma_I\, \kappa\, \mathbf{n} \qquad \text{on } \Gamma(t) \tag{2.21}$$

where κ represents the local interface curvature and γ_I is the phase boundary interfacial energy (then typically named surface tension). However, this situation results from a global configuration equilibrium which can only be achieved at any time by liquids and sufficiently accommodating purely elastic solids when the phase boundary propagation is much slower than the elastic relaxation time for the system. It is not valid for visco-plastic and low accommodating solids which can maintain a non-equilibrium interface morphology.

2.6 Chemical description

The considered volume, Ω, is composed of a different phase on each side of the sharp boundary $\Gamma(t)$. In the considered materials at high temperature, both ionic species and defects diffuse within each phase bulk and through the interface.

Mass conservation in the absence of volume mass source or sink requires that in the deformed state the sum of the external mass fluxes on Ω be equal to the global rate of change of concentration. Application of the divergence theorem on any arbitrary volume Ω leads to:

$$\int_{\Omega}\left(\operatorname{div}(\mathbf{J}_i)+\frac{dC_i}{dt}\right)d\mathrm{V}=0 \tag{2.22}$$

where $\mathbf{J}_i$ and C_i represent the species flux vector and concentration, respectively. At points where the concentration vary smoothly, equation (2.22) leads to the equilibrium condition (local mass balance for a given species i):

$$\frac{dC_i}{dt} = -\operatorname{div}(\mathbf{J}_i) = -\nabla \cdot \mathbf{J}_i \tag{2.23}$$

The two phases are assumed to present distinct chemical compositions, such that the propagation of the child phase over the parent one locally induces mass "trapping" within the formed material and "release" from the dissolved one. The local mass balance associated with the phase boundary propagation is given by:

$$\left[\mathbf{J}_i \cdot \mathbf{n}\right] = \left\{C_i^+ - \Pi_I C_i^-\right\}\, v_n \tag{2.24}$$

The global mass conservation for a species *i* over a volume embedding the phase boundary is then:

$$\int_{\Omega_0} \left(\nabla \cdot \mathbf{J}_i + \frac{dC_i}{dt} \right) \det(\mathbf{F})\, d\mathrm{V}_0 = \int_\Gamma \left(-\left[\mathbf{J}_i \cdot \mathbf{n}\right] + \left\{C_i^+ - \Pi_I C_i^-\right\}\, v_n \right) dS \tag{2.25}$$

The terms involving concentration in this expression denote the two contributions in mass storage during the phase boundary propagation: phase transformation and phase composition change.

The model of a sharp interface requires conditions relating the chemical potentials on each side of the discontinuity. At this point, there is a need to differentiate interstitial species from those occupying regular lattice sites, also known as substitutional species (Mullins and Sekerka 1985; Fried and Gurtin 2004). Due to the lattice constraint, i.e. the conservation of the finite number of lattice sites available for a given substitutional species, these species can only diffuse through a vacancy mechanism. Thus the flux of a substitutional species *i* is coupled with an opposite flux of vacancies v_i:

$$\mathbf{J}_{v_i} = -\mathbf{J}_i \quad \text{for any substitutional species } i\,. \tag{2.26}$$

The diffusion potential of substitutional species, also called relative or virtual potential, is then defined by (Lankhorst, Bouwmeester et al. 1997; Swaminathan, Qu et al. 2007):

$$\tilde{\mu}_i = \mu_i - \mu_{v_i}\,. \tag{2.27}$$

This potential can be used instead of the true species potential in energy balances to avoid dealing directly with defects. The diffusion potential of interstitial species is assumed to reduce to the chemical potential. The local chemical equilibrium at the phase boundary requires that the diffusion potentials be continuous across the interface, for both interstitial and substitutional species:

$$\left[\mu_i\right] = 0\,, \tag{2.28}$$

in which the relative potential must be used for substitutional species (Fried and Gurtin 2004).

2.7 Driving force for phase boundary propagation

The propagation of the phase boundary is accompanied by an energy dissipation, whose value per unit length of propagation constitutes the driving force for the process. It is derived in this section. The control volume described in Figure 2.7 is considered to undergo external mechanical forces and mass fluxes. The global rate of dissipation, *G*, is

given by the difference between the rate of external work (in a general thermodynamic sense), P_e, and the rate of change of the total Helmholtz free energy, $\dot{\Psi}$:

$$G = P_e - \dot{\Psi} . \tag{2.29}$$

Note that this formulation assumes isothermal conditions and constant kinetic energy for the body.

2.7.1 Power of external forces

In the absence of body forces, the power is that developed by the external forces on the boundary $\delta\Omega$ and by the flow of diffusing species across $\delta\Omega$:

$$P_e = \int_{\delta\Omega} \mathbf{t} \cdot \mathbf{v} \, dS - \int_{\delta\Omega} \tilde{\mu}_i \mathbf{J}_i \cdot \mathbf{n}_\Omega \, dS , \tag{2.30}$$

where $\mathbf{t}$ is the traction, $\mathbf{v}$ is the material velocity, and $\tilde{\mu}_i$ and $\mathbf{J}_i$ are the diffusion potential and flux, respectively, of any diffusing species through the external boundary of outward normal vector $\mathbf{n}_\Omega$. Furthermore, the Einstein notation is used so that the double indices indicate a summation over the species. Then,

$$\int_{\delta\Omega} \mathbf{t} \cdot \mathbf{v} \, dS = \int_{\delta\Omega} \left(\sigma \, \mathbf{n}_\Omega \right) \cdot \mathbf{v} \, dS = \int_{\delta\Omega} \left(\sigma \, \mathbf{v} \right) \cdot \mathbf{n}_\Omega \, dS . \tag{2.31}$$

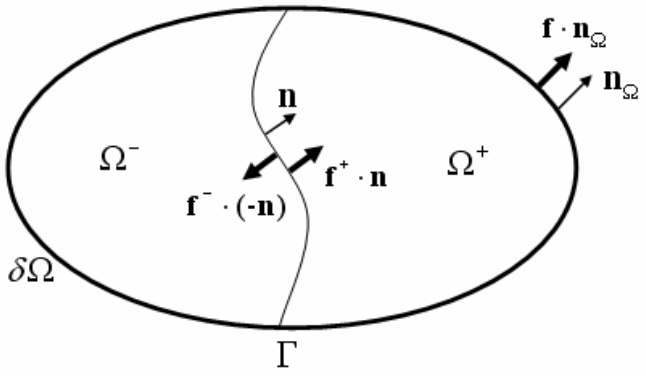

Figure 2.8: Thermodynamic forces on the domain boundary and the interface.

Application of the Gauss theorem on the domain Ω as described in Figure 2.8, embedding the surface discontinuity Γ and subjected to the action of $\mathbf{f} = (\sigma\,\mathbf{v} - \tilde{\mu}_i \mathbf{J}_i)$ yields:

$$P_e = \int_\Omega \nabla \cdot (\sigma\,\mathbf{v} - \tilde{\mu}_i \mathbf{J}_i)\, dV + \int_\Gamma \left[(\sigma\,\mathbf{v} - \tilde{\mu}_i \mathbf{J}_i) \right] \cdot \mathbf{n}\, dS\,. \tag{2.32}$$

Furthermore,

$$[\sigma\,\mathbf{v}] \cdot \mathbf{n} = [\sigma\,\mathbf{n} \cdot \mathbf{v}] = \sigma\,\mathbf{n} \cdot [\mathbf{v}] \tag{2.33}$$

since $\sigma^+ \mathbf{n} = \sigma^- \mathbf{n} = \sigma\,\mathbf{n}$ over Γ by traction continuity (equation (2.20)). This term can be rewritten in terms of the Hadamard compatibility conditions (equation (2.16)) as follows,

$$\sigma\,\mathbf{n} \cdot [\mathbf{v}] = -\sigma\,\mathbf{n} \cdot [\mathbf{F}]\mathbf{n}\, v_n\,. \tag{2.34}$$

An admissible discontinuity in the deformation gradients across the interface Γ requires that

$$[\mathbf{F}] \propto \mathbf{n}. \tag{2.35}$$

Thus, let $\mathbf{r}$ be an arbitrary proportionality vector so that $[\mathbf{F}] = \mathbf{r} \otimes \mathbf{n}$, where the tensor product is used: $(\mathbf{a} \otimes \mathbf{b})_{ij} = a_i b_j$. Substituting into equation (2.34) leaves:

$$\sigma\, \mathbf{n} \cdot [\mathbf{v}] = -\sigma\, \mathbf{n} \cdot (\mathbf{r} \otimes \mathbf{n})\mathbf{n}\, v_n = -\sigma : [\mathbf{F}] v_n. \tag{2.36}$$

where **:** represents the double contraction operator ($\mathbf{A} : \mathbf{B} \equiv A_{ij} B_{ij}$). Moreover, the continuity of traction at the interface allows the vector to be expressed through the limit values of the stress tensors within the continuous domains:

$$\sigma\, \mathbf{n} = \tfrac{1}{2}(\sigma^{+} + \sigma^{-})\mathbf{n} \tag{2.37}$$

Additionally, the continuity of diffusion potentials at the interface, equation(2.38), along with the local mass balance, equation (2.24), yields:

$$[\mu_i \mathbf{J}_i] \cdot \mathbf{n} = \tilde{\mu}_i \left\{ C_i^{+} - \Pi_I C_i^{-} \right\}\, v_n\,. \tag{2.39}$$

Introducing the developments into equation (2.32), the surface integral of the power dissipation over the phase boundary is:

$$P_e^{\Gamma} = \int_{\Gamma} \left(-\frac{1}{2}\left(\sigma^{+} + \sigma^{-}\right) : [\mathbf{F}] - \mu_i \left\{ C_i^{+} - \Pi_I C_i^{-} \right\} \right) v_n\, dS\,. \tag{2.40}$$

2.7.2 Time evolution of the Helmholtz free energy

The time evolution of the Helmholtz free energy, $\dot{\Psi}$, can be written in terms of the total free energy density *W*:

$$\dot{\Psi} = \frac{d}{dt}\int_{\Omega} W dV \,. \tag{2.41}$$

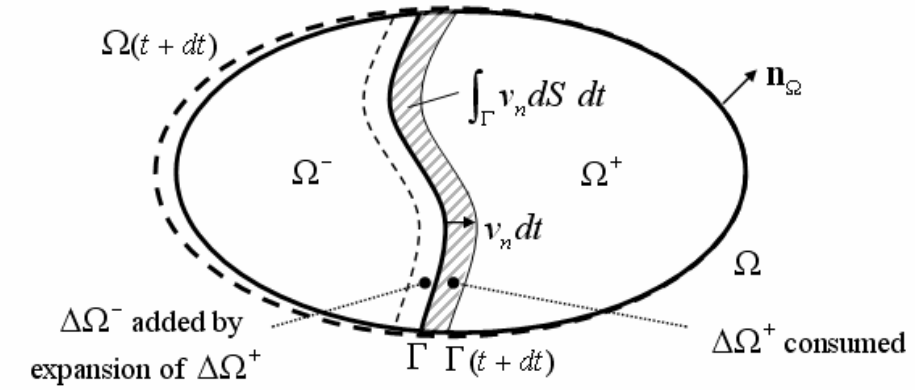

Figure 2.9: Infinitesimal time evolution of the system.

As illustrated in Figure 2.9, the change of the total free energy with time includes three components: one associated with the time variation of the total free energy density W within Ω^- and Ω^+, i.e. Ω overall; and two others associated with the change in volume of the domains Ω^- and Ω^+, due to the motion of the external boundary on one hand, and of the interface Γ on the other hand:

$$\frac{d}{dt}\int_{\Omega} W\ dV = \int_{\Omega} \frac{dW}{dt}\ dV + \int_{\delta\Omega} W\ \mathbf{v}\cdot\mathbf{n}_{\Omega} dS - \int_{\Gamma}\left\{W^+ - \Pi_I W^-\right\} v_n dS \,. \tag{2.42}$$

The local motion of the system's external boundary can be rewritten in terms of a small change in the global volume:

$$\mathbf{v}\cdot\mathbf{n}_{\Omega} dS = \frac{d}{dt}(dV) = \frac{d}{dt}\left\{\det(\mathbf{F})\right\}\ dV_0 \,. \tag{2.43}$$

Consequently, the two first terms on the right hand side of equation (2.42) can be combined and the time rate of change of the Helmholtz free energy can be written as the sum of two integrals, one over the original domain and another over the present phase boundary surface:

$$\dot{\Psi} = \int_{\Omega_0} \frac{d}{dt}\left\{W \det(\mathbf{F})\right\}\, dV_0 - \int_{\Gamma}\left\{W^{+} - \Pi_I W^{-}\right\}\, v_n dS\,. \tag{2.44}$$

Only the last term is related to the phase boundary propagation and is then of interest here. The total free energy density W includes contributions from the stored elastic energy density, W^e, and the chemical free energy density,

$$W^c = \mu_i C_i\ , \tag{2.45}$$

where μ_i and C_i stand for the chemical potential and concentration, respectively, of any species *i* present in the phase considered. Note that the Einstein notation is again used so that the double indices indicate a summation over the species. At the interface, a specific thermodynamic force induced by the gradient of local curvature along the interface applies, tending to flatten the boundary in order to reduce its surface and thus the global interfacial energy (Mullins 1957). This effect can be directly introduced in the time evolution of the free energy induced by the phase boundary propagation, which then overall can be expressed by:

$$\dot{\Psi}^{\Gamma} = \int_{\Gamma} -\left(\left\{\mu_i^{+} C_i^{+} - \Pi_I \mu_i^{-} C_i^{-}\right\} + \left\{W^{e,+} - \Pi_I W^{e,-}\right\} + \kappa\ \gamma_I\ \right)\ v_n\ dS\,. \tag{2.46}$$

where κ represents the local interface curvature and γ_I is the phase boundary energy.

2.7.3 Driving force for phase boundary propagation

The global rate of dissipation induced by the phase boundary propagation can now be obtained by substitution of equation s (2.40) and (2.46) into (2.29):

$$G^{\Gamma} = P_e^{\Gamma} - \dot{\Psi}^{\Gamma} = \int_{\Gamma} \Big(-\tilde{\mu}_i \left\{ C_i^+ - \Pi_I C_i^- \right\} + \left\{ \mu_i^+ C_i^+ - \Pi_I \mu_i^- C_i^- \right\} + \kappa\, \gamma_I \\ -\frac{1}{2}\left(\sigma^+ + \sigma^-\right) : [\mathbf{F}] + \left\{ W^{e,+} - \Pi_I W^{e,-} \right\} \Big) v_n \, dS \quad . \tag{2.47}$$

The term within brackets represents the energy dissipated by the phase boundary local propagation for given compositions as well as the stress and strain situation on each side of the sharp interface. The three first components account for the diffusion of species at the interface, the chemical reaction taking place at the phase boundary and the morphology of the discontinuity, respectively, while the two last include a contribution of the local mechanical stress state. Overall they constitute the driving force for the phase boundary propagation, f_I:

$$f_I = -\tilde{\mu}_i \left\{ C_i^+ - \Pi_I C_i^- \right\} + \left\{ \mu_i^+ C_i^+ - \Pi_I \mu_i^- C_i^- \right\} + \kappa\, \gamma_I \\ -\frac{1}{2}\left(\sigma^+ + \sigma^-\right) : [\mathbf{F}] + \left\{ W^{e,+} - \Pi_I W^{e,-} \right\} \tag{2.48}$$

It can be deduced from this formulation that interstitial species do not contribute to the driving force ($\tilde{\mu}_i = \mu_i$ so the term cancels with the chemical free energy), but that only substitutional species contribute through the vacancy potential ($\tilde{\mu}_i - \mu_i = -\mu_{\mathrm{V}_i}$). Assuming that oxygen is the only species diffusing through a vacancy mechanism at the interface, we obtain:

$$f_I = \left\{\mu_{\mathrm{V}}^{+} C_{\mathrm{O}}^{+} - \mu_{\mathrm{V}}^{-} \Pi_I C_{\mathrm{O}}^{-}\right\} + \kappa\, \gamma_I - \frac{1}{2}\left(\sigma^{+} + \sigma^{-}\right) : [\mathbf{F}] + \left\{W^{e,+} - \Pi_I W^{e,-}\right\} \qquad (2.49)$$

The driving force for the phase boundary local propagation then includes two stress contributions: the work required to complete the deformation associated with the phase transformation at the stressed interface, $\frac{1}{2}\left(\sigma^{+} + \sigma^{-}\right) : [\mathbf{F}]$, and the change in elastic energy of the transformed volume over the process, $\left\{\Pi_I W^{e,-} - W^{e,+}\right\}$.

2.8 Phase boundary propagation kinetics

Under purely elastic and isothermal conditions, the second law of thermodynamics requires that on Γ,

$$f_I\, v_n \geq 0\ , \qquad (2.50)$$

and implies that, when the driving force is different from zero, the motion of Γ induces dissipation. We can note that this statement is probably too restrictive for most solids undergoing inelastic deformation. In such cases, the motion of the interface Γ is expected to start when

$$f_I \geq f_R\ , \qquad (2.51)$$

where f_R is a threshold value related to the nature of the interaction between the moving boundary and different types of defects. The actual driving force for the phase boundary propagation must then be defined as the difference between the two terms. Since we are interested in the stress influence only, the driving force corresponding to a flat stress-free

phase boundary is denoted f_I^0 in order to highlight deviation terms:

$$f_I^0 = \left\{\mu_{\mathrm{V}}^{0+} C_{\mathrm{O}}^{+} - \mu_{\mathrm{V}}^{0-} \Pi_I C_{\mathrm{O}}^{-}\right\} - f_R \tag{2.52}$$

We assume furthermore that the local oxygen concentration deviations at the phase boundary remain negligible in front of the reference value, which means that the vacancy density is much lower than the oxygen concentration at the oxide interface. This is justified by the fact that the considered oxides, alumina and chromia, are known to exhibit a very high stoechiometry (i.e. a very low composition defect density) within the bulk (Birks, Meier et al. 2006). This property is just extended here to the interface. Then $\left\{C_{\mathrm{O}}^{+} - \Pi_I C_{\mathrm{O}}^{-}\right\}$ is constant, as well as f_I^0, and the driving force for the phase boundary propagation can be rewritten:

$$\begin{aligned} f_I = f_I^0 + \left\{\left(\mu_{\mathrm{V}}^{+} - \mu_{\mathrm{V}}^{0+}\right) C_{\mathrm{O}}^{+} - \left(\mu_{\mathrm{V}}^{-} - \mu_{\mathrm{V}}^{0-}\right) \Pi_I C_{\mathrm{O}}^{-}\right\} \\ + \kappa\, \gamma_I - \frac{1}{2}\left(\sigma^{+} + \sigma^{-}\right) : [\mathbf{F}] + \left\{W^{e,+} - \Pi_I W^{e,-}\right\} \end{aligned} . \tag{2.53}$$

The second term on the right hand side is introduced to account for the non-negligible effect of vacancy density variations on the defect chemical potential.

For a quasi-static one-dimensional problem, quasi-equilibrium can be assumed (see discussion in the global model description) and therefore the phase boundary composition can be obtained through the resolution at any time of the equation $f_I = 0$. However, under the non-equilibrium thermodynamic conditions which prevail here, the kinetics of phase transformation needs to be defined as a kinetic relation between the rate v_n at which the weak discontinuity moves and the driving force. Considering a quasi-static

propagation process, $f_I \approx 0$, a linear kinetic relation is assumed (Fischer, Simha et al. 2003; Fried and Gurtin 2004; Angheluta, Jettestuen et al. 2008):

$$v_n = M_I f_I \tag{2.54}$$

where M_I is the phase boundary mobility and constitutes a temperature-dependent parameter for the phase boundary propagation process.

2.9 Comments

The formulation derived is local and treats the propagation of a sharp phase boundary associated with solid phase transformation. It is important to note that this formulation applies to a mesoscopic scale, at which continuous bulk properties and fields can be defined. It then theoretically applies to a monocrystal. The considered phase transformation, metal oxidation, induces a composition change. Therefore mass conservation, equation (2.25), must be resolved along with the phase boundary propagation, equation (2.54). Thus, a stress-induced deviation in the propagation kinetics is locally coupled with a composition variation, counter-balanced by species diffusion.

Oxidation at the outer interface does not involve solid phase transformation since the oxide is exposed to a gaseous phase or a coating layer which is not consumed during outward oxide growth. A phase growth takes place, i.e. new oxide is formed on top of the existing oxide surface, possibly pushing upward the coating layer if present. The formulation derived does not apply for such a process. A simple mass conservation of the

oxide-forming metallic ion (Cr or Al) with a constant boundary concentration can be employed or a specific formulation should be derived to include a stress contribution.

Finally, it is important to note that no assumption have been made on the mechanical behavior and associated constitutive formulations for the two involved phases, aside from a continuum mechanics framework. The interface has been assumed to be coherent, but this condition can be removed if a non-dissipative (frictionless) slip can be considered, as demonstrated by Fischer et al. (Fischer, Simha et al. 2003). Also no specific formulation has been defined so far for the vacancy chemical potential. Therefore the model derived can be applied with a broad range of mechanical and chemical models for the two involved materials.

2.10 References

Angheluta, L., E. Jettestuen, J. Mathiesen, F. Renard and B. Jamtveit (2008). "Stress-driven phase transformation and the roughening of solid-solid interfaces." Physical Review Letters **1**(9): 4.

Birks, N., G. H. Meier and F. S. Pettit (2006). Introduction to the high-temperature oxidation of metals. New York, Cambridge University Press.

Busso, E. P., J. Lin, S. Sakurai and M. Nakayama (2001). "A mechanistic study of oxidation-induced degradation in a plasma-sprayed thermal barrier coating. Part i: Model formulation." Acta Materialia **49**: 1515-1528.

Busso, E. P. and Z. Q. Qian (2006). "A mechanistic study of microcracking in transversely isotropic ceramic-metal systems." Acta Materialia **54**: 3325-338.

Creton, N., V. Optasanu, T. Montesin, S. Garruchet and L. Desgranges (2009). "A thermodynamic approach of the mechano-chemical coupling during the oxidation of uranium dioxide." Defect and Diffusion Forum **289 - 292**: 447-454.

Essuman, E., G. Meier, J. Zurek, M. Hänsel, L. Singheiser and W. Quadakkers (2007). "Enhanced internal oxidation as trigger for breakaway oxidation of fe–cr alloys in gases containing water vapor." Scripta Materialia **57**: 845-848.

Evans, H. E. (1995). "Stress effects in high-temperature oxidation of metals." International Materials Reviews **40**(1): 1-40.

Favergeon, J., T. Montesin and G. Bertrand (2005). "Mechano-chemical aspects of high temperature oxidation: A mesoscopic model applied to zirconium alloys." Oxidation of Metals **64**(3-4): 253-279.

Fergus, J. W. (2005). "Metallic interconnects for solid oxide fuel cells." Materials Science and Engineering **A397**: 271-283.

Fischer, F. D., N. K. Simha and J. Svoboda (2003). "Kinetics of diffusional phase transformation in multicomponent elastic-plastic materials." Journal of Engineering Materials and Technology-Transactions of the ASME **125**(3): 266-276.

Fried, E. and M. E. Gurtin (2004). "A unified treatment of evolving interfaces accounting for small deformations and atomic transport with emphasis on grain-boundaries and epitaxy." Advances in Applied Mechanics **40**: 1-177.

Garruchet, S., T. Montesin, H. Sabar, M. Salazar and G. Bertrand (2004). "An interfacial thermodynamic model for the oxidation kinetics of a metal: Epitaxial stress effects." Materials Science Forum: 611-618.

Hou, P. Y. and J. Stringer (1995). "The effect of reactive element additions on the selective oxidation, growth and adhesion of chromia scales." Materials Science and Engineering a-Structural Materials Properties Microstructure and Processing **A202**(1-2): 1-10.

Huntz, A. M. (1999). "Parabolic laws during high temperature oxidation: Relations with the grain size and thickness of the oxide." Journal of Materials Science Letters **18**: 1981-1984.

Lankhorst, M. H. R., H. J. M. Bouwmeester and H. Verweij (1997). "Thermodynamics and transport of ionic and electronic defects in crystalline oxides." Journal of the American Ceramic Society **80**(9): 2175-2198.

Larche, F. and J. W. Cahn (1982). "The effect of self-stress on di)usion in solids." Acta Metallurgica **30**: 1835-1845.

Larche, F. and J. W. Cahn (1985). "The interactions of composition and stress in crystalline solids." Acta Metallurgica **33**: 333-357.

Mullins, W. and R. Sekerka (1985). "On the thermodynamics of crystalline solids." Journal of Chemical Physics **82**(11): 5192-5202.

Mullins, W. W. (1957). "Theory of thermal grooving." Journal of Applied Physics **28**(3): 333-339.

Naumenko, D., B. Gleeson, E. Wessel, L. Singheiser and W. J. Quadakkers (2007). "Correlation between the microstructure, growth mechanism, and growth kinetics of alumina scales on a fecraly alloy." Metallurgical and Materials Transactions a-Physical Metallurgy and Materials Science **38A**: 2974-2983.

Padture, N. P., M. Gell and E. H. Jordan (2002). "Materials science - thermal barrier coatings for gas-turbine engine applications." Science **296**(5566): 280-284.

Saillard, A., M. Cherkaoui, L. Capolungo and E. P. Busso (2009). "Stress influence on high temperature oxide scale growth: Modeling and investigation on a thermal barrier coating system." Submitted to Philosophical Magazine.

Swaminathan, N., J. Qu and Y. Sun (2007). "An electrochemomechanical theory of defects in ionic solids. I. Theory." Philosophical Magazine **87**(11): 1705-1721.

Wu, C. H. (2001). "The role of eshelby stress in composition-generated and stress-assisted diffusion." Journal of the Mechanics and Physics of Solids **49**: 1771-1794.

Yang, Z. G. (2008). "Recent advances in metallic interconnects for solid oxide fuel cells." International Materials Reviews **53**(1): 39-54.

CHAPTER 3

PHENOMENOLOGICAL & NUMERICAL FRAMEWORK

3.1 Introduction

In order to practically apply the developed model of stress-affected inner oxidation, a macroscopic phenomenological framework must be defined and a numerical method set up in order to perform global realistic simulations of high temperature oxide scale growth. A flowchart presenting the different processes of the global model and their interactions is presented in Figure 3.1.

The purpose of the macroscopic model is to capture the essential processes involved in oxide scale growth and related stress development, while introducing the most influent physical and particularly material-dependent parameters. Species diffusion is the main process, since it controls the rate of oxidation. The contributions of fast-diffusion paths like grain boundaries and interfaces must be included. Growth strain development within the oxide scale associated with the oxidation process should also be included, since it has been shown to be the most likely dominant phenomenon in the establishment of the stress level at oxidation temperature, at least under isothermal conditions but probably also under thermal cycling. Finally, an adequate elasto-visco-plastic behavior must be defined for the oxide and metal materials in order to obtain a realistic response to the growth strain development.

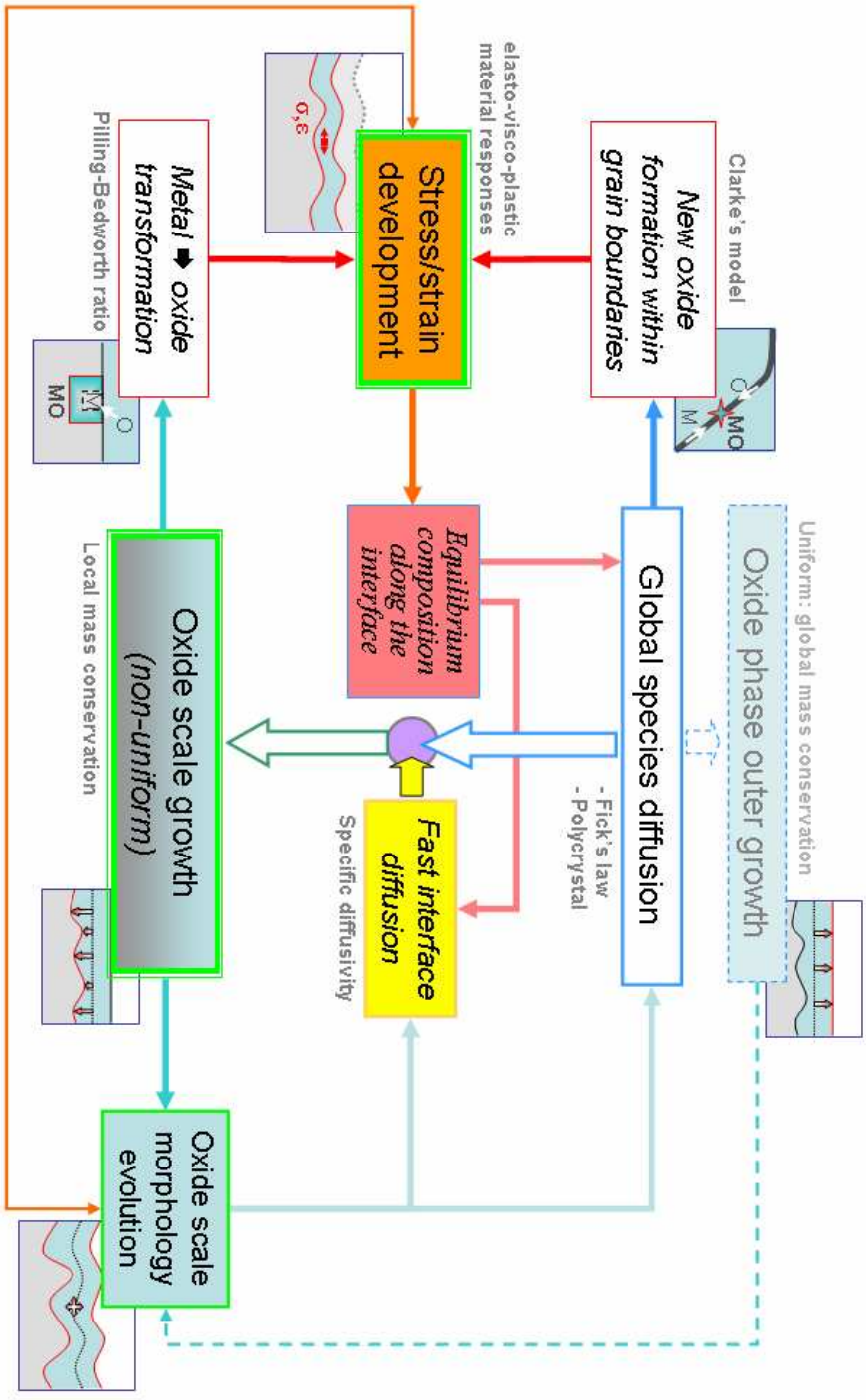

Figure 3.1: Flowchart presenting the global model processes and their interactions. Specificities about the models are included in grey font.

The build up of a numerical framework for the simulation of realistic cases with the developed model has constituted a major task of this work. In fact, the time evolution of the stress/strain and diffusion fields must be resolved within the two distinct phase domains, separated by a sharp boundary propagating over the parent phase. For complete simulation capacities based on the developed model of stress/affected oxidation, the phase boundary propagation should depend on the evolving stress and diffusion fields on each side of the sharp discontinuity. The induced modification of the material system geometry along with the generation of phase transformation strains in turn affect the continuous fields. Therefore a complete coupling is to be resolved. In addition, local processes occurring along the phase boundary have to be accounted for, such as fast diffusion along the interface and phase transformation volume strain, which render the numerical problem even more complex. A specific simulation tool has been built based on a finite element method coupled with an external routine for the phase boundary propagation.

3.2 Mass diffusion framework

3.2.1 Diffusion in ionic solids

A classical formulation for composition driven species diffusion through thick film (thickness above around 0.1µm (Atkinson 1985)) under isothermal conditions considers the chemical potential μ as the driving force. The particle or defect current density can then be expressed by (Atkinson 1985):

$$\mathbf{J}_i = -D_i^{\varphi} \frac{C_i}{R\theta} \nabla \mu_i \tag{3.1}$$

where D_i^{φ} is the isotropic diffusivity of species *i* in phase φ, *R* is the molar gas constant and θ is the absolute temperature in Kelvin. Local electroneutrality is assumed in this formulation, which is a reasonable assumption for oxides at high temperature considering that electronic charges circulate much faster than ionic species (Atkinson 1985). The chemical potential is obtained assuming furthermore that the defects are in ideal solution, thus neglecting their self-interaction. This hypothesis is only valid for a very low defect density, which is the case for vacancies in chromia and alumina crystals (Birks, Meier et al. 2006). Under these assumptions the chemical potential can then be expressed by:

$$\mu_i = \mu_i^{\circ} + R\theta \ln\left(c_i\right) \tag{3.2}$$

where μ_i° is the standard chemical potential of species *i* in a reference state of phase and temperature, and c_i is the species mole fraction, defined by:

$$c_i = \frac{n_i}{n_{total}} = \frac{C_i}{\sum_j C_j} \approx k\ C_i \tag{3.3}$$

where n_i is the number of moles of species *i* for a given volume considered, and the subscript "*total*" stands for the summation over all the present species. The approximation is obtained assuming that the composition of the phase deviates only slightly from the stoechiometry (i.e. the species mole fractions relative variations over the domain are small) and that the phase specific volume is also quite uniform. Then the total concentration of atoms is approximately constant and there is a proportionality

relationship between species mole fraction and concentration. Note that combining equations (3.1), (3.2) and (3.3) leads to the classical Fick's first law,

$$\mathbf{J}_i = -D_i^{\varphi} \nabla C_i , \tag{3.4}$$

which is then recovered with the assumptions made.

Oxygen anion diffusion is considered in this work. It is assumed to be a substitutional species, diffusing through a vacancy mechanism. Thus, its diffusion engenders the creation and annihilation of vacancies, and a diffusion potential should be considered in equation (3.1), $\tilde{\mu}_{\mathrm{O}} = \mu_{\mathrm{O}} - \mu_{\mathrm{V}}$ (Lankhorst, Bouwmeester et al. 1997; Swaminathan, Qu et al. 2007). However, under a very low defect density as discussed above for alumina and chromia, the atomic species contribution to the diffusion potential is negligible and the diffusion process can be modeled by only accounting for the defect species alone (Swaminathan, Qu et al. 2007).

3.2.2 Fast diffusion paths in polycrystalline solids

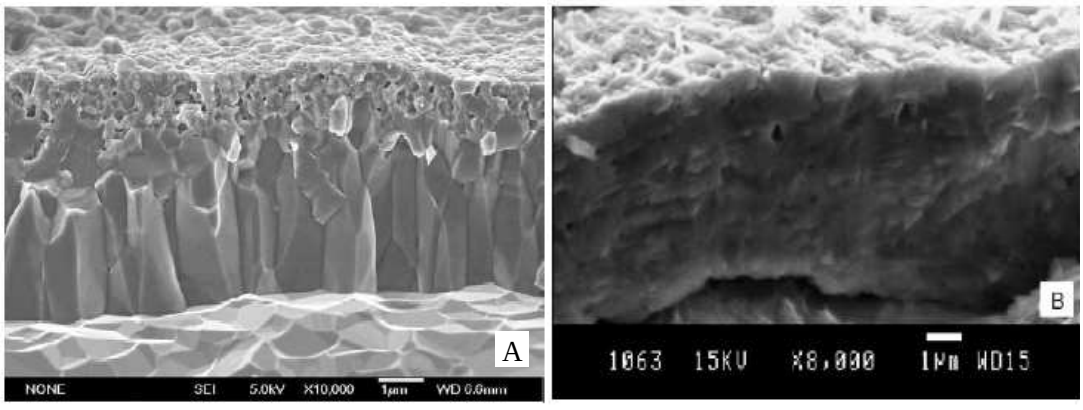

Figure 3.2: Cross-section SEMs of A) an alumina scale formed on a FeCrAlY alloy and B) a chromia scale grown on a FeCr substrate.

Alumina and chromia scales developing at high temperature on metallic alloys exhibit a polycrystalline nature, as shown on the micrographs provided in Figure 3.2 A) (Clarke 2002) and B) (Mikkelsen and Linderoth 2003). Therefore two diffusion paths exist through the oxide scale: grain bulks and grain boundaries, as illustrated in Figure 3.3. This is also the case for the metallic substrate which is most of the time a polycrystal. Furthermore, the metal/oxide interface also constitutes a specific diffusion path. While grain boundaries as well as the phase boundary occupy very low volume fractions, they present much higher diffusivities, such that their contribution can generally not be neglected (Tsai, Huntz et al. 1996).

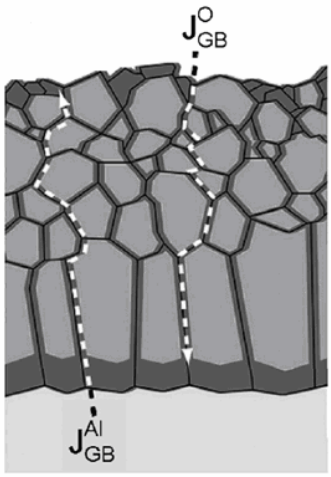

Figure 3.3: Illustration of fast diffusion paths formed by grain boundaries in an alumina scale.

The grain boundary contribution is classically included by considering a homogenized formulation for the diffusion through the material layer. Grain boundaries are introduced through their volume fraction (as a scalar if only one direction of diffusion is considered),

$$f_{gb} = k \frac{w_{gb}}{GS} \tag{3.5}$$

in which w_{gb} is the grain boundary width, GS is the average grain size (over the whole oxide scale or locally over an in-plane section if a variation of the parameter through the thickness is considered) and k is a coefficient related to the grains geometry, usually 2 (Naumenko, Gleeson et al. 2007) or 3 (Huntz 1999). Then the total flux through the oxide scale is obtained by considering two independent diffusion processes, one through a grain bulk and the other through a grain boundary, and operating a weighted sum of the contributions using the grain boundary volume fraction. An effective diffusivity can then be defined:

$$D_i^{eff} = \left(1 - f_{gb}\right) D_i^B + f_{gb} D_i^{gb} \tag{3.6}$$

where D_i^B and D_i^{gb} stand for the species i diffusivity within the grain bulks and the grain boundaries of the oxide material, respectively. The validity of such a formulation is only direct for one-dimensional models. It is justified here for a 2D model by the fact that no significant roughness of the oxide/metal phase boundary has been reported in direct relation with grain boundary locations, despite significant grain sizes with respect to the oxide scale thickness and the important difference in diffusivities between the two paths (Tsai, Huntz et al. 1996; Naumenko, Gleeson et al. 2007). This proves that in typical cases the fast diffusion along the interface operates a large redistribution of the incoming species flux along the boundary, resulting in a quite uniform oxide growth. Therefore such a homogenized formulation is employed for our phenomenological framework.

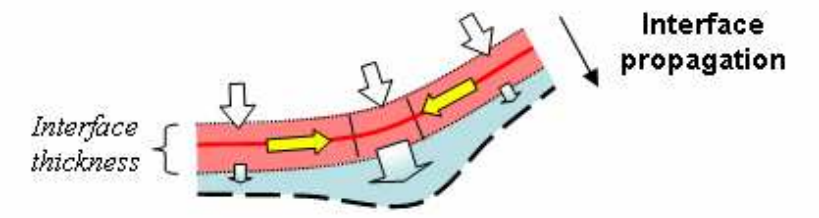

Figure 3.4: Interface diffusion model and illustration of a significant local variation in oxide phase propagation induced by large redistribution of the incoming oxygen flux along the phase boundary.

The fast diffusion along the metal/oxide boundary is of particular importance to our model, since it allows for a large redistribution of the incoming flux at the interface. Then in the situation of a stress-induced non-uniform vacancy concentration along the phase boundary, it may engender significant local variations in the oxide propagation, as depicted in Figure 3.4. The diffusion along the interface is included through a 1D path following the boundary between the metal and oxide phase's domains. In order to obtain the diffusion flow, the path is attributed a section, w_I , which stands for the phase boundary thickness, and a specific diffusivity, D_i^I , is applied:

$$J_i^I = -\frac{w_I D_i^I C_i}{R\theta} \nabla_I (\mu_i) \tag{3.7}$$

where J_i^I is the flux of species *i* along the interface (per unit thickness of the 2D domain) and ∇_I is the tangent gradient along the interface.

3.3 Mechanical framework

3.3.1 Growth strain development

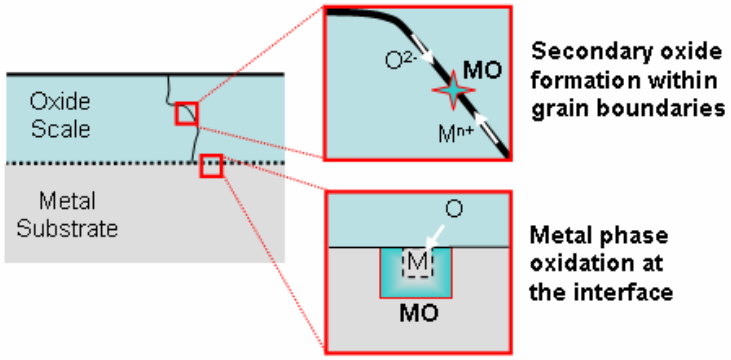

Figure 3.5: Schematic of considered growth strain generation mechanisms.

Two mechanisms of strain generation during isothermal oxide growth are considered. They have been chosen because they are most likely to induce high stresses at high temperature, possibly affecting the oxide scale development and contributing to its precipitated mechanical failure. The two mechanisms are a local volume change associated with the metal phase direct oxidation at the metal/oxide boundary, from the original theory of Pilling and Bedworth (Pilling and Bedworth 1923), and a local strain resulting from secondary oxide formation within oxide scale grain boundaries, following the concept initially introduced by Rhines and Wolf (Rhines and Wolf 1970). These two mechanisms are discussed in the review section on growth stresses. A schematic is provided in Figure 3.5.

The possibly large volume eigenstrain induced by direct alloy oxidation is likely to greatly influence local stress development at the metal/oxide boundary. Furthermore, it

induces a direct coupling between local stress situation and phase boundary propagation which might significantly affect local oxide phase developments. We consider here an effective measure of the volume ratio, denoted Π, possibly including additionally to the Pilling-Bedworth ratio other chemical contributions in volume change, as for instance from interdiffusion of species at the interface accompanying the oxidation reaction (Kang, Hutchinson et al. 2003; Suo, Kubair et al. 2003). As mentioned previously, the free energy released by the oxidation reaction is such that a strain accommodation work able to suppress the process would require a stress level about two orders of magnitude higher than typical yield or fracture stresses (Evans 1995). Consequently, the volume eigenstrain associated with metal phase oxidation is spontaneously accommodated as it develops. This generally results in the development of an anisotropic strain, exhibiting a main component in the direction of "easiest" expansion. Such a phenomenon has been identified in experiments in which the strain developed essentially along the global direction of free expansion, i.e. towards the free surface (Huntz, Calvarin Amiri et al. 2002). In this situation, the oxidation strain can simply be modeled as transversely isotropic with a main component on the surface normal vector:

$$\boldsymbol{\varepsilon}^{\Pi} = \begin{pmatrix} \varepsilon_t^{\Pi} & 0 & 0 \\ 0 & \varepsilon_n^{\Pi} & 0 \\ 0 & 0 & \varepsilon_t^{\Pi} \end{pmatrix} \tag{3.8}$$

where ε_n^{Π} represents the transformation eigenstrain in the direction normal to the interface (x_2 for instance here), and ε_t^{Π} the one in the tangential directions (x_1 and x_3). However, in a more general case and in order to better describe local developments at the interface, no arbitrary anisotropy should be enforced. Therefore we consider here the

development of an isotropic volume eigenstrain. The enforced true volumetric strain is:

$$\varepsilon_{vol}^{\Pi} = \frac{1}{3}\ln(\Pi) \tag{3.9}$$

It is simultaneously accommodated by elastic and plastic relaxation processes, which might result in an overall anisotropic development of the large eigenstrain.

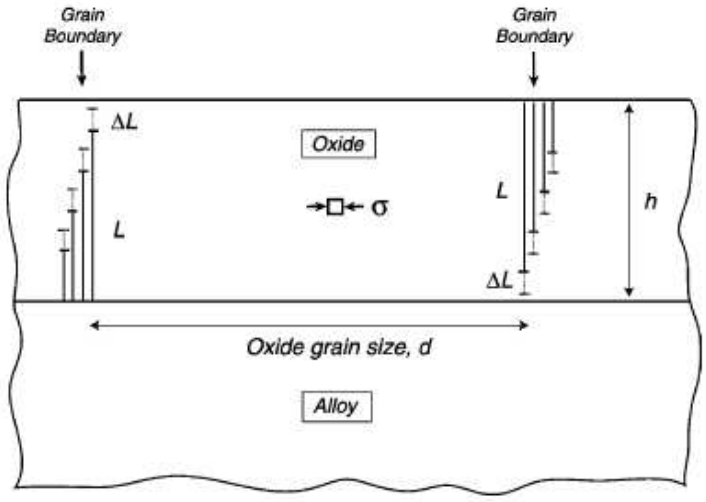

Figure 3.6: Schematic of Clarke's model describing in-plane growth strain development induced by the climb of edge dislocations along oxide scale grain boundaries.

The concept of a strain rate resulting from secondary oxide formation within oxide scale grain boundaries has gained considerable interest over the last decade, because it allows description of the development of a large in-plane strain with isothermal oxidation time, inducing in turn the raise of high stresses and/or large deformations in agreement with experimental observations. The most renowned model for the phenomenon (Balint and Hutchinson 2005; Jedlinski 2005; Zhu, Fleck et al. 2005; Busso and Qian 2006; Panicaud, Grosseau-Poussard et al. 2006; Hou, Paulikas et al. 2007) was developed by

Clarke (Clarke 2003). It describes the generation of a lateral growth strain, considering an in-plane homogenized one-dimensional domain. The underlying mechanism proposed is the climb of edge dislocations having a Burgers vector parallel to the oxide/alloy interface, in response to trapping of counter-diffusing cations and anions at the core of the dislocations. A schematic of the mechanism is provided in Figure 3.6 (Clarke 2003). In this model, it is assumed that only a negligible part of the diffusing ions are consumed in the process, so that it doesn't affect diffusion fluxes and the resulting main scale growth. Concurrent inward oxygen and outward cation diffusions along grain boundaries are required for this mechanism; however, the local oxide formation rate is assumed to be limited by the flux of the slowest diffusing species only. Following the development of Clarke, the local in-plane growth strain rate assuming a homogeneous oxide phase is formulated as:

$$\dot{\boldsymbol{\varepsilon}}^{gbox} = \begin{pmatrix} \dot{\varepsilon}^{gbox} & 0 & 0 \\ 0 & 0 & 0 \\ 0 & 0 & \dot{\varepsilon}^{gbox} \end{pmatrix}, \quad \text{with} \quad \dot{\varepsilon}^{gbox} = A_{gb}\, J_{\mathrm{O}}^{ox} \tag{3.10}$$

where J_{O}^{ox} is the flux of oxygen ions within the oxide scale and A_{gb} is a constant setting the amplitude of the growth strain development. This latter theoretically accounts for the volume fraction occupied by grain boundaries (it can be explicitly introduced as a proportionality constant), the density of edge dislocations along a grain boundary, the frequency of the slowest diffusing species trapping event, as well as geometric parameters relative to the development of an associated in-plane strain. In equation (3.10) the metallic substrate surface is considered to globally lay within the (x_1, x_3) plane, which then defines the global in-plane directions for the oxide scale.

3.3.2 Metal and oxide behaviors

In order to assess the stress influence on the oxidation process, it is essential to provide a mechanical framework as realistic as possible. A classical elasto-visco-plastic behavior is here employed for the mechanical response of each material. The model retained combines uncoupled linear elasticity, rate-independent plasticity and creep. Small elastic strains and isotropic behaviors are assumed and the rate of deformation is taken as a strain measure. Hook's law relates the true (Cauchy) stress tensor, σ, to the elastic (logarithmic) strain component, $\boldsymbol{\varepsilon}^{el}$, through the fourth-order elastic stiffness tensor, **C**:

$$\sigma = \mathbf{C}\ \boldsymbol{\varepsilon}^{el}\ . \tag{3.11}$$

A strain additive decomposition is then used:

$$\boldsymbol{\varepsilon} = \boldsymbol{\varepsilon}^{el} + \boldsymbol{\varepsilon}^{gr} + \boldsymbol{\varepsilon}^{pl} \tag{3.12}$$

in which $\boldsymbol{\varepsilon}^{gr}$ represents the growth strain and $\boldsymbol{\varepsilon}^{pl}$ stands for the plastic accommodation strain component. Incremental plasticity formulations are used, and both rate-independent plasticity and creep are modeled through the Mises stress potential and associated flow. The stress potential is then the equivalent deviatoric stress, $\tilde{\sigma}_d = \sqrt{\frac{3}{2}\sigma_d : \sigma_d}$, where $\sigma_d = \sigma - \frac{1}{3}\mathrm{tr}(\sigma)$ is the deviatoric stress tensor and **:** represents the double contraction operator ($\mathbf{A} : \mathbf{B} \equiv A_{ij}B_{ij}$). The resulting strain increment is:

$$\Delta\boldsymbol{\varepsilon}^{pl} = \frac{3}{2}\left(\dot{\tilde{\varepsilon}}^{cr}\Delta t + \tilde{\varepsilon}^{ri}\right)\frac{\sigma_d}{\tilde{\sigma}_d} \tag{3.13}$$

with $\dot{\tilde{\varepsilon}}^{cr}$ being the creep equivalent strain rate, Δt being the computation time increment and with $\tilde{\varepsilon}^{ri}$ being the minimum equivalent strain required to satisfy the plastic yield condition, $\tilde{\sigma}_d \leq \sigma^0$, where σ^0 is the equivalent (uniaxial) yield stress.

The creep relaxation of the studied oxides and metals follows a power law at high temperature (Huntz, Daghigh et al. 1998; Veal, Paulikas et al. 2007), which is usually expressed as:

$$\dot{\tilde{\varepsilon}}^{cr} = A_{cr} \exp\left(\frac{-Q_{cr}}{R\theta}\right)\sigma^{N_{cr}} \tag{3.14}$$

where Q_{cr} is the creep process activation energy and N_{cr} and A_{cr} are parameters, all dependent on material's composition and microstructure. Actually, a power law corresponds to an empirical description of the creep behavior, since mixed mechanisms are involved at the considered temperatures. A mass diffusion creep corresponds to $N_{cr} = 1$ and is characteristic to the behavior at very high temperatures, but at lower temperatures other mechanisms such as grain boundary sliding also take place. The relative contributions of the different involved processes then influence the effective exponent value. Creep relaxation is greatly influenced by the material grain size. While the dependency is known for processes based on bulk diffusion (Nabarro 1948; Herring 1950) and grain boundary diffusion (Coble 1963), it is not defined in a general case. A threshold stress is sometimes mentioned for the creep process to start (Kemdehoundja, Grosseau-Poussard et al. 2007). Such a parameter could be included by developing the stress term into $(\sigma - \sigma_t)^N \delta(\sigma - \sigma_t)$ with σ_t the threshold stress value and $\delta(x) = 0$ if $x < 1$, 1 if $x \geq 1$ (Hayhurst, Vakili-Tahami et al. 2003).

Finally, it is important to note that the plastic yield stress is high for the considered oxides, of the order of several hundreds megapascals to few gigapascals, but much lower for the metallic alloys at high temperature, typically around or below a hundred megapascals, thus allowing for large deformations of the substrate under limited stress levels.

3.4 Numerical implementation method

3.4.1 Overview of the situation

Implementation of a general numerical model for a sharp propagating phase boundary coupled with an evolving domain is very challenging. The solution can be determined by coupling two tasks: calculating the interface displacement following a given kinetics and solving for the continuous fields on each side of the discontinuity. Strong couplings appear when conservations and processes related to the interface propagation significantly influence the fields' evolutions and when the local propagation kinetics in turn depends on these affected values at the discontinuity. In this study aimed at investigating long-term high temperature oxidation, the interface displacement is gradual so that no fast morphological changes take place. However, the phase boundary propagation locally induces a large volume eigenstrain which considerably affects the strain and stress fields at the interface. In turn, this influences the local propagation kinetics. Furthermore, the oxidation kinetics is coupled with mass diffusion, including fast transport along the interface. The resolution challenge then comes from the multi-physics treatment of a discontinuity propagation coupled with its environment.

General problems of continuum mechanics are traditionally solved using the finite element method (FEM) in which a domain is modeled by a mesh that is locally refined to capture high spatial variations while keeping a smooth evolution over the elements. The definition and propagation of a sharp discontinuity in this environment are no longer straight-forward. This explains why most numerical predictions of complex phase boundary propagation / stress development couplings have been historically performed using two limited approaches. The first of these addresses simple interfacial geometries (linear, cylindrical or spherical) which are conserved in time, and allows for the use of a finite difference method over a grid evolving with the discontinuity motion (Johnson 1997; Oh 2006). The second approach addresses more complex geometries by employing FEM but limiting the analysis to a predefined interface propagation; this allows to design a mesh which remains adapted at all calculation time steps (Caliez, Feyel et al. 2002; Busso and Qian 2006). Specific numerical methods have been developed and are the subjects of extensive research for the treatment of phase boundary propagation within FEM, such as phase field (Kitashima 2008) or level set (Bloomfield, Richards et al. 2003).

However limitations remain on the allowed propagation kinetics formulations. In fact, either a continuous (diffuse) interface model must be considered, and then evolving field and phase data can be coupled at the element level, or an approximated sharp interface could be accounted for providing that its evolution does not depend on simulation fields (user-defined jumps can be used as driving force (Iwamoto, Cherkaoui et al. 2008)). Another limitation of these FEM-based methods concerns the inclusion of local processes, such as diffusion along the phase boundary in our model, which is not

possible if the local path is not defined within the mesh. An interface-adapted mesh would then be required at all times. Thus, the numerical treatment of the propagation of an evolving sharp interface dependent on field values in a continuum framework still constitutes a major challenge.

3.4.2 Description of the developed method

In order to implement the presented framework for oxide-metal phase boundary propagation at high temperature, a specific numerical tool has been developed allowing for the propagation of an evolving interface following a complex law dependent on field values. It is based on a classical FEM for the fields' resolution, performed sequentially with a specially developed external routine run in pre/post-calculations at each time step to calculate the phase boundary composition and propagation. It essentially couples the concept of phase field (Fix 1983) (diffuse interface of given width described by a field variable) for the smooth treatment of a moving sharp interface over a fixed mesh, and the front tracking method (Dafermos 1972) for the phase boundary propagation (the phase field evolution is assigned by the external routine from the mechanical and diffusion fields-dependent propagation kinetics, calculated at tracking points defining the interface). A semi-implicit time-integration scheme is employed to ensure simulation convergence and accuracy with sequentially evolving but highly coupled stress/diffusion and phase fields. It is based on a predictor/corrector method with a convergence criterion on the maximum local difference in driving force for the phase boundary propagation. A flowchart presenting the resolution scheme is provided in Figure 3.7. While the developed numerical framework requires a very fine mesh over the propagation zone (for

sharp interface model recovery) and is limited to gradual interface displacements (due to the sequential evolutions of the interface and the domain fields), it allows for the treatment of complex phase boundary composition and propagation evolutions dependent on discontinuous field values and coupled with specific interface processes such as fast mass diffusion and volume eigenstrain generation. It thus meets the specific and stringent requirements of the oxidation formulation.

The FEM computations have been performed using the commercial code ABAQUS, while specific programs developed under MATLAB have been used for the pre/post-calculations. Finally, input files writing and data extractions from ABAQUS have necessitated particular routines in PERL language. The overall simulation is ruled by a BASH code executed on a UNIX computation cluster. The finite element model and the interface resolution are detailed in the next sections.

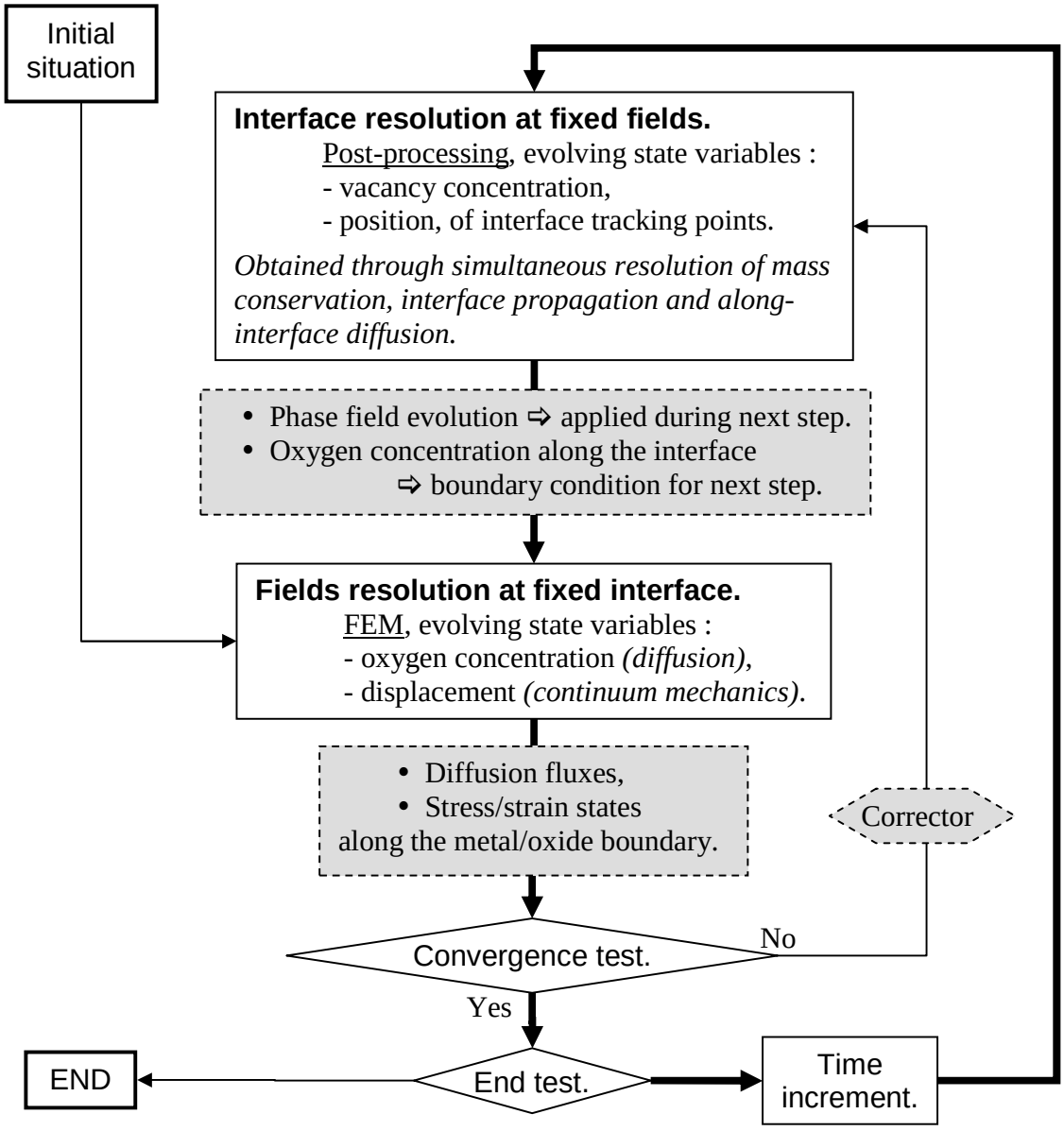

Figure 3.7: Flowchart of the resolution scheme.

3.5 Finite element model

The FEM computations have been performed using the commercial code ABAQUS. Each finite element simulation is based on a transient coupled stress/diffusion analysis, using the coupled temperature-displacement step of ABAQUS and the analogy between heat and mass diffusion. In fact, the temperature degree of freedom actually represents oxygen concentration. This analogy allows users to account for mass diffusion / displacement couplings, which are not allowed using the mass diffusion analysis step of ABAQUS. It presents of course some limitations. The main one is that an additional coupling with a temperature analysis is not possible. However, a uniform temperature variation over the domain can be performed through employing a user defined field, which is used to simulate the material system cooling from oxidation to room temperature. The uniform temperature approximation is reasonable considering that the focus is made on the very thin oxide scale and its surrounding. Note that for an accurate description of a thick thermal barrier coating, the temperature gradient that the layer is intended to experience should be accounted for. Another limitation of the use of the heat diffusion analogy is that mass density variations due to diffusion are not taken into account, only those associated with phase change are. Nevertheless, since the density of defects is assumed very low, this approximation is totally transparent here. The oxygen concentration at identified phase boundary nodes, resulting from pre-processing computations, is enforced as new boundary conditions for each simulation step. Since oxygen solubility is assumed to be negligible in the metallic substrate, a zero diffusivity is assigned on the metal side of the node-based phase boundary. If one would like to include diffusion within the metal phase, a second node-based phase boundary should be

identified to enforce concentrations on the metal side of the interface accounting for the field jump corresponding to the continuity of diffusion potential through the interface.

For the mechanical stress/strain fields, a diffuse interface is externally enforced. Its thickness should be limited to constitute a reasonable approximation of a sharp interface. It is here maintained on the order of 0.1µm through the use of a very fine mesh in the phase boundary propagation zone. Linear variations of the material mechanical properties are assumed through the interface thickness. Specific user subroutines have then been developed. In order to account for the phase transformation eigenstrain, other growth strains as well as thermal strains development, a UEXPAN subroutine has been written (this subroutine is initially intended to define complex thermal strains in the temperature analysis). The phase field evolutions computed externally are applied through a USDFLD which updates user-defined state variables as well as field variables used in material properties definition (material given by the phase field, and temperature). It also provides required local information for the UEXPAN subroutine, such as the local mass flux and initial and final phase field value over the step.

3.6 Interface resolution

The resolution of the phase boundary evolution is performed externally in pre-processing of the FEM analysis step. Coupled interface composition (vacancy concentration) and propagation (displacement with time) have to be resolved.

The phase boundary is defined by equidistant tracking points. In order to maintain the regular discretization despite large morphological evolutions, a redefinition of the points is performed after each propagation step. The number of points is kept constant for

simplicity, which is reasonable in the studied cases because the interface length does not vary dramatically over the simulation, but an adapted number recalculation could be easily added. The adapted number of points is defined essentially by two considerations. While it should be large enough to precisely describe the interface geometry, it set in the same time the minimum roughness that is accounted for, and should therefore be sufficiently high to eliminate perturbations at a scale lower the one of interest. Furthermore, the spatial resolution should be lower than that of the mesh. In fact, the stress and strain tensors, as well as the diffusion flux vector have to be extracted on each side of the diffuse interface layer for each tracking point in order to recover data corresponding to a model of sharp interface. This is performed by projection normal to the phase boundary at a distance corresponding to a half thickness of the diffuse layer, and then locally interpolating data from the FEM analysis, at elements surrounding the projected point. In order to smooth local perturbations, a local average over several elements is performed. Therefore, the spatial resolution of the phase boundary discretization should be sufficiently lower than that of the FEM analysis mesh. Furthermore, the distance between tracking points should be higher than half the diffuse layer thickness.

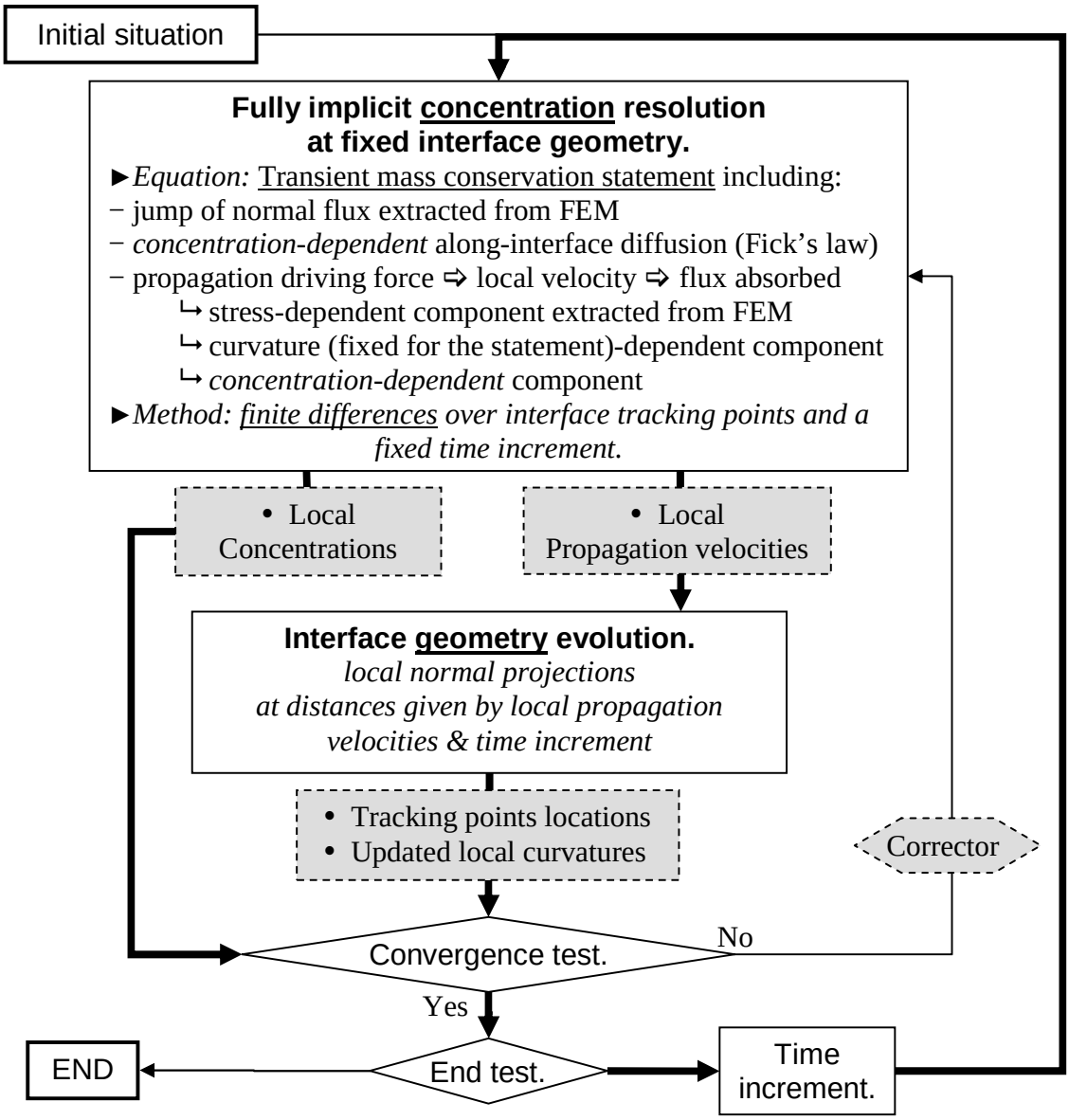

Figure 3.8: Flowchart of the interface resolution scheme.

Vacancy concentration and displacement at tracking points are resolved through the time integration of the system of equations formed by: the mass conservation statement, equation (2.25), phase boundary propagation, equations (2.54) and (2.53), and along-interface diffusion, equation (3.7). The resolution scheme is presented in Figure 3.8. The

algorithm developed for the time integration combines partial fully implicit resolution with a predictor-corrector scheme with adaptive time increment setting. A direct implicit resolution of the time integrated mass balance statement is performed providing concentrations and diffusion fluxes at a given time for a fixed geometry (and fixed sharp interface data extracted from the FEM analysis). The phase boundary propagation is then obtained from the mass consumed in the process. This sequence is included in a predictor-corrector scheme in order to solve for the coupling with geometry which is formed through the curvature term in the propagation driving force. The algorithm is stopped once a maximum allowed total time increment has been reached, or before if limiting criteria controlling the maximum allowed oxide scale thickness increase or the maximum allowed curvature evolution before stress/strain and diffusion fields' recomputation are fulfilled.

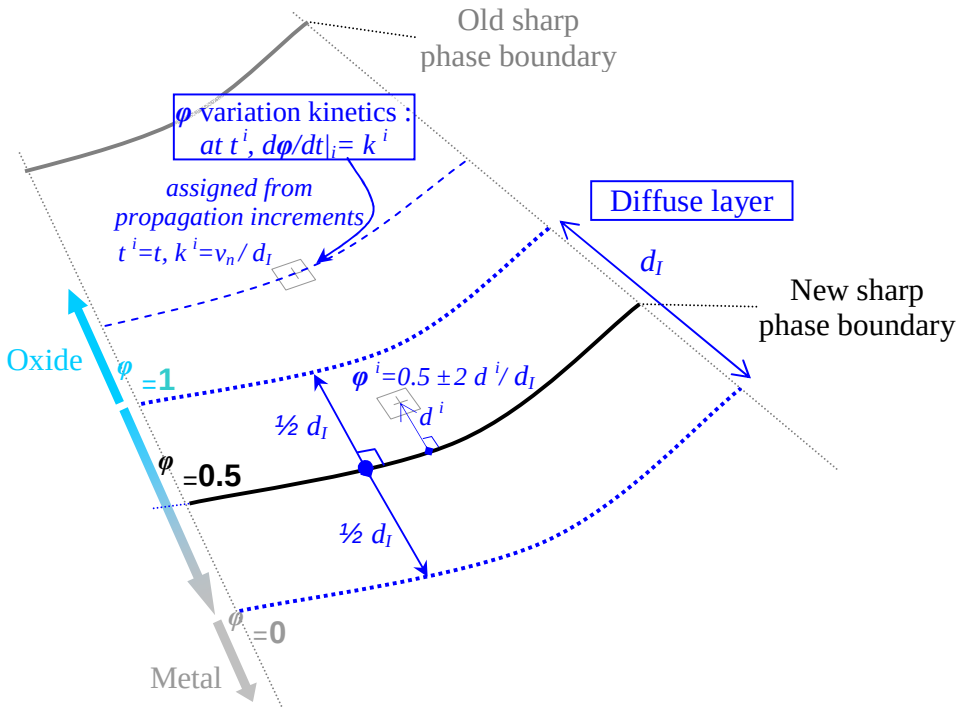

Figure 3.9: Schematic of the phase field definition.

Finally, data for the next FEM analysis are built. They essentially include the evolution of the phase field, which defines the local material properties. An updated value, φ^{i}, is defined for each element of the FEM mesh from the new position of the phase boundary, as shown in Figure 3.9. For elements lying within the diffuse layer, a scaling of the normal distance to the phase boundary line allows building a field evolving linearly over the finite thickness, as defined in the figure. The updated field is not directly enforced, but will result from a progressive time-dependent variation in order to ensure a smooth phase transformation, as defined in Figure 3.9. Times for the onset of the local phase field evolution as well as the corresponding transformation kinetics are constructed based on phase boundary propagation increments. The non-deformed configuration is considered for the interface tracking. This approximation is here required for the continuous evolution over steps of the phase field mapping. The only significant induced limitation concerns the true phase boundary curvature. It is therefore a reasonable approximation only for limited non-uniform mechanical deformations. A node-based interface is defined through identification of a path formed by FEM mesh nodes following the true phase boundary. It is used to enforce the oxygen concentration boundary conditions for the next diffusion analysis, interpolated from the values computed at the interface tracking points. The local material diffusivity only depends on the element location with respect to the node-based interface (metal or oxide side). Mechanical properties vary linearly, as defined by the phase field, from the untransformed to the transformed materials values. Therefore the interface is only diffuse for the mechanical fields' resolution. Specific programs developed under MATLAB have been written for all these pre/post-FEM calculations.

3.7 Setting and test of the simulation tool

In order to assess the simulation tool capacity and accuracy, a few tests have been performed providing necessary settings. The first test assesses the capacity to recover a parabolic kinetics for one-dimensional oxide growth. In order to set up the simulation, the conditions allowing for a parabolic growth rate with the developed model are previously investigated, and a procedure is defined for the setting of kinetics parameters. Then and in order to assess the oxide propagation time integration scheme, a simulation is run and the oxide growth kinetics is compared with the analytical expression. In a second test, a simplified case is simulated to assess the description of a stress influence on propagation kinetics.

3.7.1 Conditions for parabolic oxide growth

The classic parabolic rate for one-dimensional oxide growth, representative of a through-scale quasi-steady state diffusion control with constant compositions at the interfaces, is described through a mass balance statement at the propagating phase boundary (equation (2.24)), assuming a negligible oxygen solubility in the metal substrate ($\mathbf{J}_{\mathrm{O}}^{+} \cdot \mathbf{n} = 0$, $C_{\mathrm{O}}^{+}=0$) and no volume change associated with metal oxidation ($\Pi_I = 1$):

$$v_n = \frac{\left| \mathbf{J}_{\mathrm{O}}^{-} \cdot \mathbf{n} \right|}{C_{\mathrm{O}}^{-}} \quad . \tag{3.15}$$

Let us now analyze under which conditions a parabolic rate would be recovered with the developed model. In the case of no stress, no curvature (flat oxide scale), negligible

oxygen solubility in the metal substrate and no volume change associated with metal oxidation, the phase boundary propagation velocity is from equation (2.53):

$$v_n = M_I \left(f_I^0 - \left(\mu_{\mathrm{V}}^- - \mu_{\mathrm{V}}^{0-} \right) C_{\mathrm{O}}^- \right). \tag{3.16}$$

It is dependent on the interface vacancy concentration, which is a relaxed variable compared to the classical formulation. Equating the two expressions yields:

$$\mu_{\mathrm{V}}^- - \mu_{\mathrm{V}}^{0-} = \frac{1}{C_{\mathrm{O}}^-} \left(f_I^0 - \frac{\left| \mathbf{J}_{\mathrm{O}}^- \cdot \mathbf{n} \right|}{M_I C_{\mathrm{O}}^-} \right) \tag{3.17}$$

The parabolic rate is obtained assuming a constant interface composition, such that only the increase in oxide scale thickness affects the incoming oxygen flux. This situation is recovered here if the deviation in vacancy chemical potential is negligible at any time:

$$\left| \frac{\mu_{\mathrm{V}}^- - \mu_{\mathrm{V}}^{0-}}{\mu_{\mathrm{V}}^{0-}} \right| \ll 1 \quad \text{at any } t\,. \tag{3.18}$$

Since all terms in equation (3.17) are fixed parameters except the incoming oxygen flux at the interface, $\left| \mathbf{J}_{\mathrm{O}}^- \cdot \mathbf{n} \right|$, which is necessarily evolving with time (due to oxide growth), the previous inequality provides two conditions for parabolic oxidation kinetics:

$$\frac{1}{M_I} \frac{\left| \mathbf{J}_{\mathrm{O}}^- \cdot \mathbf{n} \right|}{\mu_{\mathrm{V}}^{0-} \left(C_{\mathrm{O}}^- \right)^2} \ll 1 \tag{3.19}$$

and

$$\frac{f_I^0}{\mu_{\mathrm{V}}^{0-} C_{\mathrm{O}}^-} \ll 1 \tag{3.20}$$

The second inequality provides a maximum bound for the value of f_I^0 in order to achieve a parabolic rate. The quasi-steady state incoming oxygen flux at the interface can be easily expressed for a one-dimensional problem through Fick's first law, yielding:

$$\left| \mathbf{J}_{\mathrm{O}}^- \cdot \mathbf{n} \right| = D_{\mathrm{O}}^{ox} \frac{C_{\mathrm{O}}^{II} - C_{\mathrm{O}}^-}{\xi} \tag{3.21}$$

where D_{O}^{ox} is the oxygen diffusivity through the oxide scale, C_{O}^{II} is the oxygen concentration at the outer interface and ξ denotes the oxide scale thickness. Assuming a negligible vacancy concentration at the outer surface, the difference in composition through the oxide scale is equal to the vacancy molar density at the interface:

$$C_{\mathrm{O}}^{II} - C_{\mathrm{O}}^- = C_{\mathrm{V}}^- \tag{3.22}$$

Therefore the first condition, equation (3.19), can be rewritten as:

$$\frac{C_{\mathrm{V}}^-}{C_{\mathrm{O}}^-} \ll \xi \frac{M_I C_{\mathrm{O}}^- \mu_{\mathrm{V}}^{0-}}{D_{\mathrm{O}}^{ox}}. \tag{3.23}$$

Since the oxide scale is growing, $\xi \geq \xi_{t=0}$ at any time. Furthermore it also implies that the oxygen flux decreases with time, see equation (3.21). Therefore the difference in vacancy chemical potential must increase with time from equation (3.17), which means that $\mu_{\mathrm{V}}^- \geq \mu_{\mathrm{V}}^{0-}$ at any time. Since the chemical potential is by essence an increasing function of the concentration, this is also true for the corresponding vacancy concentration:

$C_{\mathrm{V}}^{-} \geq C_{\mathrm{V}}^{0-}$. But if the condition (3.23) is fulfilled (along with (3.20)), then the variation remains very small. Therefore it can be assumed that inequality (3.23) is satisfied at all times if:

$$\frac{C_{\mathrm{V}}^{0-}}{C_{\mathrm{O}}^{-}} \ll \xi_{t=0} \frac{M_I C_{\mathrm{O}}^{-} \mu_{\mathrm{V}}^{0-}}{D_{\mathrm{O}}^{ox}}. \tag{3.24}$$

This relation gives a condition (maximum bound) on the equilibrium vacancy concentration at the metal/oxide interface in the reference, flat stress-free situation: C_{V}^{0-}. This parameter actually appears twice in the above equation, since the chemical potential is dependent on the concentration. It is worth noticing that the condition of a maximum bound provided by equation (3.24) at least qualitatively agrees with experimental observations of a very low composition defect density within the chromia and alumina oxides, for which parabolic growth rate are commonly observed (Birks, Meier et al. 2006).

3.7.2 Setting of oxidation kinetics parameters

The one-dimensional stress-free oxide scale growth kinetics, as described by the model in the case of a negligible oxygen solubility within the substrate, depends on four parameters: the effective oxide scale oxygen diffusivity, D_{O}^{ox}, the initial relative vacancy concentration at the phase boundary, $\delta_{\mathrm{V}}^{0} = C_{\mathrm{V}}^{-} / C_{\mathrm{O}}^{-}$, the initial driving force for the interface propagation, f_I^0, as well as the interface mobility, M_I. Actually only three parameters need to be defined. In fact, the product of the two last values sets the initial metal/oxide boundary propagation velocity, $v_n(t_0) = M_I f_I^0$. Since on the other hand it is

assumed that the oxide growth is driven by diffusion of oxygen ions through the oxide scale, the mass balance must be achieved at the phase boundary, equation (2.24). Practically, the mass rate per unit surface consumed in the oxidation reaction must match the incoming diffusion flux. This quasi-equilibrium (since incoming diffusion flux decreases with oxide scale growth) should be achieved in the considered initial situation, which yields:

$$M_I f_I^0 = \frac{\left[\mathbf{J}_\mathrm{O} \cdot \mathbf{n}\right]}{C_\mathrm{O}^+ - \Pi_I C_\mathrm{O}^-} \quad \text{at} \quad t = t_0 . \tag{3.25}$$

Assuming a negligible vacancy concentration at the outer oxide interface (in front of that at the inner interface), the incoming flux in the initial situation is given by:

$$\left[\mathbf{J}_\mathrm{O}^- \cdot \mathbf{n}\right] = D_\mathrm{O}^{ox} \frac{\delta_\mathrm{V}^0}{\xi_0} . \tag{3.26}$$

Combining both equations yields:

$$M_I f_I^0 = \frac{D_\mathrm{O}^{ox} \delta_\mathrm{V}^0}{\xi_0 \left(C_\mathrm{O}^+ - \Pi_I C_\mathrm{O}^-\right)} \tag{3.27}$$

Thus the four parameters are coupled and one can be eliminated.

Data for the effective oxide scale oxygen diffusivity, D_O^{ox}, can be directly found in the literature or easily built based on equation (3.6). The initial relative vacancy concentration at the phase boundary, δ_V^0, is not readily available, although it is known that it should be small in front of unity (Birks, Meier et al. 2006). It is here set to adjust the oxide growth magnitude at the end of the isothermal oxidation simulation time in

order to fit experimental data. No bibliographic or experimental data have been found in the literature for the initial driving force for the interface propagation, f_I^0, or for the interface mobility, M_I. Therefore f_I^0 is set from physical considerations, possibly including the shape of experimental oxidation kinetics curves (see following discussion and investigation cases in the next chapter), and M_I is eventually calculated through equation (3.27).

Under the initial assumptions made here, particularly constant oxide diffusivity and negligible solubility in the metal substrate, it would not be possible to describe a subparabolic oxide growth. However, several different situations might lead to such kinetics and could be described with the developed simulation tool. Among them, oxide grain coarsening resulting in a reduction in grain boundaries volume fraction and a consequent decrease of the effective through-scale diffusivity (Huntz 1999; Naumenko, Gleeson et al. 2007); non-zero oxygen solubility in the metal substrate and subsequent increase with time of the oxygen concentration at the oxide/metal interface, leading to a reduced through-scale composition gradient and thus a slower diffusion kinetics; or a thermodynamic effect associated with a high in-plane compressive stress field within the oxide scale as proposed by Evans (Evans 1995) and described in Chapter 2. Reverse situations would naturally result in kinetics more linear than in the parabolic growth case. However, it can be noticed that from the developed model such kinetics are directly obtained if the condition provided by equation (3.20) is not fulfilled. In the extreme opposite case, $f_I^0 \gg \mu_{\mathrm{V}}^{0-} C_{\mathrm{O}}^{-}$, a linear kinetics would be obtained since the phase boundary propagation kinetics would simply be constant.

3.7.3 Propagation time-integration accuracy

The accuracy of the global time integration scheme, including time increment setting and domain discretization, has been checked through comparison with the analytical expression for a one-dimensional parabolic oxide scale growth. The oxide phase propagation is controlled by the inward transport of oxygen. Coupling mass conservation at the interface with Fick's law, and considering a one dimensional quasi-steady-state problem with constant values for concentration at the interfaces and no oxygen diffusing in the substrate, an analytical expression can be derived for the scale thickness evolution with time:

$$\xi = \sqrt{k_p (t - t_0) + \xi_0^2} \quad , \quad \text{with} \quad k_p = 2 D_{\mathrm{O}}^{ox} \frac{C_{\mathrm{O}}^{II} - C_{\mathrm{O}}^{-}}{C_{\mathrm{O}}^{-}} \tag{3.28}$$

where ξ designates the oxide scale thickness and ξ_0 its value at the initial time t_0. D_{O}^{ox} refers to the oxygen diffusivity in the oxide scale, assumed constant, and C_{O}^{-} and C_{O}^{II} stand for the boundary concentrations of oxygen at the oxide inner and outer interfaces, respectively. An initial small thickness has been considered for comparison with the simulation, in order to avoid dealing with initial phase nucleation. Model parameters are defined following the assumptions and the procedure defined in the previous section, as well as the two conditions derived for parabolic oxidation kinetics, equations (3.20) and (3.24). The parameters used for the simulation test, along with the finite element mesh refinement in the oxidation direction, are identical to those given in the investigation case on a thermal barrier coating presented in the next chapter. The mesh is laterally composed of five identical rows of rectangular elements of width arbitrarily set to unity.

An isothermal oxidation simulation is performed over 335 hours. The kinetics of the oxide scale growth resulting from the simulation is plotted along with the analytical description, equation (3.28), in Figure 3.10. The simulation points perfectly match the analytical law, which validates the procedure of parameters setting and the long-term accuracy of the implemented numerical scheme for phase boundary propagation.

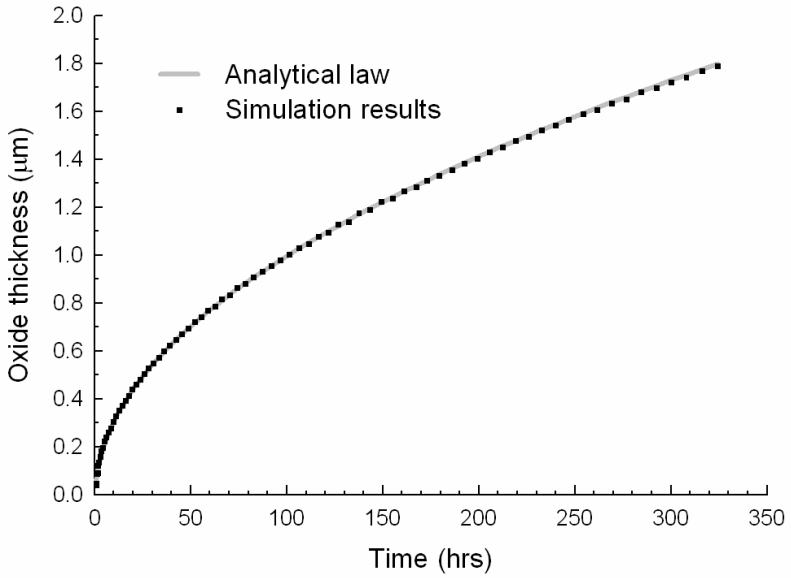

Figure 3.10: Kinetics of oxide scale thickness growth. Simulation results and comparison with the analytical law for a 1D parabolic oxidation kinetics.

3.7.4 Test of stress influence

A second test simulation has been performed to assess the description of a stress influence on the oxidation kinetics. This simulation presents isothermal oxidation at 1100°C in a thermal barrier coating case and uses the parameters of the previous test. However, now an initially convoluted oxide scale is considered and a transversely

isotropic phase transformation strain is applied in association with metal oxidation (Busso and Qian 2006):

$$\boldsymbol{\varepsilon}^{\Pi} = \begin{pmatrix} \varepsilon_t^{\Pi} & 0 & 0 \\ 0 & \varepsilon_n^{\Pi} & 0 \\ 0 & 0 & \varepsilon_t^{\Pi} \end{pmatrix}, \quad \text{with } \varepsilon_n^{\Pi} = 0.241 \quad \text{and} \quad \varepsilon_t^{\Pi} = 0.277 \times 10^{-2} \tag{3.29}$$

where ε_n^{Π} represents the transformation eigenstrain in the direction normal to the interface and ε_t^{Π} the one in the transverse directions. The materials have been assumed perfectly elastic and interface diffusion is not accounted for.

The influence of the local stress/strain state at the interface on the oxidation kinetics is shown in Figure 3.11, which provides the scale thickness growth history at different abscises of the system, identified in Figure 12. The analytical solution obtained for a stress-free flat interface under similar conditions as well as the experimental kinetics are also given for comparison. It can be seen that the kinetics are differently modified depending on the localization, whether peak (B,D) or valley regions (A, C, E), and that the extent of the influence is important, about ±20% in scale thickness. Peak regions exhibit a lower sub-parabolic rate while valleys grow at a faster rate than the one predicted by the analytical calculation. It is interesting to notice that the kinetics shape of the valley regions approaches the experimental measurements (Busso and Qian 2006), even if the comparison is limited by the fact that only internal growth has been modeled here and at isothermal conditions. Nevertheless these results show that observed deviations from the classical parabolic rate (sub-parabolic in (Busso, Lin et al. 2001), hyper-parabolic in (Busso and Qian 2006)) could be explained by the stress and strain discontinuities developing at the propagating interface.

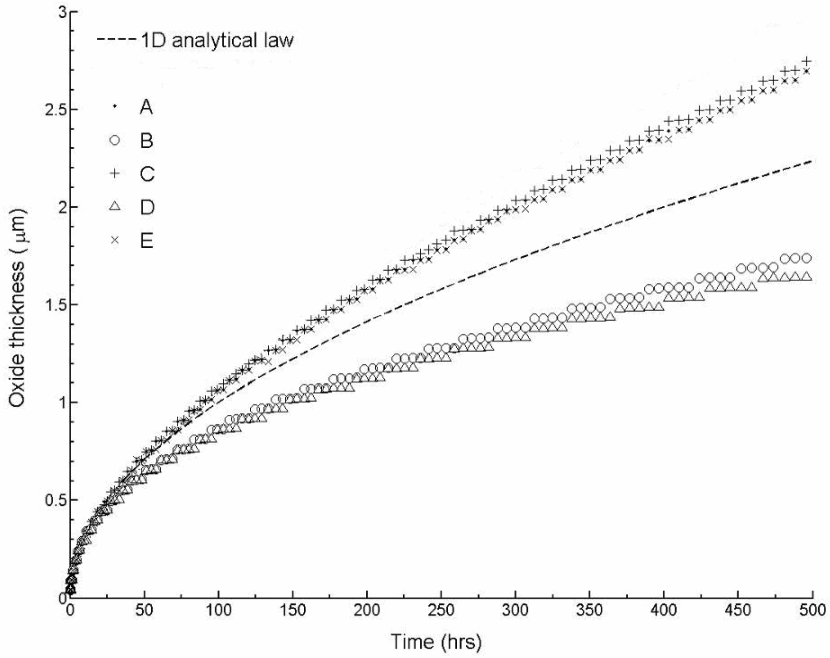

Figure 3.11: TGO growth kinetics at different abscises (identified in Figure 3.12).

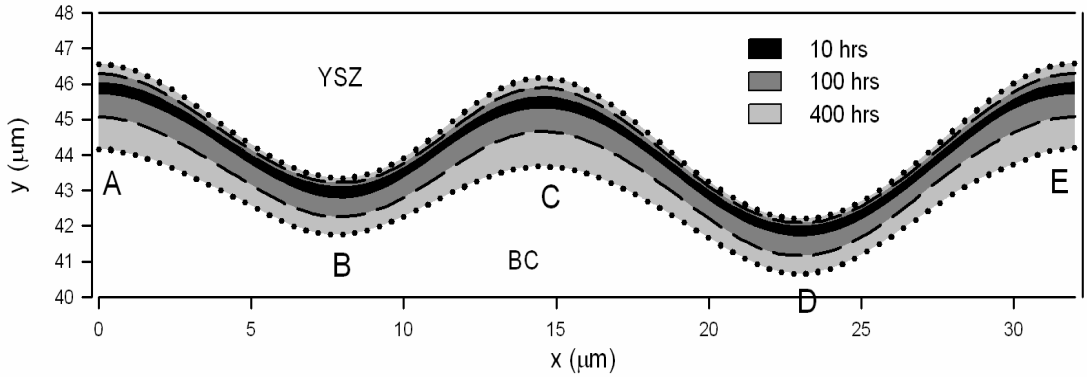

Figure 3.12: Oxide scale interfaces after 10(—), 100(– –) and 400(•) hours of isothermal oxidation at 1100°C.

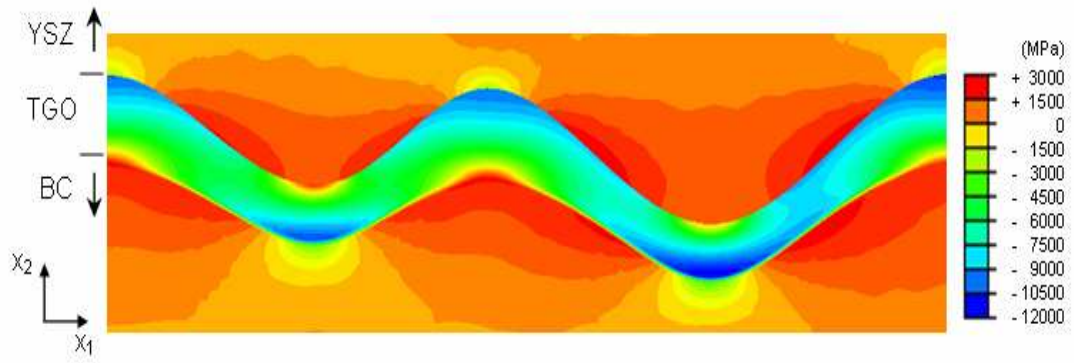

Figure 3.13: Contour plot of the lateral stress component, σ_{11}, after 400 hrs of isothermal oxidation at 1100°C.

Stress discontinuities at the metal/oxide boundary can be clearly identified in Figure 3.13, showing a contour plot of the lateral stress component after 400 hours of oxidation. In-plane (lateral) compressive stresses are dominant in the oxide scale due to the constrained volume expansion induced by the phase transformation. It can be seen that in peak regions, very high compressive stresses have developed on the oxide side of the interface, while on the bond coat side the material is less constrained. This situation induces a negative balance of mechanical elastic energy during interface propagation, which results in a decrease of the oxidation rate. Conversely, tensile stresses develop in the valley regions due to a global bending effect, and increase the local oxide growth kinetics. The outcome of these opposed situations is that the oxide layer grows faster in valleys than on peaks, while the TGO/BC interface tends to flatten with time, as shown in Figure 3.12.

These results are limited by the fact that the stress levels reached in this simulation largely overpass the typical oxide yield stress (Karlsson and Evans 2001), owing to the large phase transformation eigenstrain. Adequate relaxation processes in the different materials have to be included for realistic simulations. However, these results

demonstrate the capacity of the simulation tool to describe coupled effects of stress-affected local interface propagation and stress developments. The coupling leads to a modification of the global and local growth of the oxide layer, a phenomenon which could be amplified by fast interface diffusion (Panat, Hsia et al. 2005). It affects not only the oxide scale average thickness, but also its morphology and the interface geometry. In turn, this would have a significant influence on the stress development and localization upon cooling of the system at room temperature, and thus could play a key role in crack ignition and the eventually resulting bond coat spallation. Realistic and detailed case investigations are performed in the next chapter.

3.8 References

Atkinson, A. (1985). "Transport processes during the growth of oxide films at elevated temperature." Reviews of Modern Physics **57**(2): 437.

Balint, D. S. and J. W. Hutchinson (2005). "An analytical model of rumpling in thermal barrier coatings." Journal of the Mechanics and Physics of Solids **53**(4): 949-973.

Birks, N., G. H. Meier and F. S. Pettit (2006). Introduction to the high-temperature oxidation of metals. New York, Cambridge University Press.

Bloomfield, M. O., D. F. Richards and T. S. Cale (2003). "A computational framework for modelling grain-structure evolution in three dimensions." Philosophical Magazine **83**(31-34): 3549-3568.

Busso, E. P., J. Lin, S. Sakurai and M. Nakayama (2001). "A mechanistic study of oxidation-induced degradation in a plasma-sprayed thermal barrier coating. Part i: Model formulation." Acta Materialia **49**: 1515-1528.

Busso, E. P. and Z. Q. Qian (2006). "A mechanistic study of microcracking in transversely isotropic ceramic-metal systems." Acta Materialia **54**: 3325-338.

Caliez, M., F. Feyel, S. Kruch and J. L. Chaboche (2002). "Oxidation induced stress fields in an eb-pvd thermal barrier coating." Surface & Coatings Technology **157**(2-3): 103-110.

Clarke, D. R. (2002). "Stress generation during high-temperature oxidation of metallic alloys." Current Opinion in Solid State and Materials Science **6**(3): 237.

Clarke, D. R. (2003). "The lateral growth strain accompanying the formation of a thermally grown oxide." Acta Materialia **51**: 1393-1407.

Coble, R. L. (1963). "A model for boundary diffusion controlled creep in polycrystalline materials." Journal of Applied Physics **34**(6): 1679.

Dafermos, C. M. (1972). "Polygonal approximations of solutions of initial value-problem for a conservation law." Journal of Mathematical Analysis and Applications **38**(1): 33-&.

Evans, H. E. (1995). "Stress effects in high-temperature oxidation of metals." International Materials Reviews **40**(1): 1-40.

Fix, G. J. (1983). Free boundary problems: Theory and applications. Boston, Pitman.

Hayhurst, D. R., F. Vakili-Tahami and J. Q. Zhou (2003). "Constitutive equations for time independent plasticity and creep of 316 stainless steel at 550 degrees c." International Journal of Pressure Vessels and Piping **80**(2): 97-109.

Herring, C. (1950). "Diffusional viscosity of a polycrystalline solid." Journal of Applied Physics **21**(5): 437-445.

Hou, P. Y., A. P. Paulikas, B. W. Veal and J. L. Smialek (2007). "Thermally grown al2o3 on a h-2-annealed fe3al alloy: Stress evolution and film adhesion." Acta Materialia **55**(16): 5601-5613.

Huntz, A. M. (1999). "Parabolic laws during high temperature oxidation: Relations with the grain size and thickness of the oxide." Journal of Materials Science Letters **18**: 1981-1984.

Huntz, A. M., G. Calvarin Amiri, H. E. Evans and G. Cailletaud (2002). "Comparison of oxidation-growth stresses in nio film measured by deflection and calculated using creep analysis or finite-element modeling." Oxidation of Metals **57**(5-6): 499-521.

Huntz, A. M., S. Daghigh, A. Piant and J. L. Lebrun (1998). "Evidence of stress relaxation in thermally grown oxide layers - experiments and modelling." Materials Science and Engineering **A248**: 44-55.

Iwamoto, T., M. Cherkaoui and E. P. Busso (2008). "A finite element-based level-set method of an interface motion driven by a diffusion field: Application to a phase transformation problem." Computational Materials Science **44**(2): 792-801.

Jedlinski, J. (2005). Defect-diffusion-stress relationships in modeling the oxidation and degradation processes of alumina formers: A brief survey. Diffusion in materials: Dimat 2004, pt 1and 2. **237-240:** 911-921.

Johnson, W. C. (1997). "Effect of elastic stress on two-phase binary diffusion couples." Metallurgical and Materials Transactions a-Physical Metallurgy and Materials Science **28**(1): 27-38.

Kang, K. J., J. W. Hutchinson and A. G. Evans (2003). "Measurement of the strains induced upon thermal oxidation of an alumina-forming alloy." Acta Materialia **51**(5): 1283-1291.

Karlsson, A. M. and G. Evans (2001). "A numerical model for the cyclic instability of thermally grown oxides in thermal barrier systems." Acta Materialia **49**(10): 1793-1804.

Kemdehoundja, M., J. L. Grosseau-Poussard, J. F. Dinhut and B. Panicaud (2007). "Growth stresses in alpha-cr2o3 thermal oxide films determined by in situ high temperature raman spectroscopy." Journal of Applied Physics **102**(9).

Kitashima, T. (2008). "Coupling of the phase-field and calphad methods for predicting multicomponent, solid-state phase transformations." Philosophical Magazine **88**(11): 1615-1637.

Lankhorst, M. H. R., H. J. M. Bouwmeester and H. Verweij (1997). "Thermodynamics and transport of ionic and electronic defects in crystalline oxides." Journal of the American Ceramic Society **80**(9): 2175-2198.

Mikkelsen, L. and S. Linderoth (2003). "High temperature oxidation of fe-cr alloy in o_2-h_2-h_2o atmospheres; microstructure and kinetics." Materials Science and Engineering **A361**: 198-212.

Nabarro, F. R. N. (1948). "Deformation of crystals by the motion of single ions." Report of a Conference on Strength of Solids, Bristol: 75-90.

Naumenko, D., B. Gleeson, E. Wessel, L. Singheiser and W. J. Quadakkers (2007). "Correlation between the microstructure, growth mechanism, and growth kinetics of alumina scales on a fecraly alloy." Metallurgical and Materials Transactions a-Physical Metallurgy and Materials Science **38A**: 2974-2983.

Oh, E. S. (2006). "A diffusional analysis for the oxidation on a plane metal-oxide interface." Chemical Engineering Journal **117**(2): 143-154.

Panat, R., K. J. Hsia and D. G. Cahill (2005). "Evolution of surface waviness in thin films via volume and surface diffusion." Journal of Applied Physics **97**(1).

Panicaud, B., J. L. Grosseau-Poussard and J. F. Dinhut (2006). "On the growth strain origin and stress evolution prediction during oxidation of metals." Applied Surface Science **252**(16): 5700-5713.

Pilling, N. B. and R. E. Bedworth (1923). "The oxidation of metals at high temperatures." Journal of the Institute of Metals **29**: 529-582.

Rhines, F. N. and J. S. Wolf (1970). "The role of oxide microstructure and growth stresses in the high-temperature scaling of nickel." Metal. Trans. **1**: 1701-1710.

Suo, Z., D. V. Kubair, A. G. Evans, D. R. Clarke and V. K. Tolpygo (2003). "Stresses induced in alloys by selective oxidation." Acta Materialia **51**: 959-974.

Swaminathan, N., J. Qu and Y. Sun (2007). "An electrochemomechanical theory of defects in ionic solids. I. Theory." Philosophical Magazine **87**(11): 1705-1721.

Tsai, S. C., A. M. Huntz and C. Dolin (1996). "Growth mechanism of cr_2o_3 scales: Oxygen and chromium diffusion, oxidation kinetics and effect of yttrium." Materials Science and Engineering **A212**: 6-13.

Veal, B. W., A. P. Paulikas and P. Y. Hou (2007). "Creep in protective alpha-al2o3 thermally grown on beta-nial." Applied Physics Letters **90**(12): 3.

Zhu, H. X., N. A. Fleck, A. C. F. Cocks and A. G. Evans (2005). "Numerical simulations of crack formation from pegs in thermal barrier systems with nicocraly bond coats." Materials Science and Engineering A-Structural Materials Properties Microstructure and Processing **A404**(1-2): 26-32.

CHAPTER 4

INVESTIGATIONS OF STRESS-AFFECTED OXIDATION

4.1 Introduction

Finally, two practical cases are investigated concerning an uncoated chromia forming ferritic steel for SOFC interconnect, and a nickel-aluminum alloy coated with an EB-PVD (electron-beam physical vapor deposition) yttria stabilized zirconia layer forming a thermal barrier coating. The associated situations present many similarities, but they interestingly differ, since in the first one a chromia layer is developed from a flat surface at moderate temperature (~800°C) while in the second one an alumina scale forms at a convoluted interface at higher temperature (~1100°C).

In each case, a mechanism of stress-induced morphological development is studied. The main processes and influences are analyzed allowing for the identification of key physical properties. In a second time, the likely influence of the non-uniform morphological development on mechanical failure is investigated, during isothermal oxidation and upon cooling to room temperature. Finally, the influences of material-related parameters are tested providing optimization tracks for the design of metallic alloys which should allow improving the mechanical lifetime of the studied system.

Eventually, the assessment of the stress-affected oxidation mechanism and its main influences is discussed, along with the provided guidelines concerning material properties and the possible influence of additives, particularly reactive elements.

4.2 Investigation on a SOFC interconnect case

4.2.1 Introduction

Oxidation resistant metallic alloys are increasingly employed for interconnects in solid oxide fuel cells (SOFC) operating at moderately high temperatures (600 to 900°C), because they have lower fabrication cost and better formability than the traditionally used ceramic compounds. At the surfaces exposed directly or indirectly to the oxygen-containing atmosphere, the metal phase oxidizes and an oxide scale develops. The principle of oxidation-resistant metallic alloys is that their composition is designed so as to produce a protective oxide scale, typically constituted of chromia, owing to its good electrical conductivity. This oxide scale is designed to exhibit very low permeability to the oxidation reactants, thus limiting as it grows the further extent of the process. The physical integrity of the oxide scale is therefore essential to the long term reliability of the metallic component.

However, stress development and resulting phenomena, such as deformation and crack nucleation, often limits the lifetime of thermally grown oxide scales, leading to its spallation and failure after a few hundred hours (Hou, Paulikas et al. 2007). Intensive research has been performed over the last decades to facilitate the design of metallic alloys' composition, and this research has lead to the development of thin compact oxide scales exhibiting strong adherence to the metal substrate. Most commercial alloys now include reactive elements (as yttrium, cerium and lanthanum) or their oxides (Yang 2008). The addition, in small proportions, of these elements has demonstrated dramatic effects on oxide scale development, particularly in terms of growth kinetics, morphology

and microstructure, as well as on stress generation. These effects can lead to significant improvement of the interconnect lifetime.

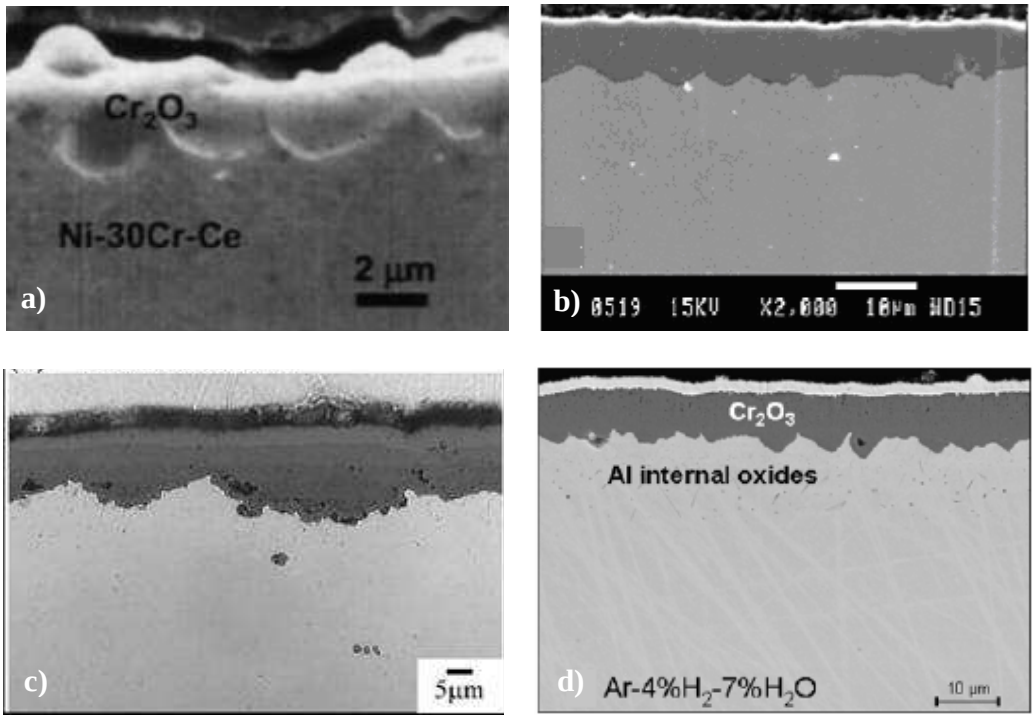

Figure 4.1: Oxide scale cross-section SEM micrographs showing morphological pattern development at the metal/oxide interface. From a) (Ramanarayanan, Mumford et al. 2000) b) (Mikkelsen and Linderoth 2003) c) (Peraldi and Pint 2004) d) (Essuman, Meier et al. 2007).

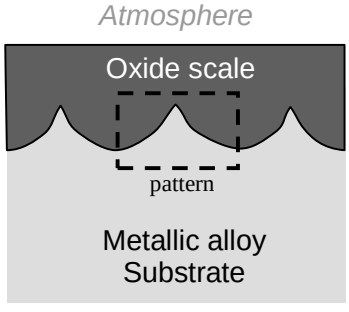

Figure 4.2: Schematic of the morphological pattern at the metal/oxide interface.

Under these conditions, the chromia scales have been shown to develop by significant, if not dominant, direct (inward) oxidation of the metallic substrate, unlike regular chromia scales which essentially grow outward at the free surface (Hou and Stringer 1995). Consequently, in these material systems oxidation at the metal/oxide phase boundary becomes more critical. Furthermore, this interface is highly constrained, which might locally affect the thermodynamic process and lead to non-uniform development of the oxide scale. Growth and thermal stresses result in a dominant in-plane compressive state of the oxide scale, reaching up to several gigapascals. In this situation, the oxide/metal interface geometry is of primary concern for the material system's resistance to failure, since it might lead to high stress concentration and to the rise of local tensile tractions, prompting crack nucleation (Mougin, Lucazeau et al. 2001).

In this study, a mechanism of stress-induced roughness development at the oxide/metal interface is investigated. A morphological pattern has been identified on several micrographs available in the literature, both on iron- and nickel- based metallic alloys, at temperatures ranging from 800 to 1100°C, as shown in Figure 4.1 (Ramanarayanan, Mumford et al. 2000; Mikkelsen and Linderoth 2003; Peraldi and Pint 2004; Essuman, Meier et al. 2007). In each of these experiments, either the atmosphere contained water vapor or the metallic alloy composition included reactive elements, two factors known to promote an inward oxide scale growth (Hou and Stringer 1995; Essuman, Meier et al. 2007). A schematic is provided on Figure 4.2. The pattern is constituted of a sharp valley surrounded by rounded regions, and exhibits a period of few µm under the fast growth conditions of the experiments. It is believed today that the main growth stress source in chromia scales developing at high temperatures comes from a

mechanism of secondary oxidation within the oxide scale grain boundaries. Therefore, it is proposed here that the high local compressive stress resulting from this process locally slows down the oxide propagation over the metallic substrate, resulting in the morphological pattern development.

4.2.2 Simulation description

The slow growth of a chromia scale over a ferritic stainless steel used in SOFC interconnect is simulated at 800°C. The objective is to study the stability and development of roughness at the metal/oxide interface, coupled with the increase in growth stresses. A small roughness is considered to develop in an initial step, and the stress-affected inward growth of the oxide layer is then simulated. A schematic presenting the initial situation and the expected evolution is provided in Figure 4.3. The simulation considers a rectangular domain of metallic substrate with an oxide phase developing from the initial top surface. The domain width is here set to 2µm, to be representative of the length scale of a half period of the identified pattern. The modeled initial roughness presents a maximum height of about 0.07 µm and an angle with respect to the axis $-x_2$ of 75°. A lateral symmetry condition is enforced, and the domain is constrained against in-plane expansion/shrinking. Furthermore, the bottom boundary is fixed, but the top surface is free. During cooling to room temperature, the thermal contractions that the substrate alone would experience are enforced as in-plane displacement boundary conditions to the domain, assuming that the oxide scale thickness is negligible in front of that of the metallic substrate. The materials' parameters are given in Table 4.1 for the metallic alloy, here taken to be a Crofer 22 APU ferritic stainless

steel (ThyssenKrupp-VDM 2005), and the chromia scale (Huntz, Daghigh et al. 1998). Note that except otherwise specified, creep relaxation is assumed negligible at this temperature and thus not accounted for in this analysis. The numerical scheme implemented requires a fine mesh in the vicinity of the propagating metal/oxide phase boundary. Consequently the oxidation zone is finely meshed using around 40000 1st order elements of dimensions 0.01×0.01 μm.

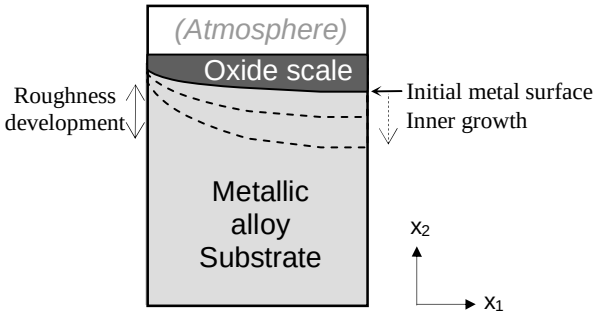

Figure 4.3: Schematic of the simulation initial configuration and expected evolution.

The long term isothermal inward growth of the oxide layer is limited at high temperature by oxygen diffusion through the developed scale. The initial configuration is obtained from the imposed non-uniform development of a thin oxide layer (~0.2 μm over 2hrs) from a stress-free system. A fixed unit concentration is considered at the free surface for oxygen, providing that the absorption process is infinitely fast compared to the ionic transport. The oxygen solubility in the metallic alloy is assumed negligible and constant diffusivities are employed. Effective diffusion parameters are formed by multiplying the diffusivities with the stress-free relative vacancy concentration at the phase boundary, $\delta_{\mathrm{V}} = C_{\mathrm{V}} / C_{\mathrm{O}}$, which constitutes the scaling factor for the diffusion

gradient. This parameter is fitted to obtain a typical parabolic rate value for chromia growing on a ferritic steel, about 10^{-18} m^2s^{-1} (Fergus 2005). This gives an oxide layer thickness of about 1.5µm after 400 hours of oxidation in a case of uniform growth.

A mechanism of in-plane growth strain generation resulting from secondary oxidation within oxide scale grain boundaries, as introduced by Rhines and Wolf (Rhines and Wolf 1970) and modeled by Clarke (Clarke 2003), is considered in this analysis. The constant A_{gb} (see equation (3.10)) is set to give a maximum in-plane growth strain of a few percent over the simulation time, in order to compare with values that have been experimentally measured during the growth of an alumina scale (Tolpygo, Dryden et al. 1998).

The initial driving force for a stress-free flat metal/oxide phase boundary, f_I^0, is unknown. A small enough value (in front of the chemical composition variation term) is required in order to obtain a parabolic shape for a uniform oxide scale growth kinetics, as indicated by inequation (3.20). On another hand, this constant also set the sensitivity of the oxidation kinetics to the stress and curvature related contributions at the interface. Here we assume that in the situation considered, the oxide phase is stable and its local dissolution is unlikely to occur. This means that f_I^0 is greater than the expected magnitude of the stress and curvature terms. A value of $f_I^0 = 10^7\ \mathrm{J/m^3}$ has thus been chosen, which is comparable to the one employed in the thermal barrier coating analysis. A phase boundary mobility $M_I \approx 10^{-19}\ \mathrm{m^4/J/s}$ is then obtained from equation (3.27).

To the author's knowledge, no values are available in the literature for the vacancy diffusivity along a chromia/ferritic steel phase boundary. It is here estimated to be significantly higher than the grain boundary diffusivity within the oxide, allowing for the

large mass redistribution along the interface required for a uniform oxide scale growth in a stress-free situation. The oxygen grain boundary diffusivity is typically few orders of magnitude higher than the effective through scale diffusivity, resulting from the fast path over volume diffusivity and area fraction ratio. A minimum bound is then assumed for the phase boundary diffusivity to be of the order of $D_V^I \approx 10^4 D_V^{ox}$. Again very few data are available for the oxide/metal interfacial energy. A usually reported value for metal/alumina systems, $\gamma_I \approx 1\ \mathrm{J/m^2}$, will serve here as a reference (Murr 1973; Panat, Hsia et al. 2005; Saiz, Cannon et al. 2008). The influence of these two parameters is discussed later.

Table 4.1: Mechanical properties of the oxide scale and the metallic substrate at 800ºC.

Parameter	Symbol [units]	Material	
		Metal	Oxide
Young's modulus	$\boldsymbol{E}$ [GPa]	140	225
Poisson's coefficient	$\boldsymbol{\nu}$ []	0.3	0.28
Yield stress	$\boldsymbol{\sigma_y}$ [MPa]	30	1000

4.2.3 Mechanism of roughness development

The objective of this study was to investigate under which conditions an increase in growth stresses could lead to the stability and growth of an initially existing roughness, and its development towards the identified morphological pattern presented on Figure 4.2. The initial roughness considered could result from a mechanism of discrete nucleation of the oxide phase followed by lateral nuclei expansion, from an interfacial

energy equilibrium configuration at the intersection of an oxide grain boundary with the phase boundary, or from a slower local oxidation kinetics induced by the presence of segregated impurities or alloying elements at the interface.

The analysis of the morphological pattern provides some indications of its development. The rounded shape seems to indicate the significant contribution of the curvature smoothing driving force for the oxide/metal boundary propagation aside from the peak. The sharp angle of the morphological pattern clearly indicates the presence of a strong singularity. Since homogeneous materials are considered here, the singularity is modeled through a lower local interfacial energy (by an order of magnitude), allowing for the stability of a high local curvature. This situation could result from a particular interface composition at this location. While this singularity is essential for the morphology, it does not provide a mechanism for its development. From a thermodynamic approach, the metallic alloy's locally slower kinetics of oxidation would result from a higher energy required to propagate the phase boundary. While chemical or microstructural considerations might be relevant, we propose here to investigate the possible role of growth stresses. These stresses are essentially in-plane compressive for the growth of a chromia scale on a metallic substrate at high temperature, and might reach few gigapascals (Mougin, Galerie et al. 2002). From the model presented above, this situation is likely to significantly alter the driving force for the oxide/metal boundary propagation. If the interface geometry induces a variation of this effect along the discontinuity, a large redistribution of the incoming oxygen flux could be induced, resulting in the non-uniform growth of the oxide scale.

Two sources of growth strain have been investigated. While its relevancy has been contested over the last decade, the historical Pilling and Bedworth mechanism (Pilling and Bedworth 1923) takes place directly at the metal/oxide interface and might therefore play an important role in stress-affected inner oxidation. The influence has been described by Evans on one-dimensional oxidation kinetics (Evans 1995). However, we are here interested on local non-uniformity in oxide scale growth rather than variations in global kinetics. The mechanism has been tested, but it appeared essentially to flatten the interface in this case of limited initial roughness and uncoated alloy (see the TBC case investigation for an opposed situation). The large volume change associated with the oxidation process at the interface induces a tensile traction at the locations where the phase propagation is slower. In turn, an effect of traction homogenization takes place, resulting from the dominancy of the work term (see equation (2.53)) in this case, which promotes a higher oxidation kinetics at the tensile traction location and a slower kinetics where it is compressive, thus acting to flatten the metal/oxide phase boundary.

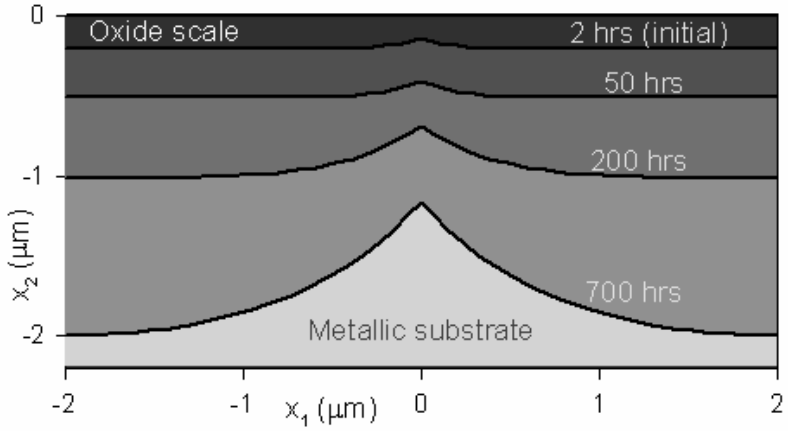

Figure 4.4: Metal/oxide boundary propagation after different oxidation times.

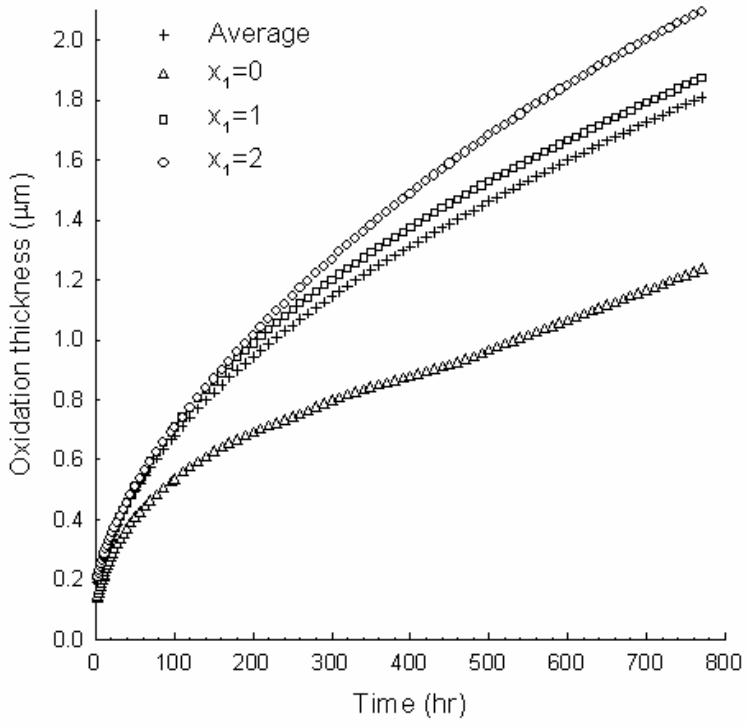

Figure 4.5: Average oxidation kinetics and values at different x_1-coordinates.

In contrast, the elastic energy jump at the interface presents a destabilizing role. It is likely to be dominant over the work term in a case of minor volume change directly associated with oxidation at the phase boundary and large in-plane stresses. The mechanism of in-plane growth strain development due to secondary oxidation along the oxide scale grain boundaries provides a framework for this situation. The metal/oxide boundary propagation after different oxidation times obtained from a simulation of isothermal oxidation is presented in Figure 4.4. The results have been extended by symmetry with respect to the axis x_1=0 for illustration purposes. This case considers $D_V^I \approx 10^6 D_V^{ox}$ and $\gamma_I \approx 2$ J/m^2. The initial roughness gradually develops with oxidation time, growing from less than 0.1μm to about 0.8 μm after 700 hours. The roughness is

here simply defined as the difference between the maximum and minimum oxide scale thicknesses, since the simulated domain includes a unique local variation in thickness. This phenomenon results from a varying oxidation kinetics along the interface as can be seen on Figure 4.5, which shows the local history of oxidation layer thickness at different coordinates along the phase boundary, along with the average value for comparison. The oxide scale growth is slower at the peak location (x_1=0), where the oxidation rate decreases during the first 200 hours and then seems to reach a constant linear value. It is maximum at the valley (x_1=2), although the deviation from the average kinetics is more gradual with time.

The variation in local oxidation kinetics is induced by the non-uniform jump in elastic energy between the two phases along the interface, differently affecting the phase transformation thermodynamics. Figure 4.6 a) presents the change in elastic energy of the transformed volume over the process, $\left\{\Pi_I W^{e,-} - W^{e,+}\right\}$, versus normalized coordinate along the phase boundary, for different times. The peak at the singularity (x_s=0) constitutes an excess energy to provide for the oxide propagation at this location.

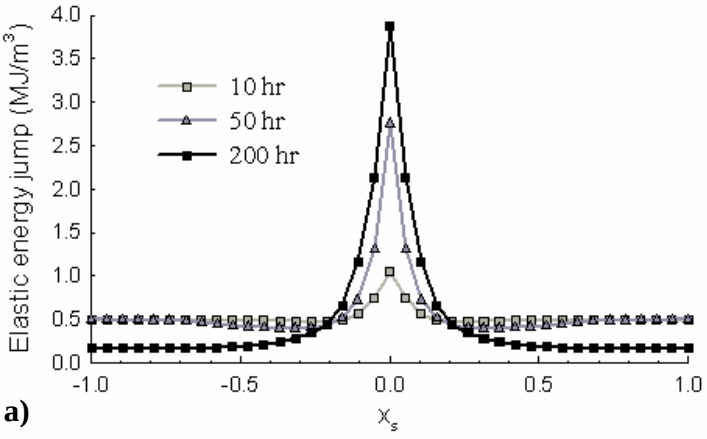

a)

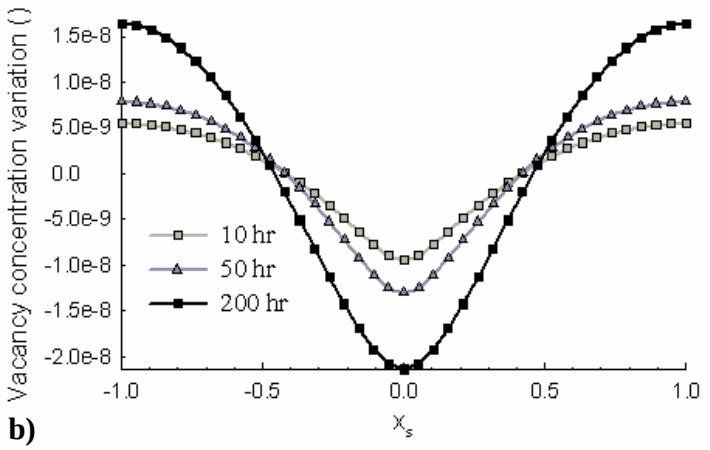

b)

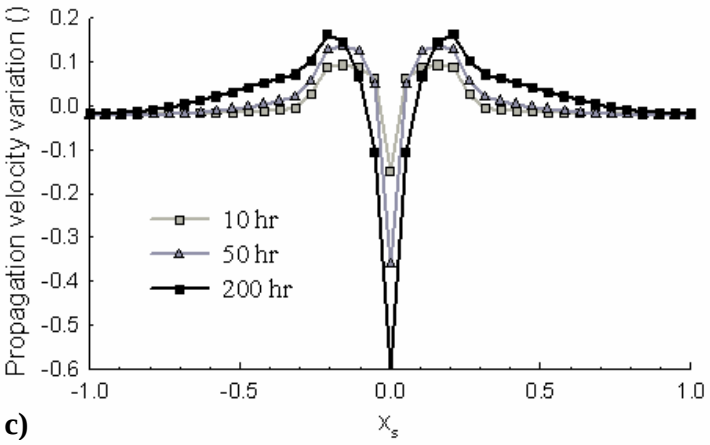

c)

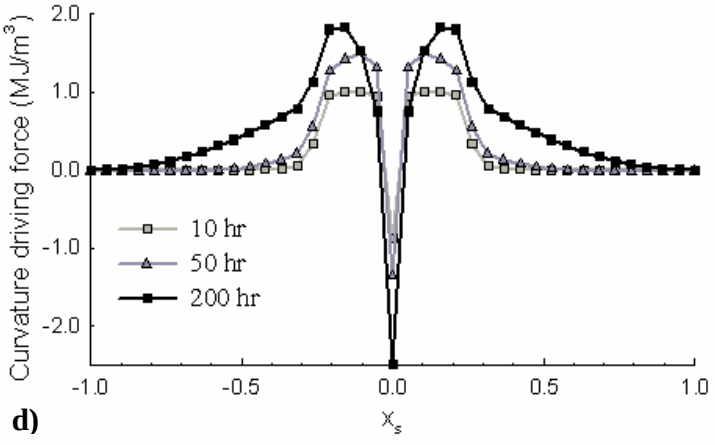

d)

Figure 4.6: a) Elastic energy jump, b) vacancy concentration variation, c) propagation velocity variation and d) curvature driving force along the metal/oxide boundary vs normalized coordinate, given for different oxidation times.

Therefore the oxidation is locally slowed down, and consequently the local concentration of vacancy decreases due to their diffusion overpassing the generation process. This phenomenon leads to an increase of the local chemical energy jump which tends to compensate the elastic contribution. However, the fast diffusion induced by the composition gradient along the phase boundary prevents formation of a local equilibration, and as a result the oxide phase propagates following a non-uniform kinetics. The variations, relative to the respective average value, of the vacancy concentration and the normal propagation velocity along the interface are shown in Figure 4.6 b) and c). As can be observed, the propagation velocity exhibits large deviations, from about +20 to -60% at the singularity after 200 hours, which drives the roughness development. As the phase boundary geometry evolves, its local curvature changes, raising a driving force which counterbalances the elastic energy jump, as shown on Figure 4.6 d). The driving force for the roughness development mechanism is the increase of in-plane growth stresses, presenting a strong variation at the interface singularity. This variation is induced by the history of local growth strain generation, directly related to that of diffusion from equation (3.10), and from the material system geometry. The maximum value at the singularity increases with time in a first period, up to around 200 hours, and then remain quite constant once the oxide elasticity limit is reached. The width of the peak widens along with the roughness development.

4.2.4 Influence on mechanical failure

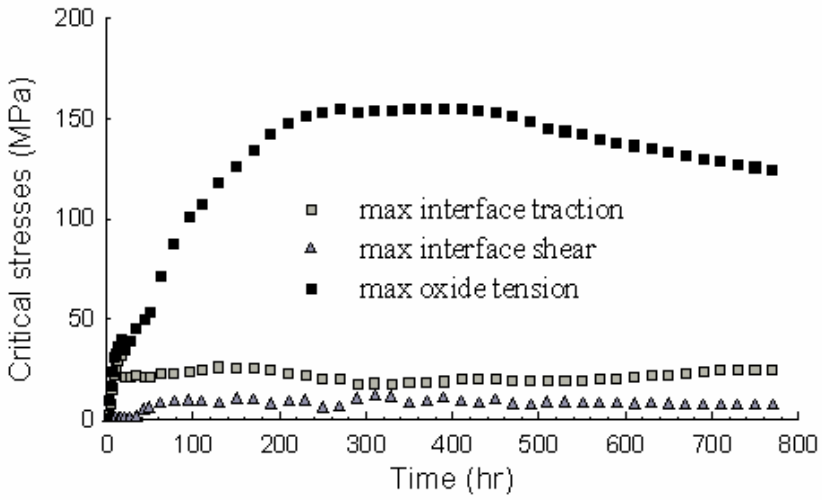

Figure 4.7: Critical stresses development with time at oxidation temperature during isothermal simulation.

Flat chromia scales grown in an SOFC environment undergo in-plane compression and typically fail by delamination, following buckling or shear cracking (Birks, Meier et al. 2006). An energy criterion is then used in association with the interface fracture strength to describe the situation regarding failure (Evans 1948). The total elastic energy stored within the oxide scale is lower in the case of a stress-affected oxidation than in the uniform growth situation. Indeed, the introduced thermodynamic influence tends to limit the system elastic energy increase by slowing down oxidation at the most stressed locations and promote the oxide propagation where it is less constrained. Therefore, the non-uniform development would be beneficial to the material system lifetime from the energy criterion. However, this approach is only relevant to compare situations of uniform oxide growths.

Tensile stresses within the oxide scale as well as shear and tensile traction at the metal/oxide interface develop in a case of non-uniform morphology, particularly upon cooling. The strengths of the brittle oxide and the oxide/metal interface under these loadings are usually much lower than that of normal compression, and therefore such a situation is likely to accelerate the mechanical failure of the system. The maximum values of these critical stresses within the domain considered have been monitored during the roughness development associated with isothermal oxidation and upon the material system cooling to room temperature.

The results at oxidation temperature are presented in Figure 4.7. It is observed that the critical stresses are limited at the interface and are quite constant, which results from the high ductility of the ferritic stainless steel substrate at elevated temperature (the yield stress is 30MPa). A tensile stress develops within the oxide scale during the first 200 hours, reaching around 150MPa before slowly decreasing. It is located half-way through the thickness on the side of the roughness tip, and oriented along the out-of-plane direction. It thus may induce in-plane crack nucleation and growth at this location. However, the tensile strength of chromia at 800°C, needed for evaluation of this situation, is missing. But the low level compared to the maximum shear stress (around half the plastic yield stress here, i.e. about 500MPa) and long term decrease make it unlikely that this would be a dominant failure mechanism that would limit the material systems long-term lifetime. Such a failure mode is besides not typically observed during isothermal oxidation. Delamination or shear cracking rather take place.

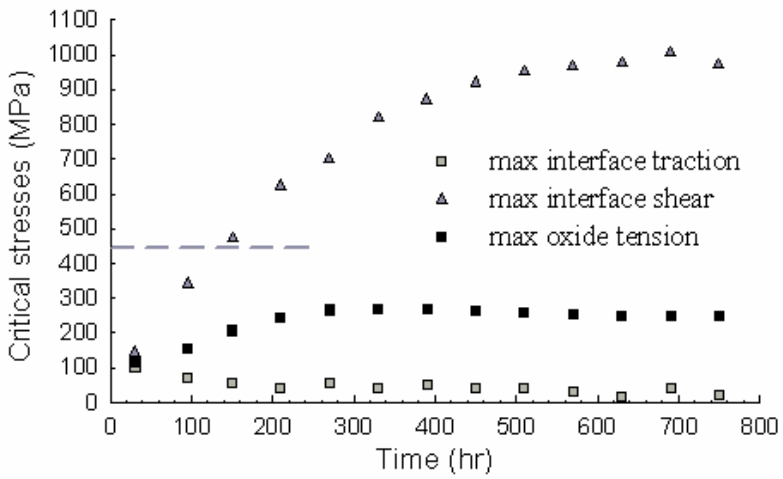

Figure 4.8: Critical stresses upon cooling to room temperature vs isothermal oxidation time. The dashed line shows the interfacial shear strength.

The same critical stresses upon cooling to room temperature after different isothermal oxidation times are provided in Figure 4.8. The maximum tensile traction at the interface remains very limited even upon cooling. The traction is in fact essentially compressive. Again the maximum tensile stress within the oxide scale increases in a first time, to around 270MPa after 300 hours; it then slowly decreases. Its location and direction are the same as observed at oxidation temperature. This value lays within the range of experimental data for the tensile strength of chromia at room temperature, 178 to 400MPa (Takano, Komeda et al. 1998; Li, Brook et al. 1999; Hirota, Motono et al. 2002), such that it is likely to induce out-of-plane crack nucleation and growth. However, failure is more likely to occur at the oxide/metal interface by shear-driven delamination, a mechanism also identified as most detrimental by Sun et al. for a thermally grown chromia/Crofer 22 APU system (Sun, Liu et al. 2008).

The roughness development with isothermal oxidation time results in the increase of a high maximum shear stress at the phase boundary, which increases along with the morphology size (see Figure 4.9). The increase is quite linear up to 400 hours, where the maximum shear stress reaches around 900 MPa, and the further evolution gradually slows down and seems to reach an asymptotical value of 1GPa. Such a high shear at the ceramic/metal interface would probably engender the growth of interfacial cracks leading to the delamination of the oxide scale, since it is more than twice the interfacial shear strength determined by Sun et al. for a thermally grown chromia/Crofer 22 APU system (Sun, Liu et al. 2008) (the mean value, 442.5MPa, is plotted in Figure 4.8). The lifetime before failure is around 150 hours in this case, which is extremely limited in comparison with the value of about 5000 hours obtained by Liu et al. for the same material system but with an interface remaining flat (Liu, Sun et al. 2009) (interfacial shear stress develops at the edges of the metal plate considered in this case). This demonstrates the very detrimental effect of an interfacial roughness development on the mechanical lifetime.

4.2.5 Influence of material-related parameters

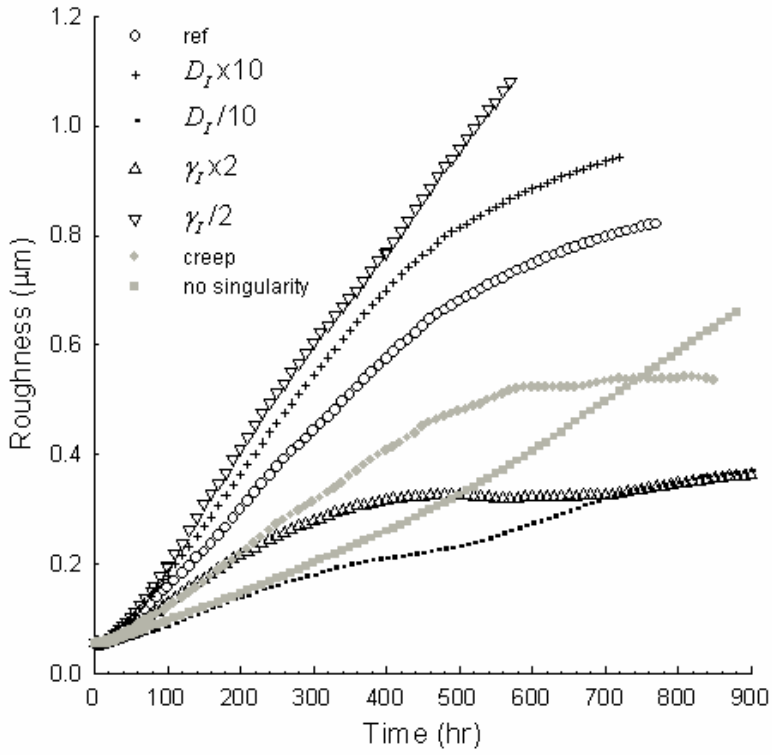

Figure 4.9: Roughness development with isothermal oxidation time, given for different parameters variations from the reference case (ref).

Roughness development is thus detrimental to the oxide scale/metallic alloy system's mechanical lifetime, because it induces the increase of critical tensile and shear stresses, particularly upon cooling. In a second time, the kinetics of the phenomenon during isothermal oxidation was studied. The results for the reference case treated before and variations of the main parameters are presented in Figure 4.9. In the reference case, the roughness development follows a constant time rate until 450 hours and then gradually decreases. This indicates a kinetic limitation of the phenomenon, and the approach to an equilibrium situation towards the end of the oxidation simulation time. The non-uniform

oxidation at the inner interface results from a stress gradient along the phase boundary, which increases until an in-plane biaxial compressive plastic state is reached on the oxide side (at about 200 hours, see Figure 4.6 a)). The peak at the singularity then slowly spreads, but the roughness continues to develop until the curvature gradient results in a counteracting driving force which equilibrates with the stress energy profile.

The kinetics of the roughness development mainly depends on the diffusivity along the interface, which controls the redistribution of the incoming oxygen flux at the phase boundary, and which thus sets the amplitude of the non-uniformity in instantaneous oxide phase propagation velocity. It can be seen in Figure 4.9 that an increase by an order of magnitude significantly increases the developed roughness, but a decrease of the same order dramatically slows down the phenomenon kinetics. This sensitivity is of major importance considering the uncertainty on the interface diffusivity data, and its likely high variation according to changes in the microstructure and the composition along the phase boundary, notably due to segregated impurities, alloying elements and additives. The same comment can be made with regard to the interfacial energy, which for a given stress gradient sets the associated equilibrium curvature profile and consequently the interface morphology. It can be seen here that when the interfacial energy is taken to be half the value used in the reference case, the roughness reaches a steady-state value around 0.3µm after approximately 400 hours. At contrary, when the interfacial energy is doubled the roughness development is much faster and the equilibrium configuration is not approached within the simulated time.

The contribution of creep relaxation in a chromia scale growing at 800°C is not generally accounted for, but it has been shown to be significant in some experiments

(Huntz, Daghigh et al. 1998). The influence on the roughness development phenomenon has also been tested, using a power creep law with the parameters identified by Huntz et al. (Huntz, Daghigh et al. 1998). The creep relaxation decreases the amplitude of the stress gradient along the phase boundary, thus lowering the steady-state roughness as shown in Figure 4.9. Finally, a last situation has been considered in which no local singularity in interfacial energy is assumed. This results in a dramatic decrease of the roughness development. The plot in Figure 4.9 has been obtained with an interfacial energy 4 times lower than in the reference case (but still 2.5 times higher at the singularity location).

This points out the likely highly detrimental role of non-uniformities in composition and/or microstructure along the metal/oxide interface. If they can't be avoided an increase of their density might be beneficial, since for a given curvature profile a decrease of the concerned phase boundary segment length would result in a diminution of the geometry roughness (shrinking of the morphology pattern). Coupled homogenization and refinement of the initial metallic substrate surface microstructure and composition, associated with an increase of the oxide nucleation density (to obtain a finer oxide scale microstructure) would then limit the amplitude of the roughness developing during the oxide scale inner growth; this would allow for an increase in the oxide scale mechanical lifetime. Finally, it is important to note that the roughness development is only weakly related to the oxide scale growth kinetics. The phenomenon relies in essence on the inward oxide development, which then provides an upper limit to its extent. But on the other side the roughness long-term development is essentially controlled by the materials mechanical and interfacial properties. This situation greatly differs from that considered

by Liu et al., in which the mechanical lifetime is highly dependent on the oxide scale thickness growth kinetics (Liu, Sun et al. 2009).

4.2.6 Conclusion

A mechanism of roughness development associated with isothermal inward oxide scale growth on a metallic alloy at high-temperature is proposed and studied. It relies on a stress-induced thermodynamic effect on the local oxidation kinetics at the metal/oxide interface. The continuum mechanics/diffusion framework includes a mechanism of in-plane growth strain generation resulting from secondary oxidation within oxide scale grain boundaries, plastic stress accommodation and a fast diffusion path along the propagating phase boundary. The non-uniform growth of a chromia scale over a ferritic stainless steel used in SOFC interconnects is simulated. The conditions allowing for the development of a roughness pattern identified on several micrographs in the literature are investigated. The generation in association with the oxide growth process of an in-plane inelastic strain, as described by the Rhines and Wolf theory, can promote the gradual development of a small initial roughness, under the influence of the engendered compressive elastic energy gradient along the interface. The roughness formation induces the increase in critical tensile and shear stresses, particularly upon cooling. Their development with isothermal oxidation time is studied, demonstrating the likely detrimental contribution of the phenomenon on the oxide scale/metallic alloy system mechanical lifetime. Finally, the influence of the main parameters and processes on the roughness development kinetics are discussed, providing new directions for the design of

long-term resistant metallic alloys for SOFC interconnects. The following properties should be forsaken:

(1) An homogeneous composition and a fine microstructure at the microscopic scale of the metallic alloy surface;

(2) A low oxygen diffusivity along the metal/oxide boundary;

(3) A high interfacial energy;

(4) Low oxygen and chromium diffusivities within the oxide scale grain boundaries to limit the local phenomenon of strain generation resulting from secondary oxidation;

(5) A fine oxide scale microstructure to enhance creep relaxation.

4.3 Investigation of a thermal barrier coating system

4.3.1 Introduction

Thermal barrier coatings are used in aircraft and industrial gas-turbine engine to allow a high functioning temperature while maintaining sustainable conditions for the metallic structure. However, at high temperature, an oxide scale (commonly named thermally grown oxide, TGO) develops between the coating, usually made of yttria-stabilized zirconia (YSZ), and the metallic bond coat (BC), limiting the lifetime of the coating and as a consequence the long term reliability of the structure. The oxide scale, mainly constituted of alumina oxide, presents significantly different thermal expansion and creep properties than the surrounding YSZ and BC layers. This induces high stresses and deformations upon cooling at room temperature, leading to crack nucleation and eventually to the spallation of the top coat. Thus, the growth of the TGO during high temperature operations is the most important phenomenon responsible for the TBC intrinsic failure (Padture, Gell et al. 2002; Evans, Clarke et al. 2008). However, if the global mechanisms driving the oxide scale development are well known, the factors for varying kinetics and the development of a rough and undulated scale are poorly understood.

Initial undulations appear during the BC and YSZ coatings deposition processes (Evans, Mumm et al. 2001; Panat and Hsia 2004; Vaidyanathan, Jordan et al. 2004; Panat, Hsia et al. 2005; Busso, Wright et al. 2007). The wavy interface might then evolve in a detrimental manner during functioning oxidation. Several studies have investigated the development of undulations at the TGO/BC interface, pointing out the key roles of oxide growth stresses and interface geometry (He, Evans et al. 2000; Spitsberg, Mumm et

al. 2005; Tolpygo and Clarke 2007; Evans, Clarke et al. 2008). These works focus on plastic and creep deformation during cooling and heating cycles, or stress-driven material diffusion within the BC (Panat, Hsia et al. 2005; Panat, Hsia et al. 2005), but all consider a uniform growth of the TGO. To our knowledge, no study has been performed considering a local effect of stress on the oxidation kinetics at the BC/TGO interface, which could result in the non-uniform growth of the oxide scale, a factor which has been identified as strongly detrimental to the TBC lifetime (Evans, Clarke et al. 2008). It would result in additional stress concentrations upon cooling and might lead to large local scale deformations of the oxide layer, accelerating the development of cracks and spallations. Even limited oxide scale morphology variations might become significant under the effect of thermal cycling. Therefore, it is of primary interest to understand the mechanisms leading to a non-uniform oxide growth, quantify the contributions and identify the most influential physical parameters. This should allow for the optimization of the TBC material system design in terms of composition and fabrication process, and also help predicting the location of failure.

4.3.2 Simulation description

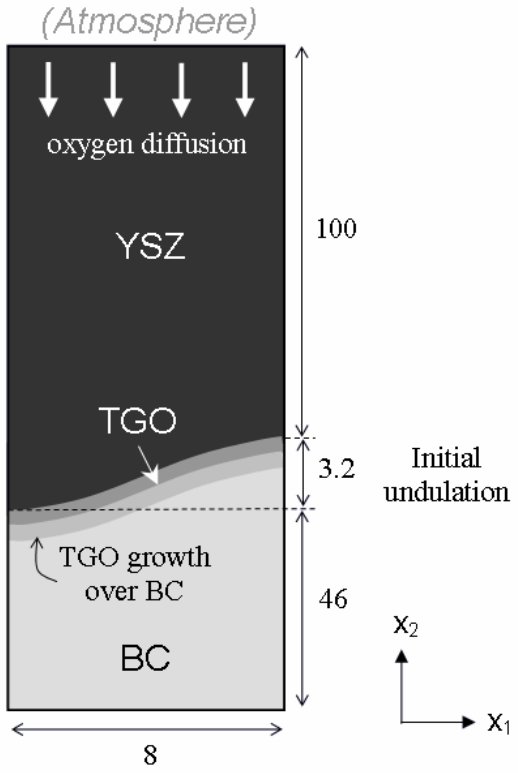

Figure 4.10: Schematic of the TBC system model (not to scale).

The framework developed is applied to a practical case concerning a thermal barrier coating (TBC) formed by electron-beam physical vapor deposition (EB-PVD) of yttria stabilized zirconia (YSZ) over a Pt-aluminized NiAl bond coat (BC) adapted from the model by Busso et al. (Busso, Lin et al. 2001; Busso and Qian 2006). The simulation describes the long-term isothermal growth of the oxide layer (named thermally grown oxide, TGO) at the operating temperature, 1100°C, by oxidation of the metallic bond coat at the metal/oxide interface. The simulation domain describes a cross-section perpendicular to the YSZ/BC interface plane and is meshed with generalized plane strain elements. The YSZ and BC layers are modeled, and the initial YSZ/BC interface is

idealized as a wavy-type segment, as introduced by Busso et al. from scanning electron microscopy micrograph observations. Here the initial interface is described by a generic quarter sin period, as presented on Figure 4.10, of dimensions representative of a typical local roughness after coating deposition (8µm-width and 3.2µm-depth) (Busso and Qian 2006; Busso, Wright et al. 2007). Symmetry boundary conditions are enforced for displacement at the lateral sides and for the thickness of the domain, which forces the system to expand uniformly in the in-plane directions (x_1 and x_3). Additionally, in order to account for the in-plane deformations practically imposed by the thick substrate, displacement boundary conditions are effectively applied in these directions. At the oxidation temperature, a value typical of creep rates exhibited by single crystal superalloys in service is used, $\dot{\varepsilon}_{11} = \dot{\varepsilon}_{33} = 10^{-9}\mathrm{s}^{-1}$ (Busso, Lin et al. 2001). Finally the simulation domain is fixed at the lower boundary but free to expand at the top surface. The materials parameters are given in Table 4.2 for the bond coat (Pan, Chen et al. 2003), the thermally grown oxide (Cheng, Jordan et al. 1998) and the YSZ coating (Cheng, Jordan et al. 1998; Busso and Qian 2006). For the oxidation volume eigenstrain, The Pilling-Bedworth ratio is taken from the primary oxidation reaction as $\Pi = 1.28$, which gives an isotropic volume strain of $\varepsilon_{vol}^{\Pi} \approx 0.08$. From the numerical scheme implemented the propagating metal/oxide phase boundary description within the finite elements domain relies on the mesh. The zone covered by oxidation during the simulation is then finely meshed using 36000 1st order elements of dimensions 0.02×0.04 µm.

Table 4.2: Mechanical properties of the bond coat, the TGO and the YSZ thermal layer at 1100ºC.

Parameter	Symbol [units]	Material		
		Bond coat	Oxide	YSZ
Young's modulus	$\boldsymbol{E}$ [GPa]	92	320	173
Poisson's coefficient	$\boldsymbol{\nu}$ []	0.3	0.25	0.12
Yield stress	$\boldsymbol{\sigma_y}$ [MPa]	30	1000	-
Creep parameters	N_{cr} [] A_{cr} [MPa$^{-Ncr}s^{-1}$]	4 1.5 10^{-11}	2.3 5 10^{-13}	- -

The long term inner TGO growth at high temperature is limited by the oxygen inward diffusion through the developed scale. The initial configuration is here obtained from the uniform growth of a thin oxide layer (0.5 μm) from a stress-free system in a time obtained from the empirical kinetics law in (Busso and Qian 2006) (about 30 hr). A fixed unit concentration is considered at the free surface for oxygen, providing that the absorption process is infinitely fast compared to the ionic transport. The oxygen solubility in the bond coat is assumed negligible and constant diffusivities are employed. Effective diffusion parameters are formed by multiplying the diffusivities with the stress-free relative vacancy concentration at the phase boundary, $\delta_{\mathrm{V}} = C_{\mathrm{V}} / C_{\mathrm{O}}$, which constitutes the scaling factor for the diffusion gradient and is enforced at the initial step. This parameter is fitted for the TGO so that the scale growth kinetics matches globally the value of the experimental data over the simulated time. A value of $D_{\mathrm{O}}\delta_{\mathrm{V}} \approx 10^{-18}\,\mathrm{m^2 s^{-1}}$ is thus assigned. The diffusion parameter for the YSZ layer is obtained through the ratio of its diffusivity to the one of the alumina scale, which gives a ratio around 10^7 from (Huntz, Balmain et al. 1997) and (Krishnamurthy, Yoon et al. 2004). Such a high value

makes the thermal coating, as it is known, transparent for oxygen diffusion. Symmetry boundary conditions are applied on the lateral sides of the domain for diffusion (zero flux normal to the boundary). To the author's knowledge, no values are available in the literature for the vacancy diffusivity along the BC/TGO phase boundary. It is here estimated through the surface self-diffusivity of Ni (Bonzel and Gjostein 1968) and gives a diffusion parameter of $10^{-11}\mathrm{m}^2\mathrm{s}^{-1}$. The metal/alumina interfacial energy is taken to be $\gamma_I = 1\ \mathrm{J/m}^2$, based on experimental data (1.38 J/m^2 (Murr 1973)) and values used in other studies (1.1J/m^2 (Saiz, Cannon et al. 2008), 1J/m^2 (Panat, Hsia et al. 2005)). Finally, in order to set the oxidation kinetics, the driving force for a stress-free flat metal/oxide phase boundary, f_I^0, has to be defined. Since no bibliographic or experimental data of this parameter have been found in the literature, it has been set from physical considerations. Observation of the oxide/metal interface morphology has been used to set f_I^0. The curvature-related thermodynamic force, $\kappa\,\gamma_I$, can easily be quantitatively estimated since the interfacial energy is known and the curvature range can be identified from cross-section micrographs. Since it compares with f_I^0 for the interface evolution, it thus provides references for the setting of this parameter. The first considered situation is that the effect of the curvature-related thermodynamic force alone on the phase-boundary propagation should be negligible on the initial interface geometry corresponding to the experimentally observed roughness. This allows for the uniform growth of the convoluted oxide scale when stresses are negligible. The initial waviness exhibiting a curvature radius of the order of 10µm, it requires: $f_I^0 \gg 1/(10\times10^{-6})\ \gamma_I$. The second situation considers the minimum bound of the roughness. From observation, it is estimated to

0.1μm. Consequently, smaller morphologies should be naturally flattened, giving: $f_I^0 \sim 1/(0.1\times10^{-6})\ \gamma_I$. Thus a value of $f_I^0 = 5\times10^7\ \mathrm{J/m^3}$ has been chosen. A value of $M_I \approx 10^{-19}\ \mathrm{m^4/J/s}$ is then obtained for the interface mobility from equation (3.27).

4.3.3 Mechanism of non-uniform thickness development

The results from the numerical simulations are presented in this section. They include the stress and curvature effects on the local propagation kinetics of the oxide-metal phase boundary, the volume eigenstrain generation from the direct metal oxidation at the inner interface and the time-dependent as well as time-independent behaviors of the different materials, and the specific mass diffusion along the propagating phase boundary. Note that the effect of an in-plane growth strain developing from a process of secondary oxidation within the oxide scale grain boundaries has also been tested. However, this mechanism alone results in a negligible phase transformation work at the propagating boundary due to no significant specific volume change at the interface. Furthermore, the local elastic energy in the oxide remains limited in this case owing to a high creep at the elevated considered temperature.

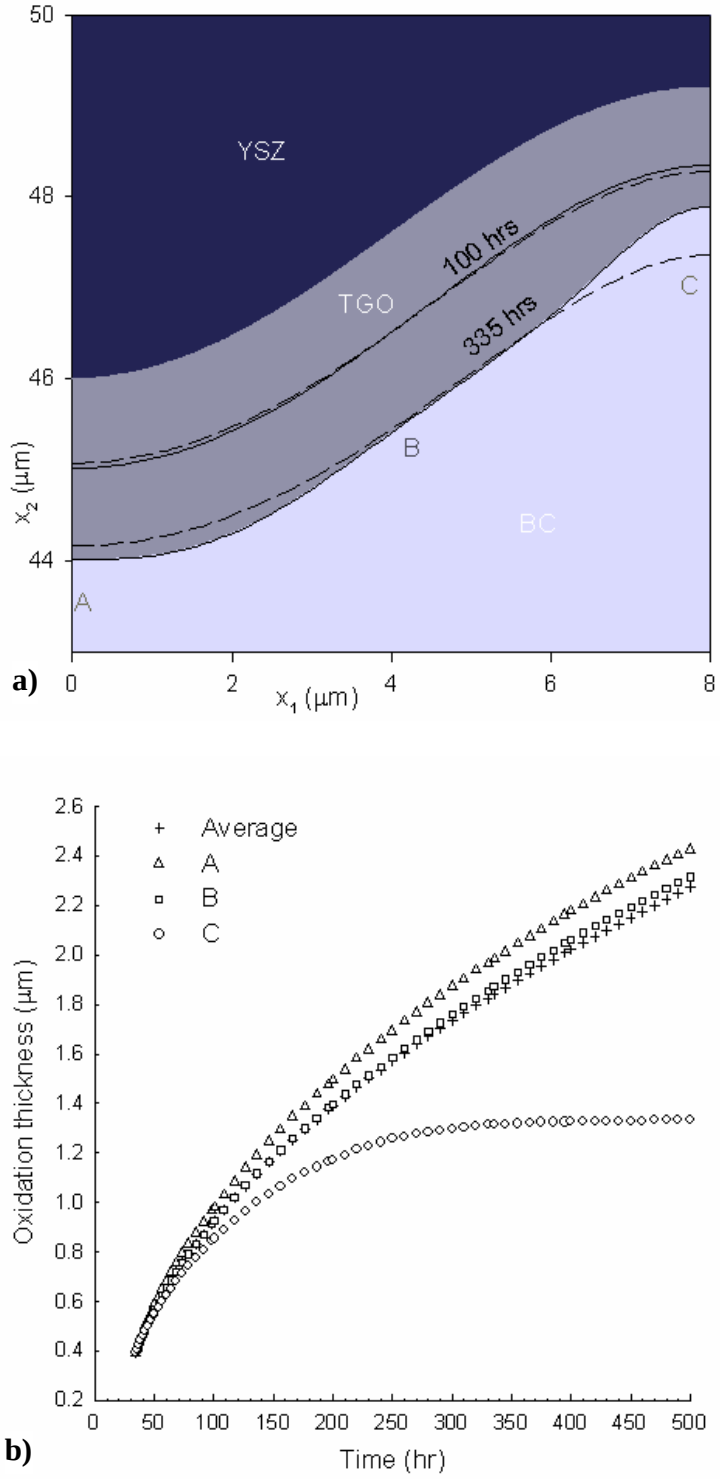

Figure 4.11: a) Oxidized bond coat layer after 100 and 335 hours of isothermal oxidation. The dashed lines show the interfaces corresponding to a uniform oxidation. b) Oxidation kinetics at different locations.

The oxidized bond coat layer in the TBC environment as predicted after 100 and 335 hours of isothermal oxidation is presented on Figure 4.11 a). Following the study by Busso and Qian (Busso and Qian 2006), these times have been selected because they represent a lower and an upper bound, respectively, of the oxidation time leading to the critical conditions resulting in the TBC spallation upon cooling at rest temperature. Also shown on Figure 4.11 a) for comparison are the oxide/metal interfaces at the different times which would correspond to a uniform oxidation. Note that the undeformed configuration is presented in order to point out the oxidation kinetics contribution to the oxide scale development, eliminating the effect of the large phase transformation volume eigenstrain in the true oxide thickness growth. During the first 100 hours of oxidation, the phase propagation has remained quite uniform. But during the following 235 hours, local oxidation kinetics have significantly differ leading to the development of significant non-uniformities in the oxidation layer thickness. The local history of oxidation layer thickness at different locations along the phase boundary is presented on Figure 4.11 b), along with the average value for comparison. The points A, B and C correspond to the peak, the mid-slope and the valley, respectively, of the oxide-metal phase boundary as illustrated on Figure 4.11 a). The average oxidized zone thickness follows the empirical kinetics law, giving 0.8 µm after 100 hours and 1.8 µm after 335 hours, but dissimilar local developments have been induced by the varying stress field along the inner interface. The highest oxidation kinetics is found to be at the peak and the slowest at valley, the mid-slope presenting a slightly above-average value. The main deviation is clearly located at the valley, where the oxidation is almost stopped after 300 hours. The

corresponding relative oxide zone thickness variations with respect to the average value at the three locations after 335 hours are +8% (A), +2%(B) and -29% (C), respectively.

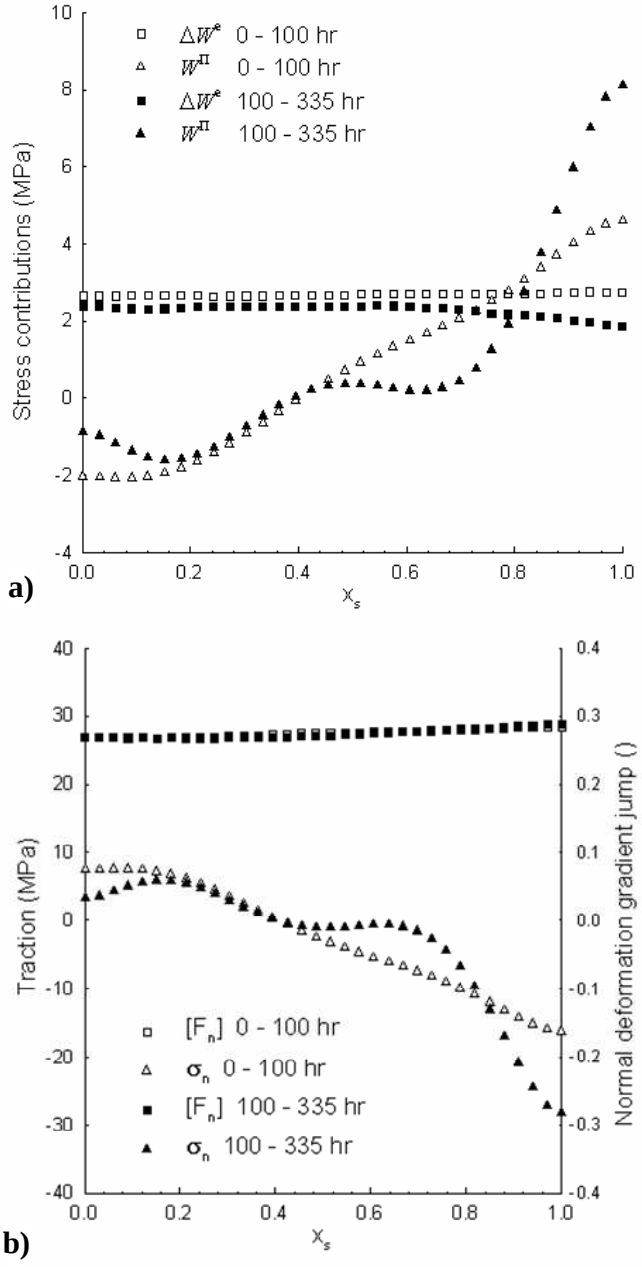

Figure 4.12: Average a) stress contributions and b) tractions and normal deformation gradients jump over the indicated time period vs normalized abscissis along the oxide-metal boundary.

In order to investigate the stress situation which lead to this non-uniform oxidation, the two contributions of the stress influence on the process kinetics, namely the work required to complete the deformation associated with the metal phase oxidation at the stressed interface, $W^{\Pi} = \frac{1}{2}\left(\sigma^{+} + \sigma^{-}\right) : [\mathbf{F}]$, and the change in elastic energy of the transformed volume over the process, $\Delta W^{e} = \left\{\Pi_I W^{e,-} - W^{e,+}\right\}$, are presented on Figure 4.12 a). The data are averages of the simulation steps contributions weighted by the average step propagation increments over the time ranges of interest in order to reflect the influences histories. It can be inferred that the local oxidation kinetics variations are essentially driven by the phase transformation work, which exhibits a much higher variation amplitude along the interface than the elastic energy change. This situation is due to the large phase transformation eigenstrain which leads to plastic accommodation of the components in the constrained directions, resulting in a similar dominant in-plane compressive state along the interface. However, the undulated geometry induces a varying situation along the free direction, which is the one of main development for the volume eigenstrain, resulting in high accommodation work variations along the phase boundary. The traction and the normal component of the deformation gradient jump along the phase boundary are presented on Figure 4.12 b), making explicit the main contributions to the oxidation work variations. The deformation normal to the phase boundary is quite uniform, around $\Pi_I - 1 = 0.28$, although it can be seen that it increases from the peak to the valley region. The higher value at the valley compared to the peak is due to the fact that the TGO and the YSZ coating are less strain compliant than the metallic bond coat, inducing a more limited in-plane accommodation of the oxidation

volume eigenstrain at the valley in comparison with the peak. On top of being rather uniform, the data are also quite constant in time, which backs up the validity of the model of a phase transformation eigenstrain exhibiting a constant anisotropy with the main direction along the local normal to the phase boundary (Busso and Qian 2006). However, the variations of the main transformation strain component along the interface, even if limited, greatly influence the local traction. From this analysis, the traction is clearly the main component of the local oxidation kinetics variations. It is essentially compressive in the valley region, inducing the lower oxidation kinetics, slightly tensile near the peak resulting in the faster than average oxidation and vanishes at the mid-slope. It is interesting to notice that the stress contribution gradient is significant over the 0-100 hours range, even if little non-uniformity in the development can be observed at the term of the period. This highlights the progressive development of the oxide scale, but stress effects at long term are also reinforced by the role of diffusion along the interface. Indeed, it becomes more and more influent with time since the oxide thickness increase leads to a decrease of the arriving oxygen flux, thus allowing for a larger mass redistribution along the phase boundary.

4.3.4 Influence on mechanical failure

Thermal barrier coating systems typically fail by large-scale delamination of the thermal coating. This delamination phenomenon results from the coalescence of in-plane cracks developing in the vicinity of the thermally grown oxide (TGO). The nucleation and growth of such cracks are thought to be driven by tensile stresses rising upon cooling due to the undulated morphology of the thermally grown oxide (Evans, Mumm et al.

2001; Padture, Gell et al. 2002). Actually, important tensile stresses within the ceramic alumina TGO and yttria-stabilized zirconia thermal coating (YSZ) layers, as well as substantial shear and tensile tractions at the TGO interfaces might develop as a result of unsymmetrical volume shrinking of the different materials upon cooling. These stresses would play a significant role in the generation and extension of in-plane and interfacial cracks. The maximum values of these critical stresses have therefore been monitored during the isothermal oxidation and upon the material system cooling to room temperature. The results are compared to a situation of uniform oxide growth in order to evaluate the contribution of the non-uniform oxide scale development.

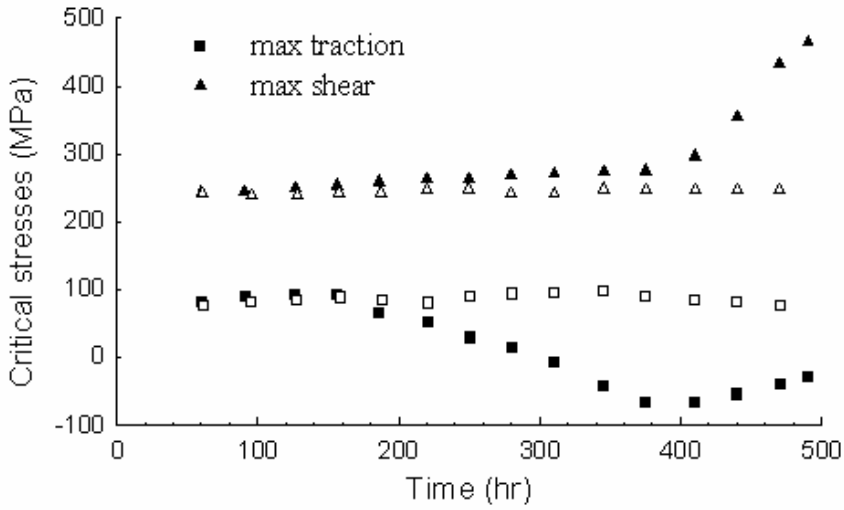

Figure 4.13: Maximum traction and shear stresses at the BC/TGO interface upon cooling to room temperature vs isothermal oxidation time. The black symbols correspond to the case of non-uniform oxide growth and the white ones to a uniform development.

No significant difference in the identified critical stresses can be noticed at oxidation temperature between the uniform and non-uniform oxide growth cases. The stresses

remain anyway limited (below 100 MPa) at high temperature owing to the low elastic limit of the metallic bond coat and the important creep relaxation within the thermally grown oxide layer. The maximum traction and shear stresses along the BC/TGO interface developed upon cooling after given isothermal oxidation times are shown in Figure 4.13. The traction maximum, almost constant in the uniform growth case, is actually decreased at long term as a result of the stress-induced non-uniform oxidation. The interface even becomes fully compressed after around 300 hours. The influence is different regarding the maximum shear developing at the BC/TGO interface. The values corresponding to the uniform and non-uniform growths remain close and rather constant until around 400 hours. A significantly higher shear then develops resulting from the increase in interface curvature induced by the stress-affected isothermal oxidation (see Figure 4.11). Indeed, the maximum shear is located on the side of the morphologically evolving valley ($x_1 \approx 7\mu m$). It nearly doubles between 400 to 500 hours of oxidation, increasing from around 250 to almost 500 MPa. This evolution is likely to precipitate interfacial crack nucleation and growth. Thus the non-uniform oxide growth is likely to accelerate the mechanical failure of the thermal barrier coating system by initiating an early delamination at the BC/TGO interface.

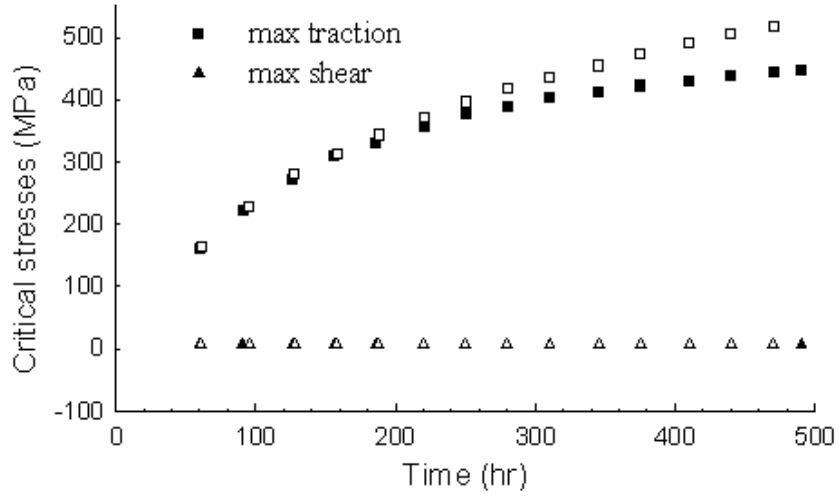

Figure 4.14: Maximum traction and shear stresses at the TGO/YSZ interface upon cooling to room temperature vs isothermal oxidation time. The black symbols correspond to the case of non-uniform oxide growth and the white ones to a uniform development.

The development of geometry-induced tensile stresses within the YSZ coating is thought to play a key role in the growth of in-plane cracks causing TBC delamination, notably under the effect of a ratcheting mechanism associated with thermal cycling. In the simulated situation, the maximum tensile stress actually develops at the YSZ/TGO interface. The evolution with isothermal oxidation time of the highest traction along the material discontinuity upon cooling to room temperature is presented in Figure 4.14. The maximum interfacial shear is also given. However, it can be seen that no significant shear stress develops at the YSZ/TGO interface both in the uniform and non-uniform oxide growth cases. The increase of the traction maximum is significant and rather similar in the two cases. The critical stress reaches above 400 MPa, and cracks are then likely to be induced at or in the vicinity of the interface. Indeed, the tensile strength of the TGO at room temperature has been reported to be lower than this value (it is estimated to 300

MPa in (Vaidyanathan, Jordan et al. 2004)). Although they are close, the uniform oxide growth constitutes here the most detrimental of the two situations, owing to a higher increase rate compared to the non-uniform development from above 200 hours of isothermal oxidation.

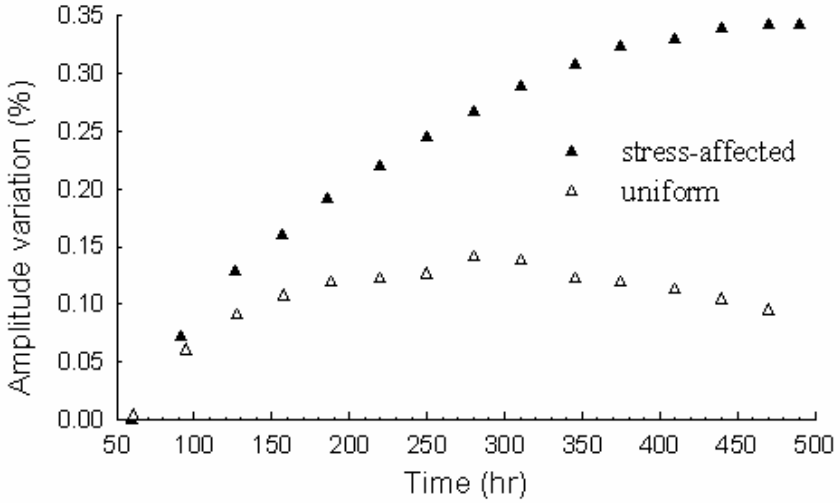

Figure 4.15: Relative variation of the TGO undulation amplitude upon cooling to room temperature vs isothermal oxidation time, given for the cases of non-uniform and uniform oxide growth.

Finally, the TGO deformation upon cooling is analyzed. Indeed, a ratcheting mechanism associated with thermal cycling has been shown to possibly lead to a detrimental increase in out-of-plane tensile stress with time (He, Evans et al. 2000). Although such a mechanism has not been simulated here, it is interesting to investigate the possible contribution of the described stress-induced non-uniform oxide scale growth. The variation of the TGO undulation amplitude upon cooling to room temperature after different isothermal oxidation times is shown in Figure 4.15. The values are given relatively to the variation obtained from the first cooling simulation for the non-uniform

growth case. It can be observed that a much more significant amplitude increase is induced upon cooling of the non-uniformly growing oxide scale. The difference is already significant at 100 hours, and continuously increases with oxidation time. At 450 hours, the relative amplitude variation is about 4 times higher in the stress-affected oxidation case. These data demonstrate the likely detrimental effect of a non-uniform TGO morphology on the deformation of the oxide scale upon cooling. Although this study is not sufficient to conclude, a mechanism of stress-induced non-uniform oxidation might then aggravate the ratcheting phenomenon and thus contribute to decrease the thermal barrier coating mechanical lifetime.

4.3.5 Influence of material-related parameters

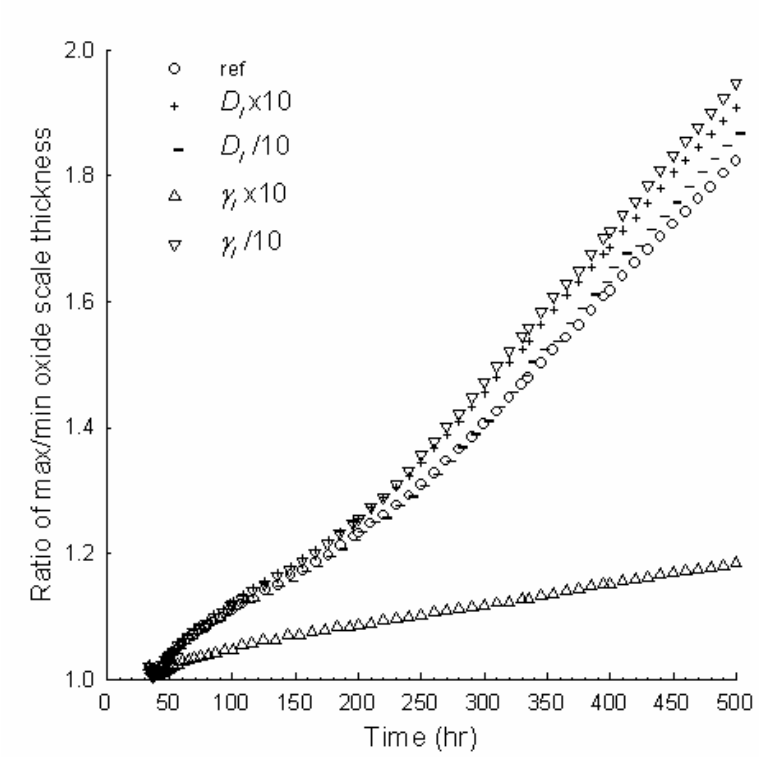

Figure 4.16: Evolution with oxidation time of the ratio of the maximum local scale thickness to the minimum value. The results are presented for different oxide-metal interface energies and diffusivities.

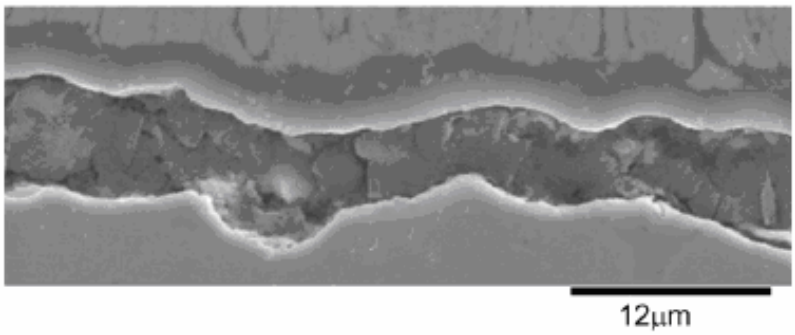

Figure 4.17: Cross section SEM of a thermally grown oxide in a TBC system, showing a typical morphology of the failing stage.

The non-uniform morphology of the oxide scale has been identified as a potentially strongly detrimental factor for the TBC lifetime, in agreement with the litterature (Evans, Clarke et al. 2008). Figure 4.16 shows the evolution with oxidation time of the ratio of the maximum local scale thickness to the minimum value. The respective influences of the oxide-metal interfacial energy and diffusivity are also presented. It can be seen that very significant thickness non-uniformity develops with time in the reference case, with a maximum local thickness getting close to twice the minimum one after 500 hours. The development is quite linear with time, with a rate increase at around 200 hours. As noticed previously, the non-uniformity is limited after 100 hours of oxidation, with a ratio value around 1.1 (10% thickness difference), but more significant after 335 hours where it reaches almost 1.5 (50%). These values are consistent with local thickness ratios than can be observed on SEM micrographs, see for instance Figure 4.17 (Busso, Wright et al. 2007). The fast mass diffusion along the inner interface is a key process contributing to the significant variations in local oxidation kinetics. Therefore the phase boundary diffusivity influences the rate of non-uniform morphological development through the kinetics of mass redistribution. However, it can be seen on Figure 4.16 that the effect of an interface diffusivity variation by an order of magnitude from the reference case considered is limited on the non-uniformity development. This indicates that the diffusion process is not limiting significantly the interface evolution in this case, owing to a high reference value for the interface diffusivity. Furthermore, no clear influence can be deduced here since a decrease of the diffusivity eventually leads to an increase in non-uniformity. This situation is due to the strong local coupling between oxide propagation and traction at the interface, resulting in a direct effect on the traction gradient of a

variation in the oxidation kinetics profile. The influence of the phase boundary energy is very significant, proving its relevant contribution in morphology development damping. The interfacial energy decreases the magnitude of the non-uniform oxide growth, under the effect of the thermodynamic force formed in association with the local curvature which drives a mass repartition along the interface to promote its flattening. The simulation data reported in Figure 4.16 show that an increase by an order of magnitude of the interfacial energy results in a dramatic decrease of the morphology development rate, leading to a thickness ratio below 1.2 after 500 hours of oxidation.

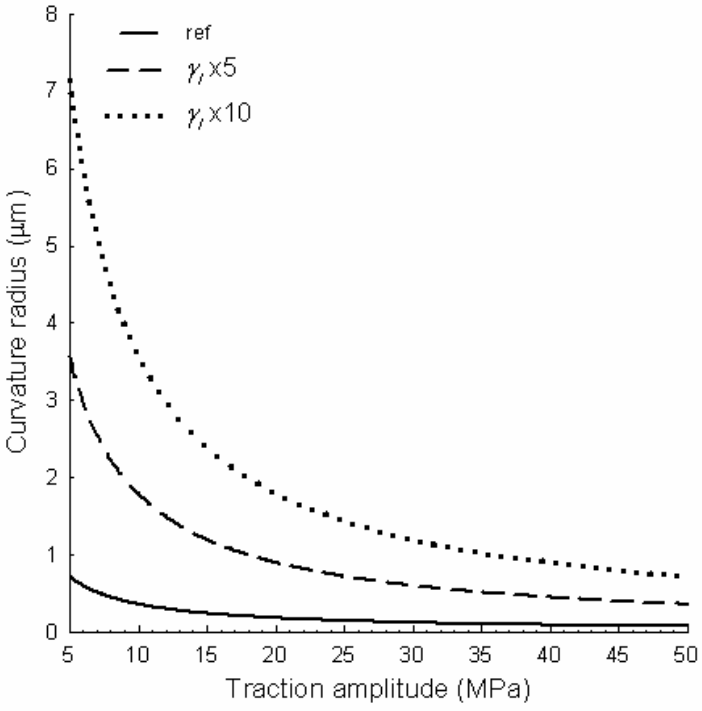

Figure 4.18: Curvature radius vs traction amplitude.

Stresses are generated in response to the large volume eigenstrain induced by the oxide phase propagation over the metallic bond coat. Therefore the stress influence on the

propagation process introduces an indirect local coupling which tends to uniformize the traction gradient along the propagating phase boundary. The traction gradient along the metal/oxide phase boundary is closely related to interface geometry, resulting in local elastic and inelastic accommodations presenting different anisotropies. On the other hand, a similar coupling is induced by local curvature, which at the same time influences and is affected by interface propagation. The two effects are here opposed, and it is therefore relevant to study which curvature would match the stress influence, thus providing a natural range for stress-induced roughness. Figure 4.18 presents the matching curvature radii for a given range of traction amplitudes, $\Delta\sigma_n$, obtained through the approximate relation: $R = 1/\kappa = \gamma_I / \{\Delta\sigma_n(\Pi_I - 1)\}$. The initial maximum curvature radius is around 5μm for the model undulation and the traction amplitude is around 30MPa. It is therefore logical from the graph to obtain a high local curvature development, since the equilibrium radius is more than twenty times lower than the one of the initial interface. The phenomenon is only limited by the process kinetics. The effect of an interfacial energy increase is also presented, showing again the very beneficial contribution. This graph provides two guidelines for the TBC material system design in order to limit non-uniformities development: to increase the interfacial energy, as stated earlier, and to increase the stress relaxation at the phase boundary in order to limit the local traction magnitude. Globally, the maximum traction magnitude at high temperature is essentially set by the bond coat plastic yield stress, which should then be as low as possible in this environment. Lowering the initial interface roughness would also be beneficial since it would result in a decrease of the initial maximum traction (Busso, Wright et al. 2007), thus slowing down the non-uniformity development kinetics.

4.3.6 Conclusion

A study of oxide scale growth developing a non-uniform morphology in an EB-PVD thermal barrier coating system is presented. It is based on a mechanism of stress-affected oxidation kinetics at the metal/oxide sharp phase boundary. The continuum mechanics/diffusion framework includes the volume eigenstrain generation from the main oxidation at the inner interface, the time-dependent and time-independent accommodation behaviors of the different materials, as well as the specific mass diffusion along the propagating phase boundary. The study reveals that a stress-affected local oxidation kinetics assisted by a large mass redistribution through diffusion along the phase boundary might induce the development of an oxide scale of significantly non-uniform morphology. The main influence on the oxidation kinetics local variation comes from the phase transformation work accompanying the propagation of the phase boundary under a traction profile related to the geometry. This work is induced by the accommodation of the large volume eigenstrain associated with the metallic phase oxidation, which develops mainly along the normal direction to the interface. The non-uniform oxide growth induces at long term a significant increase in the maximum shear stress at the inner interface at room temperature. It also leads to an important increase in the undulation amplitude development upon cooling. These two phenomena are likely to dramatically reduce the TBC system lifetime. Finally, the influences of the main parameters on the thickness non-uniformity development are investigated. The interfacial energy is identified as a key property for the attenuation of the development of a rough interface, competing with geometry-induced traction variations. The study provides directions for the design of bond coat metallic alloys in view of increasing the thermal

barrier coating mechanical lifetime. The following properties should be forsaken for the bond coat material:

(1) A high metal/oxide interfacial energy.

(2) A high plasticity at oxidation temperature (low plastic yield stress and high creep rate at low stress) particularly in the vicinity of the alloy interface with the YSZ coating, where the TGO forms. Note that the bond coat is already designed to accommodate the deformations induced by the coating deposition and the oxide layer growth. However, the mechanical behavior at room temperature where the maximum stresses develop is engineered, but not necessarily the behavior at the oxidation temperature.

(3) A low initial roughness at the BC/YSZ interface since the traction variation along the propagating metal/oxide phase boundary results from the geometry. This recommendation is common to all failure investigations since it also allows limiting the maximum tensile stresses developping upon cooling.

(4) Finally, the other recommendations made in the SOFC interconnect investigation also apply for the TBC system although they haven't been directly assessed in this study: a homogeneous composition and a fine microstructure at the microscopic scale of the metallic alloy surface; a low oxygen diffusivity along the metal/oxide boundary; low oxygen and chromium diffusivities within the oxide scale grain boundaries and a fine oxide scale microstructure.

4.4 Mechanism / influences assessment

In order to validate the model and the provided directions for mechanical lifetime improvement, the presented mechanism of stress-affected local oxide growth and its main influences should be experimentally assessed.

A direct experimental observation would not be possible considering the inaccessibility of the key evolving data: stress/strain field at the metal/oxide boundary and interface geometry. Traction across the discontinuity and elastic energies on each side of the interface should be monitored in-situ during isothermal oxidation, along with stress-free strain development associated with metal oxidation and the phase boundary displacement in order to quantitatively evaluate the model. A direct measurement of stress at the interface is probably not possible with today's techniques, which detect an average normal stress level within the resolution zone. Therefore, they only allow recording the dominant principal stress, which is most likely to be an in-plane compression within the thermally grown oxide scale. However, depending on the main growth strain generation mechanism, the maximum in-plane stress will not necessarily be at the metal/oxide interface (Saillard, Cherkaoui et al. 2009). A direct measurement of other stress data and stress-free strains development is even less conceivable. Finally, the interface geometry cannot be observed in-situ since it requires a cross-sectionnal cut or the oxide scale removal. Therefore, a direct experimental assessment is not possible. Besides, the fact that available information is limited to only indirect data constitutes a key motivation for progress in modeling and simulation of material systems evolution during high-temperature oxidation.

Even an indirect assessment of the stress-affected oxidation mechanism modeled in this study would be difficult considering the uncertainty on the main parameters and the difficulty to obtain experimental estimates. In fact, the oxygen diffusivity along the metal/oxide boundary and the interfacial energy have been identified as the most influential material-related parameters. Experimental assessment of the influence of these two parameters would be difficult due to the lack of data for different metallic alloy/oxide scale systems. Furthermore, the likely variations induced by minor alloying elements, additives and impurities not only on these properties but on the whole oxide growth process would render the general validity of any experimental measure uncertain (as it is the case for diffusivity or creep data through the thermally grown oxide scale for instance). However, ranges for specific material systems and trends associated with the presence of a minor species might be identified, notably with the help of computational thermodynamics, atomistic approaches and first-principle calculations (Silva, Agren et al.).

An experimental validation, at least qualitative, of one of the model influences would still be valuable to its assessment. The comparison of developed non-uniformities in oxide scale thickness for different specific experiments might allow observing a targeted influence. Morphological patterns should be identified and statistics in occurrence and dimensions compared between experiments.

The traction magnitude might be affected by experimental means while keeping the same material system. For instance it would be interesting to perform two similar isothermal oxidation experiments on a thermal barrier coating system, one with the YSZ coating and another one with the coating removed. Indeed, the relaxation of the constraint

imposed by the top layer should greatly affect the out-of-plane stress magnitude. Note that for a meaningful comparison the oxide growth kinetics should be similar in magnitude and development direction. Therefore the temperature gradient within the YSZ coating should be accounted for such that the oxide scales grow at similar temperatures in the two experiments.

Another method for stress influence assessment could be to directly apply a lateral (in-plane) stress to the material system (thermal barrier coating system or SOFC interconnect plate) during an isothermal oxidation experiment. However, the imposed stress should be of the order of the in-plane growth stress within the TGO to be significant. At this value, a high plastic deformation of the soft metallic bond coat and/or the damage of the YSZ or another oxide coating are likely, which might prevent from meaningful comparisons between experiments at different stress levels.

Finally, a last track would be to perform isothermal oxidation experiments with metallic alloys presenting the same composition but different microstructures (in term of mean grain size). This should affect the stress relaxation flow rate within the metallic phase and as a consequence the stresses magnitude at the oxide/metal interface. In order to assess the influence of this parameter, the initial metal surface (or interface if a coating is present) rugosity should be similar for the different experiments despite different alloy microstructures, and the stress relaxation variation with grain size should be previously quantified and be significant.

4.5 Guidelines and effects of additives

The two case investigations performed in this study lead to support common recommendations but also provided new tracks to limit non-uniform morphological developments that might be induced by a stress effect on oxidation at the metal/oxide interface. The general guidelines aim at limiting stress development at oxidation temperature and particularly along the metal/oxide boundary on one hand (initial roughness limitation, oxide grain boundary diffusivities reduction, plasticity/creep enhancement); and at uniformizing material properties along the metal/oxide propagating front on the other hand (homogeneous chemical composition and fine microstructure). The new optimization recommendations provided by the developed model of stress-affected oxidation concern the interfacial energy and the oxygen diffusivity of the metal/oxide boundary.

The interfacial energy has been identified as a key property for the attenuation of roughness development at the propagating phase boundary. It forms a driving force in association with the local curvature which tends to uniformize the interface geometry, and is directly competing with stress-induced local variations. Therefore from a thermodynamic approach, increasing the metal/oxide interfacial energy would be highly beneficial in reducing roughness or non-uniform morphology developments. However, attention must be paid to the influence regarding the interface adhesion energy. Indeed, the adhesion energy is an essential property measuring the resistance to delamination of the oxide scale. It thus constitutes a key parameter for the material system mechanical lifetime. The adhesion energy (or work of adhesion), W_{ad}, is related to the interfacial energy, γ_I, through the Dupré equation:

$$W_{ad} = \gamma_{met} + \gamma_{ox} - \gamma_I \tag{4.1}$$

where γ_{met} and γ_{ox} refer to the surface energy of the metal and the oxide phase, respectively. Any modification of the material system considered will affect each of the four parameters, such that no direct correlation can be made between adhesion and interfacial energy, even though the two properties are closely related. Note that the work of adhesion is the free energy change per unit of area when reversibly separating an interface to create two surfaces (the interfacial energy is the free energy associated with the extension of the interface by a unit surface area). The reversibility condition renders the measure inappropriate for delamination description if the two new surfaces are not given enough time to equilibrate, as it would be the case at least at room temperature (Saiz, Cannon et al. 2008). Then a work of separation, which disregards any dissipation, might form a more relevant measure for stress-induced interface fracture energy at room temperature. Estimates of the interfacial energy and the work of adhesion/separation for a given material system can be obtained through atomistic simulations, thus allowing for the combined optimization of the two properties.

Oxygen diffusion along the metal/oxide boundary is a key process in the proposed mechanism of stress-affected oxidation. It might allow large redistribution of the incoming oxygen flux at the interface and as a consequence the development of large non-uniformities in oxide phase propagation over the metallic substrate. Thus, a reduction of the oxygen diffusivity at the interface would be highly beneficial to limit roughness or non-uniform morphology developments. However, fast diffusion at the metal/oxide boundary also allows uniformizing the oxide scale growth through spreading of the oxygen fluxes arriving from grain boundaries. Therefore, a finer oxide scale

microstructure might be necessary to compensate the oxygen interface diffusivity reduction, thus limiting bump formations at grain boundaries (an illustration is provided in Figure 1.29 (Evans, Clarke et al. 2008)). Similarly, a more uniform composition of the oxide layer, particularly in terms of main phases and possible precipitates would help reducing local discrepancies in oxidation kinetics.

The major influence of alloy composition on the oxide scale growth and its lifetime has long been recognized. Aside from the role of main constituent mass fractions, quite well understood (for instance the requirement of a minimum Cr content in Fe-Cr alloys to prevent chromium depletion in the substrate leading to porosity and voids formation (Yang, Weil et al. 2003)), the presence in minor quantities of alloying elements, additives or impurities has long been shown to dramatically affect the oxidation kinetics and the time and mode of failure (Stringer 1989; Hou and Stringer 1995; Hou 2003). Thus, a minor concentration of manganese (Mn), introduced as an alloying element or present as impurity in Fe-Cr alloys, has shown a significant and beneficial impact on chromia scale formation. Manganese ions segregate at grain boundaries within the oxide scale and form a spinel phase which leads to a slower oxidation rate and an improved electronic conductivity. It also limits chromium evaporation, a major issue for metallic SOFC interconnects (Brylewski, Nanko et al. 2001; Yang, Weil et al. 2003; Horita, Xiong et al. 2004; Kurokawa, Kawamura et al. 2004; Fergus 2005).

Table 4.3: Main reactive element effects observed for alumina and chromia thermally grown oxide scales.

Oxide	Extent	Reactive element effect
Alumina	++	Improved scale adhesion
	+	Lower creep rate
	~	Slower growth & less outward
Chromia	++	Slower growth & switch to inward
	+	Improved scale adhesion
	+	Higher creep rate

Since more than a decade, extensive research has been performed in view of gaining understanding and optimizing the effects of reactive elements. According to Whittle and Stringer (Whittle and Stringer 1980), any element which presents a higher affinity for oxygen than the metal constituting the oxide phase, or any fine dispersion of an oxide of this element may produce the "reactive element effect" (REE). The most employed elements are yttrium (Y), lanthanum (La), cerium (Ce) and Hafnium (Hf). The RE effect is actually multiple: globally it is characterized by a lower oxide growth rate and an increased lifetime before mechanical failure. The main identified effects for alumina (Hou 2003) and chromia (Hou and Stringer 1995) are presented in

Table 4.3. The underlying mechanisms to these effects are still subject of debates. However, it is acknowledge that segregation of the reactive elements to the oxide scale grain boundaries and to the oxide/metal interface, as first observed by Pint (Pint 1996), is a key base process.

For alumina oxide scales, an improvement in the layer adhesion to the metallic substrate seems to be the most beneficial reactive element effect. This effect is thought to result from sulfur and carbon scavenging at the metal/oxide boundary, thus strengthening

interface bonds (Stringer 1989; Sarioglu, Stiger et al. 2000; Bennett, Kranenburg et al. 2005; Hou 2008). Note that platinum has been shown to provide the same effect. Although the reported effects seem less significant or general, a lower creep rate and a slower oxide growth, particularly in the outward direction, have also been observed to result from the addition of reactive elements. A site blocking mechanism altering diffusion is most commonly advanced to explain these contributions (Cho, Wang et al. ; Harding, Atkinson et al. ; Chen, Xu et al. 2005; Nychka and Clarke 2005; Nakagawa, Sakaguchi et al. 2007; Heuer 2008; Milas, Hinnemann et al. 2008). A higher local bonding energy has also been proposed (Cho, Wang et al. ; Matsunaga, Tanaka et al. 2003; Chen, Xu et al. 2005; Nychka and Clarke 2005; Buban, Matsunaga et al. 2006; Milas, Hinnemann et al. 2008), which might be due to the removal of impurities as sulfur (Nakagawa, Sakaguchi et al. 2007). Finally, an effect on grain growth reducing the grain boundary volume fraction within the oxide scale has been suggested (Liu, Gao et al. 2000; Naumenko, Gleeson et al. 2007).

The dominant observed reactive element effect for chromia scales is a significant reduction in the oxide growth rate and a switch of the main direction of development from outward to inward. Reactive elements are here thought to contribute through the annihilation of the metal diffusion sites (Pieraggi and Rapp 1993; Liu, Stack et al. 1998; Ramanarayanan, Mumford et al. 2000), or an alteration of the metal transport through the interface (Hou and Stringer 1995). As for alumina scales, the addition of reactive elements has been shown as being very beneficial to the adhesion of chromia scales, most likely by preventing vacancy condensation at the metal/oxide interface (Stringer 1989; Li and Hou 2007). Finally, reactive elements have also been observed to reduce stress

development at oxidation temperature. This effect is thought to result from the reactive elements increasing the density of oxide nucleation sites, thus resulting in a finer microstructure of the growing oxide scale (Huntz, Daghigh et al. 1998; Chevalier, Valot et al. 2003).

Each of the reactive element effects might influence the proposed mechanisms of non-uniform oxide scale growth resulting from a stress effect on high temperature oxidation. However, considering the different influences and their strong couplings, it seems not possible to draw general conclusions. For instance, a lower creep relaxation coupled with a more inward oxide growth would increase morphological developments induced by stress-affected inner oxidation. Thus the addition of reactive elements could be to some aspects detrimental to metal/alumina systems' mechanical lifetime. However, the influences on the key properties that are the interfacial energy and the oxygen diffusivity of the metal/oxide boundary are missing, preventing any tentative conclusion. The situation is similar for the growth of chromia scales, although this time the refinement of the oxide layer microstructure and the reduction of stress development constitute two very beneficial contributions based on our investigation. The interfacial energy and the oxygen diffusivity of the metal/oxide boundary might be tailored through the use of additives, notably reactive elements, since they are known to segregate at the interface (Pint 1996). However to our knowledge, no trend even qualitative is available concerning an effect of additives on the interfacial energy and the interface oxygen diffusivity. Considering the difficulty to experimentally measure these properties, atomistic simulations should be set up to investigate the influence of the base metallic

alloy and of additives on these parameters. Such investigations on the variations of key properties depending on alloy composition should be coupled with representative macroscopic analyses using the developped simulation tool. This method should allow providing strong recommendations for metallic alloy design significantly improving the mechanical lifetime of the considered interconnect and thermal barrier coating systems.

4.6 References

Bennett, I. J., J. M. Kranenburg and W. G. Sloof (2005). "Modeling the influence of reactive elements on the work of adhesion between oxides and metal alloys." Journal of the American Ceramic Society **88**(8): 2209-2216.

Birks, N., G. H. Meier and F. S. Pettit (2006). Introduction to the high-temperature oxidation of metals. New York, Cambridge University Press.

Bonzel, H. P. and N. A. Gjostein (1968). "Diffraction theory of sinusoidal gratings and application to in-situ surface self-diffusion measurements." Journal of Applied Physics **39**(7): 3480-3491.

Brylewski, T., M. Nanko, T. Maruyama and K. Przybylski (2001). "Application of fe-16cr ferritic alloy to interconnector for a solid oxide fuel cell." Solid State Ionics **143**(2): 131-150.

Buban, J. P., K. Matsunaga, J. Chen, N. Shibata, W. Y. Ching, T. Yamamoto and Y. Ikuhara (2006). "Grain boundary strengthening in alumina by rare earth impurities." Science **311**(5758): 212-215.

Busso, E. P., J. Lin, S. Sakurai and M. Nakayama (2001). "A mechanistic study of oxidation-induced degradation in a plasma-sprayed thermal barrier coating. Part i: Model formulation." Acta Materialia **49**: 1515-1528.

Busso, E. P. and Z. Q. Qian (2006). "A mechanistic study of microcracking in transversely isotropic ceramic-metal systems." Acta Materialia **54**: 3325-338.

Busso, E. P., L. Wright, H. E. Evans, L. N. McCartney, S. R. J. Saunders, S. Osgerby and J. Nunn (2007). "A physics-based life prediction methodology for thermal barrier coating systems." Acta Materialia **55**(5): 1491-1503.

Chen, J., Y. N. Xu, P. Rulis, L. Z. Ouyang and W. Y. Ching (2005). "Ab initio theoretical tensile test on y-doped sigma=3 grain boundary in alpha-al2o3." Acta Materialia **53**(2): 403-410.

Cheng, J., E. H. Jordan, B. Barber and M. Gell (1998). "Thermal/residual stress in an electron beam physical vapor deposited thermal barrier coating system." Acta Materialia **46**(16): 5839-5850.

Chevalier, S., C. Valot, G. Bonnet, J. C. Colson and J. P. Larpin (2003). "The reactive element effect on thermally grown chromia scale residual stress." Materials Science and Engineering a-Structural Materials Properties Microstructure and Processing **343**(1-2): 257-264.

Cho, J., C. M. Wang, H. M. Chan, J. M. Rickman and M. P. Harmer Role of segregating dopants on the improved creep resistance of aluminum oxide.

Clarke, D. R. (2003). "The lateral growth strain accompanying the formation of a thermally grown oxide." Acta Materialia **51**: 1393-1407.

Essuman, E., G. Meier, J. Zurek, M. Hänsel, L. Singheiser and W. Quadakkers (2007). "Enhanced internal oxidation as trigger for breakaway oxidation of fe–cr alloys in gases containing water vapor." Scripta Materialia **57**: 845-848.

Evans, A. G., D. R. Clarke and C. G. Levi (2008). "The influence of oxides on the performance of advanced gas turbines." Journal of the European Ceramic Society **28**(7): 1405-1419.

Evans, A. G., D. R. Mumm, J. W. Hutchinson, G. H. Meier and F. S. Pettit (2001). "Mechanisms controlling the durability of thermal barrier coatings." Progress in Materials Science **46**(5): 505-553.

Evans, H. E. (1995). "Stress effects in high-temperature oxidation of metals." International Materials Reviews **40**(1): 1-40.

Evans, U. R. (1948). An introduction to metallic corrosion. London, Edward Arnold.

Fergus, J. W. (2005). "Metallic interconnects for solid oxide fuel cells." Materials Science and Engineering **A397**: 271-283.

Harding, J. H., K. J. W. Atkinson and R. W. Grimes Experiment and theory of diffusion in alumina.

He, M. Y., A. G. Evans and J. W. Hutchinson (2000). "The ratcheting of compressed thermally grown thin films on ductile substrates." Acta Materialia **48**(10): 2593-2601.

Heuer, A. H. (2008). "Oxygen and aluminum diffusion in alpha-al2o3: How much do we really understand?" Journal of the European Ceramic Society **28**(7): 1495-1507.

Hirota, K., H. Motono, M. Yoshinaka and O. Yamaguchi (2002). "Fabrication and mechanical properties of almost fully-densified cr2o3 ceramics." Journal of Materials Science Letters **21**(11): 853-854.

Horita, T., Y. Xiong, K. Yamaji, H. Kishimoto, N. Sakai, M. E. Brito and H. Yokokawa (2004). "Imaging of mass transports around the oxide scale/fe-cr alloy interfaces." Solid State Ionics **174**: 41-48.

Hou, P. Y. (2003). "Impurity effects on alumina scale growth." Journal of the American Ceramic Society **86**(4): 660-668.

Hou, P. Y. (2008). "Segregation phenomena at thermally grown al2o3/alloy interfaces." Annual Review of Materials Research **38**: 275-298.

Hou, P. Y., A. P. Paulikas, B. W. Veal and J. L. Smialek (2007). "Thermally grown al2o3 on a h-2-annealed fe3al alloy: Stress evolution and film adhesion." Acta Materialia **55**(16): 5601-5613.

Hou, P. Y. and J. Stringer (1995). "The effect of reactive element additions on the selective oxidation, growth and adhesion of chromia scales." Materials Science and Engineering a-Structural Materials Properties Microstructure and Processing **A202**(1-2): 1-10.

Huntz, A. M., J. Balmain, S. C. Tsai, K. Messaoudi, M. K. Loudjani, B. Lesage and J. Li (1997). "Diffusion studies in oxides scales grown on alumina- and chromia-forming alloys." Scripta Materialia **37**(5): 651-660.

Huntz, A. M., S. Daghigh, A. Piant and J. L. Lebrun (1998). "Evidence of stress relaxation in thermally grown oxide layers - experiments and modelling." Materials Science and Engineering **A248**: 44-55.

Krishnamurthy, R., Y.-G. Yoon, D. J. Srolovitz and R. Car (2004). "Oxygen diffusion in yttria-stabilized zirconia: A new simulation model." Journal of the American Ceramic Society **87**(10): 1821-1830.

Kurokawa, H., K. Kawamura and T. Maruyama (2004). "Oxidation behavior of fe-16cr alloy interconnect for sofc under hydrogen potential gradient." Solid State Ionics **168**: 13-21.

Li, M. S. and P. Y. Hou (2007). "Improved cr2o3 adhesion by ce ion implantation in the presence of interfacial sulfur segregation." Acta Materialia **55**(2): 443-453.

Li, T., R. J. Brook and B. Derby (1999). "Fabrication of reaction-bonded cr_2o_3 ceramics." Journal of the European Ceramic Society **19**(8): 1651-1664.

Liu, H., M. M. Stack and S. B. Lyon (1998). "Reactive element effects on the ionic transport processes in cr_2o_3 scales." Solid State Ionics **109**: 247-257.

Liu, W. N., X. Sun, E. Stephens and M. A. Khaleel (2009). "Life prediction of coated and uncoated metallic interconnect for solid oxide fuel cell applications." Journal of Power Sources **189**(2): 1044-1050.

Liu, Z., W. Gao and Y. He (2000). "Modeling of oxidation kinetics of y-doped fe-cr-al alloys." Oxidation of Metals **53**(3-4): 341-350.

Matsunaga, K., T. Tanaka, T. Yamamoto and Y. Ikuhara (2003). "First-principles calculations of intrinsic defects in al2o3." Physical Review B **68**(8).

Mikkelsen, L. and S. Linderoth (2003). "High temperature oxidation of fe-cr alloy in o_2-h_2-h_2o atmospheres; microstructure and kinetics." Materials Science and Engineering **A361**: 198-212.

Milas, I., B. Hinnemann and E. A. Carter (2008). "Structure of and ion segregation to an alumina grain boundary: Implications for growth and creep." Journal of Materials Research **23**(5): 1494-1508.

Mougin, J., A. Galerie, M. Dupeux, N. Rosman, G. Lucazeau, A. M. Huntz and L. Antoni (2002). "In-situ determination of growth and thermal stresses in chromia scales formed on a ferritic stainless steel." Materials and Corrosion **53**: 486-490.

Mougin, J., G. Lucazeau, A. Galerie and M. Dupeux (2001). "Influence of cooling rate and initial surface roughness on the residual stresses in chromia scales thermally grown on pure chromium." Materials Science and Engineering a-Structural Materials Properties Microstructure and Processing **308**(1-2): 118-123.

Murr, L. E. (1973). "Measurement of interfacial energy and energy of adhesion by scanning electron-microscopy." Materials Science and Engineering **12**(5-6): 277-283.

Nakagawa, T., I. Sakaguchi, N. Shibata, K. Matsunaga, T. Mizoguchi, T. Yamamoto, H. Haneda and Y. Ikuhara (2007). "Yttrium doping effect on oxygen grain boundary diffusion in alpha-al2o3." Acta Materialia **55**(19): 6627-6633.

Naumenko, D., B. Gleeson, E. Wessel, L. Singheiser and W. J. Quadakkers (2007). "Correlation between the microstructure, growth mechanism, and growth kinetics of alumina scales on a fecraly alloy." Metallurgical and Materials Transactions a-Physical Metallurgy and Materials Science **38A**: 2974-2983.

Nychka, J. A. and D. R. Clarke (2005). "Quantification of aluminum outward diffusion during oxidation of fecral alloys." Oxidation of Metals **63**(5-6): 325-352.

Padture, N. P., M. Gell and E. H. Jordan (2002). "Materials science - thermal barrier coatings for gas-turbine engine applications." Science **296**(5566): 280-284.

Pan, D., M. W. Chen, P. K. Wright and K. J. Hemker (2003). "Evolution of a diffusion aluminide bond coat for thermal barrier coatings during thermal cycling." Acta Materiala **51**: 2205-2217.

Panat, R. and K. J. Hsia (2004). "Experimental investigation of the bond-coat rumpling instability under isothermal and cyclic thermal histories in thermal barrier systems." Proceedings of the Royal Society of London Series A-Mathematical Physical and Engineering Sciences **460**(2047): 1957-1979.

Panat, R., K. J. Hsia and D. G. Cahill (2005). "Evolution of surface waviness in thin films via volume and surface diffusion." Journal of Applied Physics **97**(1).

Panat, R., K. J. Hsia and J. Oldham (2005). "Rumpling instability in thermal barrier systems under isothermal conditions in vacuum." Philosophical Magazine **85**(1): 45-64.

Peraldi, R. and B. A. Pint (2004). "Effect of cr and ni contents on the oxidation behavior of ferritic and austenitic model alloys in air with water vapor." Oxidation of Metals **61**(5-6): 463-483.

Pieraggi, B. and R. A. Rapp (1993). "Chromia scale growth in alloy oxidation and the reactive element effect." Journal of the Electrochemical Society **140**(10): 2844-2850.

Pilling, N. B. and R. E. Bedworth (1923). "The oxidation of metals at high temperatures." Journal of the Institute of Metals **29**: 529-582.

Pint, B. A. (1996). "Experimental observations in support of the dynamic-segregation theory to explain the reactive-element effect." Oxidation of Metals **45**(1-2): 1-37.

Ramanarayanan, T. A., J. D. Mumford, C. M. Chun and R. A. Petkovic (2000). "Transport through chromia films." Solid State Ionics **136-137**: 83-90.

Rhines, F. N. and J. S. Wolf (1970). "The role of oxide microstructure and growth stresses in the high-temperature scaling of nickel." Metal. Trans. **1**: 1701-1710.

Saillard, A., M. Cherkaoui, L. Capolungo and E. P. Busso (2009). High-temperature oxidation of metallic alloys for sofc interconnects: Stress and morphological developments during oxide scale growth. Material Research Society Spring Meeting, San Francisco.

Saiz, E., R. M. Cannon and A. P. Tomsia (2008). "High-temperature wetting and the work of adhesion in metal/oxide systems." Annual Review of Materials Research **38**: 197-226.

Sarioglu, C., M. J. Stiger, J. R. Blachere, R. Janakiraman, E. Schumann, A. Ashary, F. S. Pettit and G. H. Meier (2000). "The adhesion of alumina films to metallic alloys and coatings." Materials and Corrosion-Werkstoffe Und Korrosion **51**(5): 358-372.

Silva, A. C. E., J. Agren, M. T. Clavaguera-Mora, D. Djurovic, T. Gomez-Acebo, B. J. Lee, Z. K. Liu, P. Miodownik and H. J. Seifert Applications of computational thermodynamics - the extension from phase equilibrium to phase transformations and other properties, Pergamon-Elsevier Science Ltd.

Spitsberg, I. T., D. R. Mumm and A. G. Evans (2005). "On the failure mechanisms of thermal barrier coatings with diffusion aluminide bond coatings." Materials Science and Engineering A-Structural Materials Properties Microstructure and Processing **394**(1-2): 176-191.

Stringer, J. (1989). "The reactive element effect in high-temperature corrosion." Materials Science and Engineering a-Structural Materials Properties Microstructure and Processing **120**: 129-137.

Sun, X., W. N. Liu, E. Stephens and M. A. Khaleel (2008). "Determination of interfacial adhesion strength between oxide scale and substrate for metallic sofc interconnects." Journal of Power Sources **176**(1): 167-174.

Takano, Y., T. Komeda, M. Yoshinaka, K. Hirota and O. Yamaguchi (1998). "Fabrication, microstructure, and mechanical properties of cr2o3/zro2(2.5y) composite ceramics in the cr2o3-rich region." Journal of the American Ceramic Society **81**(9): 2497-2500.

ThyssenKrupp-VDM (2005). Material data sheet no. 4046: Crofer 22 apu. Werdohl, Germany.

Tolpygo, V. K. and D. R. Clarke (2007). "Temperature and cycle-time dependence of rumpling in platinum-modified diffusion aluminide coatings." Scripta Materialia **57**(7): 563-566.

Tolpygo, V. K., J. R. Dryden and D. R. Clarke (1998). "Determination of the growth stress and strain in alpha-al_2o_3 scales during the oxidation of fe–22cr–4.8al–0.3y alloy." Acta Materialia **46**(3): 927-937.

Vaidyanathan, K., E. H. Jordan and M. Gell (2004). "Surface geometry and strain energy effects in the failure of a (ni, pt)al/eb-pvd thermal barrier coating." Acta Materialia **52**(5): 1107-1115.

Whittle, D. P. and J. Stringer (1980). "Improvements in high-temperature oxidation resistance by additions of reactive elements or oxide dispersions." Philosophical Transactions of the Royal Society of London Series a-Mathematical Physical and Engineering Sciences **295**(1413): 309-&.

Yang, Z., K. S. Weil, D. M. Paxton and J. W. Stevenson (2003). "Selection and evaluation of heat-resistant alloys for sofc interconnect applications." Journal of the Electrochemical Society **150**(9): A1188-A1201.

Yang, Z. G. (2008). "Recent advances in metallic interconnects for solid oxide fuel cells." International Materials Reviews **53**(1): 39-54.

CONCLUSION

In the presented research work, oxide scale growth and associated stress and morphological developments during high temperature oxidation are investigated. The objective is to improve the understanding of the mechanisms leading to the development of oxide scales of non-uniform morphology, a situation which has been identified to accelerate mechanical failure and thus to limit metallic systems' lifetime in oxidizing environment at high temperature. Two different oxides, alumina and chromia, in two different industrial systems, thermal barrier coatings and solid oxide fuel cell metallic interconnects are studied. The phenomenon of oxide scale growth and its modeling are reviewed, with an emphasis on stress development and mechanical failure mechanisms. This review work pointed out the much detrimental contribution of non-uniform morphological developments of the oxide scale on the material systems' resistance to mechanical failure, as well as the importance of growth stresses at oxidation temperature. It lead us to focus on the investigation of a possible mechanism of stress-induced irregular morphological development in growing oxide scales at high temperature.

A specific formulation of stress-affected local oxide phase propagation by direct oxidation of the metallic substrate at the metal/oxide interface is developed. The mechanism proposed for a stress influence on the local oxidation kinetics relies on a deviation from the stress-free quasi-equilibrium concentration induced by the stress and strain jumps at the sharp propagating interface. Since the gradient of concentration drives species diffusion, the local incoming flux of oxygen at the phase boundary is in turn affected and eventually the oxidation kinetics is locally modified. A continuum mechanics description of a dissipative sharp interface propagation is then

derived to include the influence of the elastic energy jump and the phase transformation accommodation work on the phase boundary propagation kinetics. For a complete description of the local oxidation process, the derivation includes the mass diffusion fluxes, the mass consumption as well as the deformation work during the phase transformation process. Furthermore, it incorporates the contribution of the possible large volumetric strain associated with the direct metal oxidation.

The local formulation of stress-affected oxidation is completed with a phenomenological macroscopic framework, and a numerical tool is developed allowing for the analysis of complex cases. The framework includes species diffusion in a polycrystalline material, accounting for fast diffusion paths and in particular the contribution of the phase boundary itself as an enhanced transport route. Two sources of strain generation during isothermal oxide growth are considered. They are likely to induce high stresses at oxidation temperature, possibly affecting the oxide scale development and contributing to its precipitated mechanical failure. The two mechanisms accounted for are a local volume eigenstrain associated with the metal phase direct oxidation at the metal/oxide boundary, from the original theory of Pilling and Bedworth; and an in-plane inelastic strain resulting from secondary oxide formation within oxide scale grain boundaries, following the concept initially introduced by Rhines and Wolf. Elasto-visco-plastic mechanical behaviors are considered for the stress-free strains accommodation within the metal and oxide materials. In order to implement the presented framework of stress-affected metal oxidation, a specific numerical tool has been developed allowing for the propagation of an evolving sharp interface following a complex law dependent on field values. It is based on a finite element method for the fields' resolution, performed sequentially with a specially developed external

routine run in pre/post-calculations at each time step to calculate the phase boundary composition and propagation.

Finally, two practical situations in which oxide scale growth and associated stress and morphological developments are critical to the material system's lifetime have been identified and are investigated. The first one considers the inner growth of a chromia layer from a flat surface of an uncoated chromia forming ferritic steels for SOFC interconnect at moderate temperature (~800°C). The second treats the development at higher temperature (~1100°C) of an alumina scale at a convoluted interface separating a nickel-aluminum bond coat and an yttria-stabilized zirconia layer forming a thermal barrier coating. For each case, a mechanism of stress-induced irregular morphological development is studied. The main processes and influences are analyzed allowing for the identification of key physical properties. In order to investigate the consequences of the non-uniform growth regarding mechanical failure mechanisms, the evolution of critical stresses during isothermal oxidation and upon cooling to room temperature are analyzed. This study points out the major detrimental role of a non-uniform oxide scale development on the material system's mechanical lifetime. Eventually, the influences of material-related parameters are tested. The study provides recommendations on physical properties for the limitation of detrimental morphological developments. These optimization tracks are discussed along with the possible influence of reactive elements.

This work provides a broad and comprehensive review on high-temperature oxidation, with a focus on the processes associated with stress and morphological developments, along with their influence on mechanical failure mechanisms. While extensive research has been performed over the last decades, considerable challenges remain in understanding and modeling of the

mechanisms affecting the oxide/metal systems' mechanical lifetime. The developed framework for phase boundary propagation coupled with mechanical stress development contributes to the modeling and investigation of macroscopic phase growth phenomena coupled with stress generation. The model applies to many industrial systems undergoing high temperature oxidation, such as thermal barrier coatings and SOFC interconnects. It should also allows for investigations concerning semi-conductor devices and more generally any material system undergoing diffusion-driven sharp phase boundary propagation. It accounts for mass conservation and large volume eigenstrain development in association with phase transformation, not present in most sharp phase boundary propagation models. The building of the simulation tool highlighted the complexity of multi-physics coupled analysis of a sharp propagating discontinuity separating two evolving domains. Owing to the complex and specific requirements imposed by the developed model for realistic complete investigations, an adapted scheme has been built which allows for the simulation of complex field-dependent propagation of a sharp phase boundary including the important contribution of mass diffusion along the interface. Finally, we believe that our simulations and analyses of the selected high temperature oxidation cases will contribute to a better understanding of the mechanisms influencing mechanical failure and of their relations with the metallic alloy properties and composition. This in turn will help optimizing material composition and preparation allowing for the increase of oxide/metal systems lifetimes.

Future work should primarily focus on the experimental assessment of the described mechanism of stress-induced non-uniform oxide scale growth at high temperature. This would include bringing experimental evidence of the stress influence on roughness or non-uniform thickness development during isothermal oxidation, but also obtaining finer and material

composition-dependent estimates of the key physical properties, particularly oxygen diffusivity and interfacial energy of the metal/oxide boundary. Eventually the recommendations provided by our analyses should be tested.

Additional simulations should be performed in order to investigate the influence of coupling thermal cycling with the stress-affected oxidation mechanism. Moreover, only two generic initial interface geometries have been studied during this work. More complex interface profiles representative of practical systems should be studied in order to better assess the global influence of the stress-affected oxidation mechanism.

Finally, the model could be extended by the introduction of more complex material models accounting for: the composition and microstructure of the metal and the oxide layers, as well as their evolution during isothermal oxidation; the description of multi-species diffusion and the nucleation and growth of secondary phases; and finally material and interface damage development through crack and voids growth, allowing for refined failure studies.